

Title	湿潤接着性向上のための形態適応性ソフトコンタクトの機構
Author(s)	NGUYEN, DANG DU Y
Citation	
Issue Date	2024-06
Type	Thesis or Dissertation
Text version	ETD
URL	<a href="http://hdl.handle.net/10119/19333">http://hdl.handle.net/10119/19333</a>
Rights	
Description	Supervisor: Ho Anh Van, 先端科学技術研究科, 博士

DOCTORAL DISSERTATION

Mechanics of morphologically adaptive soft contact for  
wet adhesion enhancement

NGUYEN Dang Duy

Supervisor: HO Anh Van

Graduate School of Advanced Science and Tehcnology

Japan Advanced Institute of Science and Technology

Materials Science

June, 2024



JAPAN ADVANCED INSTITUTE OF SCIENCE AND TECHNOLOGY

# *Abstract*

Graduate School of Advanced Science and Technology

Doctoral Dissertation

## **Mechanics of morphologically adaptive soft contact for wet adhesion enhancement**

by NGUYEN Dang Duy

This thesis delves into the concept of animal adaptation to various environments through the ability to morphologically adapt, often referred to as morphological design. It focuses on the significant role of tribological phenomena in different animal species, such as human fingers in grasping, gecko toes in dry locomotion, and tree frog toes in wet gripping, and how these findings can be applied to engineering. Wet adhesion, a crucial aspect in tribology, is explored, and its potential application in robotics is investigated, particularly in the context of stable robot walking that requires effective gait planning and control. The mechanical properties of the interaction between robot feet and the ground surface are considered pivotal.

In this research, we propose a mechanics of morphology changeable soft pad for robotic feet capable of adapting its morphology to the changing terrains that robots encounter. This adaptation includes optimizing various tribological factors such as friction, adhesion, and particularly wet adhesion when the foot interacts with wet surfaces. The function of actively changing morphology to adapt to the environment plays an important role in embodied robots. The result proposed in this thesis is promising to use for the application of embodied robots that perceive their surroundings to manipulate objects or move their bodies, process information, and make decisions.



First, I establish a mathematical model based on energy equations to provide insights into the principles of morphological changes of the robot foot. I then present two approaches to model the value of wet adhesion in preventing slippage for the robot's foot. The first approach simplifies the foot shape to streamline complex parameters for calculating wet adhesion forces. The second approach introduces a more generalized model based on finite element methods to describe wet adhesion forces on a soft body interacting with various ground surfaces. This generalized model is validated and simulated using the Simulation Open Framework Architecture (SOFA framework).

Subsequently, we present experimental data that corroborates the accuracy of the mathematical models proposed in this research. Finally, we test the application of the morphologically adaptable robot foot in two scenarios using a separate legged robot and a complete hexapod robot in showcases. These applications aim to showcase the effectiveness and potential practicality of a morphologically adaptable robot foot.

In conclusion, this research advances our understanding of animal-inspired robotics, particularly focusing on the significance of morphological adaptability and wet adhesion in robotic locomotion. The proposed model and its practical application hold promise for the development of robots capable of efficiently traversing various terrains and adapting to different environments.

*Keywords: Tribology, capillary, morphology computation, soft toe pad, animal locomotion, SOFA, finite element, embodied robot*

# *Acknowledgements*

Completing this doctoral thesis has been a journey of growth, learning, and perseverance. It is with immense gratitude that I extend my thanks to the following individuals and groups who have supported me on this academic expedition.

First and foremost, I would like to express my deepest appreciation to my main supervisor, Assoc. Prof. Ho Anh Van, for his unwavering guidance, invaluable insights, and unwavering dedication to my research. Your mentorship has been a beacon of wisdom that illuminated my path throughout this journey.

I am equally grateful to my second supervisor, Assoc. Prof. Ji Yonghoon, whose expertise and constructive feedback have enriched the quality of this work and broadened my horizons in the field.

I extend my heartfelt appreciation to Prof. Nguyen Le Minh, who served as my Advisor for Minor Research Project, for providing critical direction and unceasing support in this endeavor.

My profound thanks also go out to the entire team at the Soft Haptics Lab, School of Materials Science, Japan Advanced Institute of Science and Technology, for creating a vibrant, collaborative research environment and contributing to my academic and personal growth.

To my family, especially my wife and son, your unwavering support, encouragement, and patience throughout this journey have been my greatest source of strength and motivation. I owe this achievement to your understanding and love.

Lastly, my thanks to all my friends and colleagues who have provided inspiration and shared their knowledge.

In this collective effort, I have had the privilege of standing on the shoulders of giants, and I am deeply appreciative of each one's role in making this thesis possible.



# Achievements

## International Journal

- **Duy Dang Nguyen**, Nhan Huu Nguyen, Van Anh Ho, "Morphology-Changeable Soft Pads Facilitate Locomotion in Wet Conditions," in IEEE Robotics and Automation Letters, vol. 8, no. 5, pp. 2983-2990, May 2023, doi: 10.1109/LRA.2023.3264731. (The research was presented orally at The 2023 IEEE/RSJ International Conference on Intelligent Robots and Systems - IROS 2023, Detroit, Michigan, USA.)
- **Duy Dang Nguyen**, Nam Phuong Dam, and Van Anh Ho "Enhancing wet surface adhesion in walking robots: finite element-based analysis and morphology-changeable soft pads." *Advanced Robotics* (2024): 1-17, doi: 10.1080/01691864.2024.2327649
- Harit Pitakjakpipop, Robin Rajan, Kittipong Tantisantisom, Pakorn Opaprakasit, **Duy Dang Nguyen**, Van Anh Ho, Kazuaki Matsumura, and Paisan Khanchaitit, "Facile Photolithographic Fabrication of Zwitterionic Polymer Microneedles with Protein Aggregation Inhibition for Transdermal Drug Delivery", *Biomacromolecules* 2022 23 (1), 365-376, DOI: 10.1021/acs.biomac.1c01325.

IEEE Robotics and Automation Letters metrics: Impact Factor: 5.2, CiteScore: 8.0; Ranking: Q1 in Artificial Intelligence, Q1 in Biomedical Engineering, Q1 in Computer Science Applications, Q1 in Computer Vision and Pattern Recognition, Q1 in Control and Optimization, Q1 in Control and Systems Engineering, Q1 in Human-Computer Interaction, Q1 in Mechanical Engineering; #2 journal in top publications of Robotics by Google scholar.

International Conference on Intelligent Robots and Systems (IROS) is flagship international conference of Robotics: Impact score: 2.45; #4 journal in top publications of Robotics by Google scholar.



# Contents

<b>Abstract</b>	<b>iii</b>
<b>Acknowledgements</b>	<b>v</b>
<b>Achievements</b>	<b>vii</b>
<b>1 Introduction</b>	<b>1</b>
<b>2 Background and Related Works</b>	<b>7</b>
2.1 Morphology and bio-inspired structure of animals' food pad with adhesion and capillary . . . . .	7
2.2 Contact mechanics models for elastic material . . . . .	9
2.3 Finite Element method for wet adhesion and capillary . . . . .	11
2.4 The contribution of this thesis . . . . .	13
<b>3 Bioinspired robotic foot facilitating wet adhesion</b>	<b>15</b>
3.1 ANALYTICAL MODEL . . . . .	15
3.1.1 Morphology computation model . . . . .	15
3.1.2 Contact model with liquid film . . . . .	25
3.1.3 Optimal function for design parameters . . . . .	28
3.2 Experimental . . . . .	32
3.2.1 Inflation and contact-related shape verification . . . . .	33
3.2.2 Tangential force experiment . . . . .	38
<b>4 The finite element analysis (FEA) for representing wet</b>	<b>43</b>
4.1 The FEA-based solution . . . . .	43
4.1.1 The general problem of capillary phenomenon . . . . .	44

4.1.2	The FEA-based model for the capillary phenomenon . . . . .	44
4.2	Implementation using SOFA (Simulation Open Framework Architecture) framework . . . . .	48
4.2.1	The wet adhesion phenomenon simulation for various shape objects using SOFA . . . . .	48
4.2.2	The FEA-based model for the capillary phenomenon of the patterned pad . . . . .	56
4.3	Experimental validation . . . . .	58
4.3.1	Tangential force experiment . . . . .	58
<b>5</b>	<b>Application to slippage resistance of locomotive robot on wet surface</b>	<b>63</b>
5.1	Design and fabrication . . . . .	63
5.1.1	Large scale design . . . . .	64
5.1.2	Small scale design . . . . .	65
5.2	Case of single legged robot with the proposed foot . . . . .	66
5.3	Case of hexapod robot with the proposed feet . . . . .	70
<b>6</b>	<b>Conclusion and Future Works</b>	<b>75</b>
6.1	Impact of morphology-changeable soft pads . . . . .	75
6.1.1	Design and fabrication . . . . .	75
6.1.2	Analytical model and finite element method model for Morphology changeable soft dome pad . . . . .	76
6.1.3	Application for legged robot walking on different terrain without slippage . . . . .	77
6.2	Future work . . . . .	78
<b>7</b>	<b>Appendix</b>	<b>79</b>
7.1	Appendix 1: Drawing of mold design . . . . .	79
7.1.1	Appendix 1.1: Drawing of mold design for large scale foot . . . . .	79
7.1.2	Appendix 1.2: Drawing of mold design for small scale foot . . . . .	85
7.2	Appendix 2: Matlab code for calculation . . . . .	91

7.2.1	Morphology changing without pressing force . . . . .	91
7.2.2	Morphology changing with pressing force . . . . .	95
	<b>Bibliography</b>	<b>103</b>





# List of Figures

1	Morphology-changeable soft pads for locomotion on both dry and wet surfaces. (a) An illustration of a legged robot, highlighting the potential issue of slippage on a wet floor. (b) A conceptual representation of a robot foot equipped with a flexible and adaptable sole. (c) The manufacturing process of a robotic foot, comprising a sturdy "bone" enclosed within a soft, flexible skin, and a soft sole featuring adaptable soft pads. (d) A cross-sectional diagram of the foot, offering insights into the adaptable soft pads that are controlled via pneumatic air pressure. . . . .	2
2	Morphology-changeable soft pads foot and finite element model. (a) The improved version Morphology-changeable soft pads. (b) The morphology changeable pad foot attached hexapod-robot. (c) Concept of capillary force model on multi-dome pads. (d) finite element method model for capillary simulation. . . . .	4
3	The morphology of foot pad's structure of animals: a- Tree frog toe pad, b- Gecko toe pad, and c- Starfish tube feet . . . . .	8
4	Proposed designs and applications inspired from animals' foot pad. (a) The design of tree-trog-inspired adhesives in micro-scale [23]. (b) the artificial tube feet of starfish that exhibit robust adhesion and enable effective locomotion [24]. . . . .	9

5	A cross-sectional illustration shows the contact between two elastic spheres using three models: (a) Hertz contact, (b) JKR, and (c) DMT models. In Hertz theory, no interactions are considered, while the JKR theory accounts for surface forces only within the contact region. On the other hand, the DMT theory considers both surface forces within and attractive forces outside the contact region. Solid lines represent the contact configuration at zero load, and dashed lines represent the contact configuration when an applied load, $P$ , is present.[34] . . . . .	11
6	Soft Pad Configurations: (a) Depressurized (flat circular soft pad). (b) Pressurized (dome-shaped soft pad) without ground contact. (c) Pressurized with ground contact during walking. (d) Geometric characteristics (at constant pressures) of the soft pad with and without contact (represented by dashed lines). . . . .	15
7	The spherical surface differential explanation for tension energy: Tension energy is determined by integrating the differentials of spherical segments along the $z$ -axis. . . . .	17
8	Capillary action occurs upon contact with the wet floor, induced by a liquid layer surrounding the soft pad with a height of $h$ . In this situation, the pad exhibits a tendency to slip to the left. . . . .	25
9	Optimization solution for design. (a) phenomenon of rising wet liquid. (b) the arrange of inflated dome in the foot and the area caculation. . . . .	29
10	The graphical representation illustrates the changes in the liquid's rising height $h$ versus the initial radius $r_0$ . . . . .	32
11	Design of the soft pad. (a) Soft pad without air pressure. (b) Illustration of the soft pad design concept. (c) Soft pad under the influence of air pressure. . . . .	33
12	Experimental design for examining morphological changes. . . . .	34

13	Dome morphology dimension processed by 400-CAM058 microscope (SANWA SUPPLY): a- without applying pressing force, b- with applying pressing force. . . . .	34
14	Experiment state 1: Effects of different pressures in the soft pad without floor contact were compared using Matlab (Code matlab in Appendix 7.2.1). . . . .	35
15	Experiment state 1: dimension of dome height and dome radius. . . .	36
16	Experiment state 2: Response of the soft pad under air pressure of 75 kPa to being pressed at different forces (Code matlab in Appendix 7.2.2). . . . .	37
17	Experiment state 2: dimension of dome height and dome radius. . . .	37
18	Experiment state 2: dimension of adhesive radius and adhesive depth. . . .	38
19	Experiment to assess the resistance of the soft pad to tangential forces: (a) Setup of the experiment. (b) Soft pad under air pressure without simulated floor contact, (c) and with simulated wet floor contact. . . .	38
20	(a) Comparison of resulted tangential forces among flat soft pad, and domed pad under pressures of 65 kPa, 75 kPa, and 85 kPa, respectively; on both wet and dry floors. (b) Zoom-in range with comparison of tangential forces under dry (dashed line) and wet (solid line) conditions several air pressure values. . . . .	39
21	Comparison of capillary action in wet condition ( $F_{cap} = F_{wet} - F_{dry}$ ) between experiment (with error bars) and estimation results. . . . .	40
22	Wet process: (a) Soft contact between 2 object. (b) Liquid molecular of wet-adhesion phenomenon in the first time. (c)Wet-adhesion phenomenon in process . (d) Equilibrium state. . . . .	45
23	(a) Wet adhesion phenomenon in general geometry object. (b) Differentials of liquid following polar coordinates. . . . .	46

24	(a) The geometric parameters of the differential element of the liquid mass in polar coordinate system. (b) The 2D projection of the differential element of the liquid mass onto its own normal plane. . . . .	50
25	The algorithm of finite element method for estimation of capillary force.	53
26	SOFA simulation for capillary phenomenon. Note that red dotted boundaries show the uplifted water layer due to adhesion. (a) Dome shape object. (b) Truncated cone shape object. (c) General geometry object . . . . .	54
27	Tangential capillary force estimation following the wetted liquid and movement direction, where $S_{section}$ is the projected area of the wetting liquid on a plane perpendicular to the direction of motion. . . . .	54
28	Wet adhesion parameters simulating in case of $\gamma_l = 0.004 \text{ N/m}^2$ with the rising of $\gamma_s$ (simulation using SOFA.) . . . . .	54
29	The relationship between surface tension energies and wetted height.	55
30	The relationship between wetted height and radius of wetted liquid curvature. . . . .	55
31	SOFA simulation of wet liquid for soft pads foot. (a) Changeable soft pads foot meshing in SOFA. (b) Height of rising wet liquid. . . . .	57
32	Experimental setup of the tangential force. . . . .	59
33	Microscopic images of the experimental soft plastic layer surface: (a) presents the projection of the convex elevation on the rough surface, (b) shows the projection of the roughness density on the rough surface, (c) demonstrates the projection of the smooth surface, (d) displays the projection of the roughness density on the smooth surface.	60
34	(a) Comparison of resulted tangential forces among flat soft pads foot, and domed pads on both wet and dry floors in two different roughness. (b) Comparison of capillary action in wet condition ( $F_{cap} = F_{wet} - F_{dry}$ ) between experiment (with error bars) and estimation results.	61

35	Fabrication procedure: (a) Arrangement of the foot mold. (b) Pouring of silicone material. (c) Finalizing the foot structure. (d) Soft pad with applied pressure and dimensions. . . . .	64
36	Fabrication process: (a) mold set of foot. (b) Pouring silicone include two step: pouring Dragon Skin 30 silicone for the body, then pouring the silicone Ecoflex 00-20 for the thin sheet. (c) Finishing the foot. (d) dome inflation and the robot leg attached the foot. . . . .	65
37	Design of the robotic leg. (a) The walking system with its components. (b) Mechanical analysis of the linkage system for walking tests on both (c) dry and (d) wet floors (contour data was tracked to generate the foot paths in Fig. 38). . . . .	67
38	Tracked foot's posture (the rectangle in Fig. 37d) during walking action in (a) on a dry floor, (b) on a wet floor with flat foot, and (c) on a wet floor with domed pad (high inner pressure state). . . . .	68
39	Results of the walking robot's body displacement in five experimental conditions (tracked by the marker on the robot body as shown in Fig. 12d). . . . .	68
40	3-Degree-of-Freedom Hexapod robot in the experiment: (a) Hexapod robot with attached markers, (b) leg mechanism illustration. (c) The concept of hexapod locomotion showcased. . . . .	70
41	The positions of the detected markers on leg 2 and leg 5 of the hexapod while walking on the rough surface, illustrating instances of slippage in different scenarios: walking on dry surface with flat foot, walking on wet surface with flat foot, walking on wet surface with dome pad foot. . . . .	72
42	The positions of the detected markers on leg 2 and leg 5 of the hexapod while walking on the smooth surface, illustrating instances of slippage in different scenarios: walking on dry surface with flat foot, walking on wet surface with flat foot, walking on wet surface with dome pad foot. . . . .	72

43	The positions of the detected markers on the body of the hexapod while walking on the rough surface in different scenarios: walking on dry surface with flat foot, walking on wet surface with flat foot, walking on wet surface with dome pad foot. . . . .	73
44	The positions of the detected markers on the body of the hexapod while walking on the smooth surface in different scenarios: walking on dry surface with flat foot, walking on wet surface with flat foot, walking on wet surface with dome pad foot. . . . .	74
45	Designed mold and completed foot in large and small scale. . . . .	76

# 1 Introduction

Recently, biomimetic research has become popular in various engineering applications [1]. This problem-solving approach, often inspired by nature, not only helps create innovative solutions but also allows exploring biological hypotheses that are difficult or impossible to test on live organisms [2]. Besides offering practical engineering insights, biomimetic research enhances our understanding of the basic physics behind different phenomena. This knowledge is particularly valuable in situations where ethical or systematic concerns restrict experimentation on animals.

Among the numerous biomimetic approaches, one area has recently garnered significant interest: the concept of morphological adaptation to changing environmental conditions. This approach focuses on creating functional, adaptive structures that can modify their shape, stiffness, or properties in response to different scenarios. These morphological changes provide a compelling basis for various applications [3]. Researchers are increasingly exploring how animals adapt their morphology to suit their surroundings. This form of adaptation, often referred to as "morphological design," has become a topic of intensive investigation [4].

This research in biomimetics has delved into the details of tribological phenomena, focussing on various aspects of animal adaptation to their environments. For instance, studies have examined how human fingers achieve exceptional friction and dexterity when grasping objects, the dry locomotion capabilities of gecko toes [5], and how tree frog toes are optimized for wet gripping [6]. The findings from these studies have practical uses in engineering, especially in creating grippers and adhesion systems. As we understand more about how these animals effectively use their morphology, we gain insights into optimizing mechanisms that enable robots to interact more effectively with their environment. The ability of actively changing



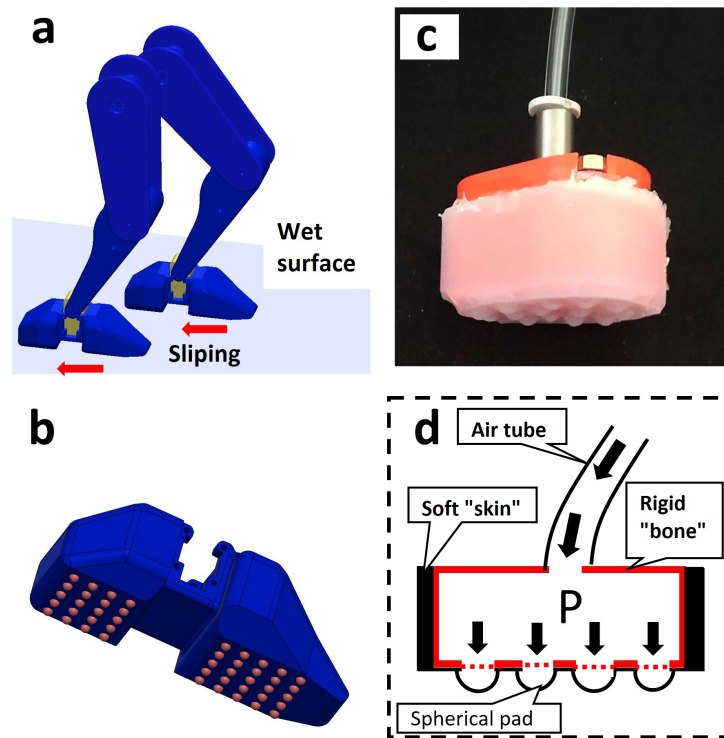


FIGURE 1: Morphology-changeable soft pads for locomotion on both dry and wet surfaces. (a) An illustration of a legged robot, highlighting the potential issue of slippage on a wet floor. (b) A conceptual representation of a robot foot equipped with a flexible and adaptable sole. (c) The manufacturing process of a robotic foot, comprising a sturdy "bone" enclosed within a soft, flexible skin, and a soft sole featuring adaptable soft pads. (d) A cross-sectional diagram of the foot, offering insights into the adaptable soft pads that are controlled via pneumatic air pressure.

morphology to adapt to the environment is also an important aspect of embodied robots, which is an interesting trend. The concept of embodied robotics is grounded in the idea that intelligence and cognition are tightly linked to physical embodiment and interaction with the environment [7]. By having a physical presence, these robots can engage with the world in a manner similar to living organisms, allowing them to adapt to changing conditions and navigate complex environments.

One interesting example of this type of adaptation comes from starfish. They can pump water into their tubular limbs through a sieve plate within their skin, thereby altering the shape, stiffness, and posture of their limbs to enhance their locomotion [8]. This morphological adaptation allows them to harness the principles of tribology effectively and facilitate adhesion between their limbs and the surfaces they navigate, especially in complex, irregular terrains [9]. This adaptation seems to be a crucial factor in their ability to adapt to challenging environments, a principle that

may hold significance for legged robots as they navigate dynamic, unpredictable surfaces.

Building on these insights, we propose a novel mechanics of morphology changeable soft pad that takes advantage of adapting its morphology to optimize tribological interactions, such as friction, adhesion, and, notably, wet adhesion. Fig. 1 illustrates the concept of this research. Wet adhesion plays a crucial role when robots operate on wet surfaces, where slippage can be a challenge (see Fig. 1a). Our robotic foot incorporates a novel design of soft pad that can adapt its morphology, enhancing the foot's performance on both dry and wet surfaces. (see Fig. 1b, d).

To provide a theoretical concept for this mechanic, we have developed an analytical model that examines the interaction between the foot's morphology and the conditions of ground contact. This model takes into account factors such as shape, size, and stiffness of the foot. Furthermore, by actively adjusting the morphology of the foot's soft pads to adapt to different surface conditions, we emphasize the critical role that morphological features play in the locomotion of legged walking robots.

Besides, slippage is a significant challenge for legged robots, particularly when they walking on wet surfaces [10]. Various research studies have explored the potential of improving robotic stability by using friction, adhesion, and capillary forces. Notably, bio-inspired feet with small-scale, soft pads have successfully used capillary forces to enhance robot mobility, mimicking the locomotion of animals such as tree frogs on wet surfaces [11]. Additionally, some studies have introduced perspectives on wet adhesion, inspired by the adhesive capabilities of mussels [12].

However, while these bio-inspired foot designs have led to significant improvements in robot stability, there remains a gap in our understanding of the underlying physics. A universal analytical model that reveals not only the performance of robot feet but also the mechanisms at play in the natural world is still lacking. The fundamental principles describing capillary forces in wet adhesion are still a challenge, due to the complicated interaction between the foot's pads, the liquid, the surrounding surface, and vapor [13]. Existing analytical models are often limited to

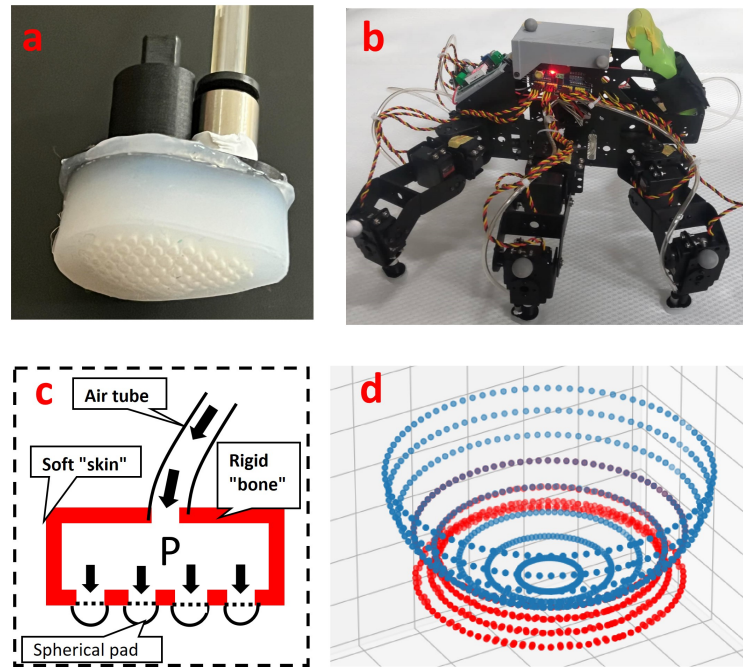


FIGURE 2: Morphology-changeable soft pads foot and finite element model. (a) The improved version Morphology-changeable soft pads. (b) The morphology changeable pad foot attached hexapod-robot. (c) Concept of capillary force model on multi-dome pads. (d) finite element method model for capillary simulation.

specific geometrical shapes that are readily incorporated into calculations [14], [15]. Furthermore, the arrangement and distribution of these pads are acknowledged as significant factors in enhancing capillary force [16]. However, this element has not been directly incorporated into the capillary force equation. Because of the complicated capillary interactions between objects on wet surfaces, the Finite Element (FE) method has become a useful tool for simulating how liquids behave, especially when it comes to wet adhesion and capillary forces.

To address these challenges, we present an analytical model that employs the Finite Element method, thoroughly explores the equilibrium state of energy related to the liquid's geometric surface. Besides, we also proposed an improved robot foot design featuring smaller dome pads to maximize the capillary force's effectiveness and enhance the robot's locomotion. This research also calculates the capillary force values, which depend on the geometric characteristics and distribution of the domes on the foot. Fig. 2 illustrates this purpose, which focuses on another design to optimize the capillary force (Fig. 2a, c). Besides, Fig. 2b shows the application of the foot in hexapod robot. Finally, Fig. 2d introduce the result of finite element method

base model for simulation of capillary.

This study employs the Simulation Open Framework Architecture (SOFA) to construct an analytical model, effectively meshing solid objects and considering every element of the liquid's energy equilibrium state. The analytical model's accuracy is validated through force measurement experiments, ensuring its accuracy and reliability. Finally, we evaluate the effectiveness of the robotic foot through a series of showcase experiments, including scenarios involving locomotion on both dry and wet surfaces.

In summary, this research contributes to our understanding of biomimetic adaptations, morphological design, and the role of tribological phenomena in optimizing the performance of legged robots. Learning from both nature and engineering helps us create a solution for robot feet. It highlights the importance of models that connect theoretical understanding with practical application. This result could lead to improvements in robotics, contributing to the development of robots capable of effective and stable locomotion across a range of surfaces.

In this chapter, I have introduced the overall concept and philosophy of the dissertation, emphasizing the physical meaning, impact, and goals of this research. In the next chapter, related works that form the concept for our research will be explained in detail.



## 2 Background and Related Works

In this study, a novel mechanics of morphology changeable soft pad were introduced with demonstrated designs and experiments. This mechanics draws its inspiration from the morphological features and bio-inspired structures found in animals' foot pads, which have been extensively explored and employed across diverse applications. Subsequently, a soft contact mechanical model was employed to reveal the fundamental physical concepts underlying the contact phenomenon within this mechanics and design. Furthermore, the finite element method was used to provide a solution for simulating and assessing wet adhesion and capillary effects within our research-focused contact phenomenon.

### 2.1 Morphology and bio-inspired structure of animals' food pad with adhesion and capillary

Researchers have drawn insights from animal footpads, driving advancements in adhesion mechanisms. Nature's adaptations have been a source of inspiration, resulting in practical applications. For example, the tree frog's toe pads display a distinctive feature – velocity-dependent shear resistance. This trait has proven valuable in the development of wet adhesion methods, contributing to bio-inspired technology [17], [18]. The authors unveiled the significant potential in the concept of the tree frog's foot pad, providing a novel approach applicable to a wide array of contexts.

In a similar case, gecko toe pads have undergone extensive research due to their hierarchical structure. These intricate feet have not only been closely studied but

have also been employed in developing dry adhesion mechanisms [19], [20]. Moreover, geckos can adjust their hydrophobicity in humid environments, enhancing adhesion and stabilizing friction, highlighting the adaptability of these structures in various conditions [21]. These examples emphasize the potential of nature-inspired designs in engineering and technology. Similarly, echinoderm tube feet give another interesting direction for exploration. These remarkable appendages enable creatures to navigate challenging terrains like sand, stone, or underwater surfaces with remarkable grace and efficiency [22].

Taking inspiration from the natural world, researchers have proposed bio-inspired designs for significant applications in various fields, including robotics and medicine. Authors in [23] proposed design of tree-trog-inspired adhesives in micro-scale to exploit the capillary and adhesion in different applications. Through meticulous design and fabrication, researchers have created artificial tube feet of starfish that exhibit robust adhesion and enable effective locomotion, promising innovative solutions in various applications [24]. Soft pad claw robots have successfully integrated the flexible morphology of soft pads to achieve impressive results. These robots can climb rough vertical surfaces, showcasing the potential of nature-inspired adhesion designs [25]. Furthermore, a quadruped insect-scale robot uses capillary and

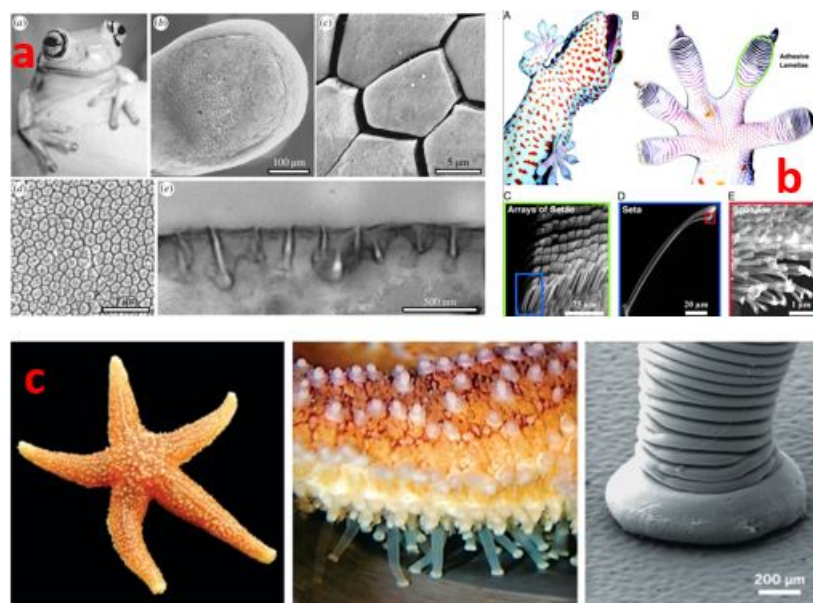


FIGURE 3: The morphology of foot pad's structure of animals: a- Tree frog toe pad, b- Gecko toe pad, and c- Starfish tube feet



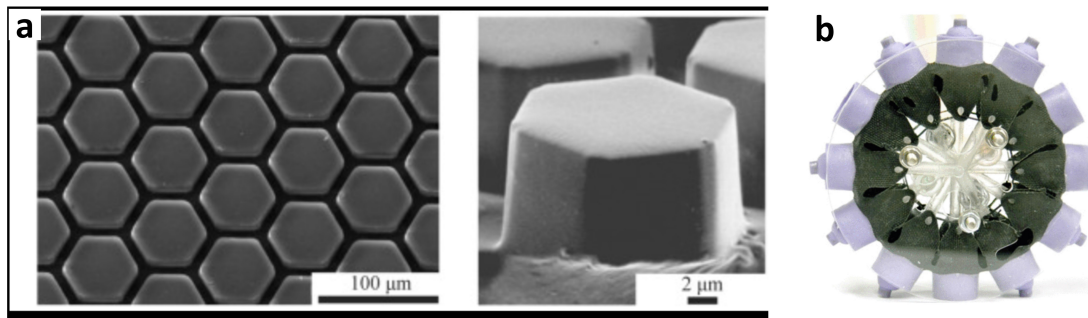


FIGURE 4: Proposed designs and applications inspired from animals' foot pad. (a) The design of tree-trog-inspired adhesives in micro-scale [23]. (b) the artificial tube feet of starfish that exhibit robust adhesion and enable effective locomotion [24].

lubrication effects to tackle inclined climbing tasks, underlining the versatility of bio-inspired strategies in robotics [26].

These examples emphasize the impressive adaptability of animal foot pads, showcasing their significant ability to use adhesion mechanisms in various engineering applications. This adaptability has evolved over millions of years, with nature finely honing footpad structures in response to unique environmental challenges.

These examples underline that animal foot pads possess versatile properties capable of reshaping engineering adhesion concepts. Researchers, inspired by natural design, are committed to exploring and applying these insights. Their aim is to incorporate biological lessons into practical solutions that connect biology with advanced technology. As this collaboration progresses, it holds the potential to bring about significant advancements in various scientific and engineering fields, from robotics to material science. This collaboration aims to strengthen the connection between the insights from nature and human innovation.

## 2.2 Contact mechanics models for elastic material

The study of soft contact locomotion, seen in the soft pads of animals and evolving robot designs, uncovers a fascinating area marked by a complex interplay of features like adhesion, friction, capillary action, and Van der Waals forces. Understanding the roles and physical concepts of these factors in different situations is a challenging scientific puzzle. Adding complexity, many natural foot pads are soft,



adaptable, and flexible. These abilities help them move easily on different surfaces, like tree bark, slippery leaves, or rough rocks. In robotics, this adaptability is a significant tool that helps animals live in their habitat. Researchers want to study from these natural abilities, making robots more versatile and innovative. Understanding how soft contact locomotion works can give us new ideas in fields like robotics and material science.

To solve that problem, one approach is to construct a capillary-action model using elastic materials. Building upon theories such as Hertz theory, Johnson-Kendall-Roberts, Derjaguin–Muller–Toporov, and Tabor (Fig. 5), we have gained insights into a multitude of contact conditions that soft bodies can exhibit [27]–[29]. Fig. 5 illustrate the development of contact mechanics theories. In Hertz theory, no interactions are considered, while the JKR theory accounts for surface forces only within the contact region. On the other hand, the DMT theory considers both surface forces within and attractive forces outside the contact region. The Maugis-Dugdale theory has added a crucial analytical perspective by providing valuable data on interactions in the intermediate regions, where Tabor’s result has moderate values [30]. Those results contributed important knowledge into soft contact mechanics.

In our earlier studies, we delved into how soft materials interact in wet conditions, especially concentrating on micro-patterned pads [31]. Taking inspiration from how tree frog toes stick, we explored creating and trying out a pad shape that can grip thin hemispherical shells using wet adhesion [32], [33]. These inquiries, inspired by nature, have opened up possibilities for robots to adjust their movement based on the environment.

In the field of soft contact, there’s an interesting aspect related to adhesives inspired by tree frogs. These adhesives provide researchers with an exciting opportunity to investigate the limitless possibilities of technology inspired by nature [35]. They often feature a micropillar pattern connected via a soft homogeneous base layer to a rigid support. The pioneering works of researchers like Drotlef et al. and Langowski et al. brought forward these designs [23], [36]. These advancements

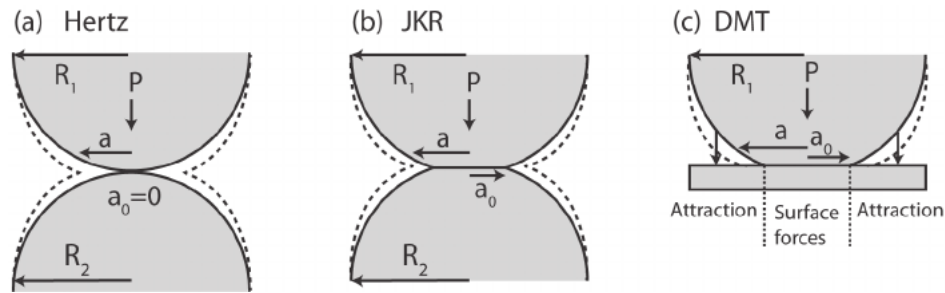


FIGURE 5: A cross-sectional illustration shows the contact between two elastic spheres using three models: (a) Hertz contact, (b) JKR, and (c) DMT models. In Hertz theory, no interactions are considered, while the JKR theory accounts for surface forces only within the contact region. On the other hand, the DMT theory considers both surface forces within and attractive forces outside the contact region. Solid lines represent the contact configuration at zero load, and dashed lines represent the contact configuration when an applied load,  $P$ , is present.[34]

haven't just stayed in the scientific contributions but have been used in practical applications, significantly affecting the detection of slipping and enhancing industrial applications [37]. For example, the legged walking robot introduced by Bloesch et al. [38] changed how slip detection algorithms work, making them more accurate and efficient by focusing on the robot's perspective of the situation.

## 2.3 Finite Element method for wet adhesion and capillary

Wet adhesion and capillary forces represent a fundamental challenge that stems from the complex interaction between solid and liquid interfaces [39]. Recent research by scholars like Gholamreza and Majid has focussed on the effects of groove height, width, and contact angles on capillary phenomena [40]. The complexity that arises when solids interact with liquids, especially in scenarios featuring complex solid geometries, has led to adopting the Finite Element (FE) method as a powerful tool to study these intricate phenomena [41]. Luo et al. [42] used the FE method to develop a numerical simulation model for droplet spreading on topologically rough surfaces. Moreover, a prior study [43] delved into the deformation of a two-dimensional spherical liquid droplet on a horizontal surface. This study presented

a mathematical model that described the deformation, using the time-dependent Navier-Stokes equations in a time-dependent domain.

Over the past several decades, the finite element method (FEM) has proven to be a crucial tool in simulating a wide range of physical phenomena [44], and this holds true for research into wet adhesion and capillary action in the realm of robotics. The finite element method involves discretizing complex systems into smaller, more manageable elements and solving mathematical equations for each element. In the context of wet adhesion and capillary effects, this computational technique offers a powerful means of modeling and predicting the behavior of liquid interactions with various surfaces.

One of the primary areas where FEM has made significant contributions is in understanding how capillary forces play a role in the adhesion of soft materials to surfaces [45]. This is particularly relevant in the design of robots that need to maintain stable contact with surfaces in wet environments. FEM simulations allow researchers to investigate how capillary forces affect the interaction between soft materials and surfaces under different conditions [46].

This insight is invaluable for designing robots that can effectively navigate and interact with both dry and wet surfaces. FEM simulations have also been an important method to investigate the mechanics of wet adhesion and capillary forces in more intricate environments [47]. For example, when designing robots that can adapt to complex terrains, such as rocky landscapes or underwater environments, researchers employ FEM to model the interactions of fluids with irregular surfaces. These simulations help engineers optimize the adhesion mechanisms to ensure that the robots can securely adhere to the surfaces they encounter [48]. Moreover, FEM enables the evaluation of the effect of various parameters, such as surface roughness and liquid properties, on adhesion, leading to more accurate and adaptable robotic designs [49]. The collaboration between Finite Element Method (FEM) and wet adhesion research contributes to creating novel robotic systems [50]. It facilitates the creation of soft robots capable of scaling walls, adhering to irregular surfaces, and performing tasks in challenging environments where traditional rigid robots would

struggle [51]. The results from FEM simulations help design soft robot parts that can effectively use capillary forces to stick, even on wet or uneven surfaces.

In summary, finite element simulations play an important role in researching wet adhesion and capillary phenomena in the field of robotics. These simulations help us understand how these forces influence the interaction between robots and surfaces, leading to the development of more adaptable, efficient, and versatile robotic systems capable of performing tasks in a variety of environments, including those involving liquids and irregular surfaces. This approach brings together engineering, material science, and computer science, promoting the advancement of robotic technology.

## 2.4 The contribution of this thesis

In this research, we focus on exploring both the theory and real-world aspects of soft pads with actively morphology adaptations. To bring these concepts to practical applications, we employ both the analytical model and the Finite Element (FE) method, a robust tool, to achieve stable locomotion for our robot foot in both cases of dry and wet surfaces. The main goal is to understand how a flexible shape can significantly improve the stability of the foot when it moves on different surfaces. The important findings of this research are explained below:

- We present a mechanics of morphology changeable soft pad that can actively change the morphology to adapt to the environment. This concept is an important aspect of embodied robot which is grounded in the idea that intelligence and cognition are tightly linked to physical embodiment and interaction with the environment.
- We suggest designing a soft pad capable of transitioning from a flat elastic sheet in the foot sole (suitable for walking in dry conditions) to a raised spherical dome, which enhances walking efficiency on wet surfaces.

- An analytical model is proposed to investigate the morphology of the soft pad, delving into the complexities of tribological aspects, including friction, adhesion, and capillary action. The findings of our study indicate that, in comparison to the significant size of our robot's foot, capillary action plays a relatively minor role when compared to friction and adhesion. Nevertheless, we anticipate that in smaller-scale applications, capillary action could become more significant. We plan to explore this aspect further in our future work.
- A mathematical model, based on the FE method, is proposed to delve into capillary action, and its findings are validated through force measurement experiments.
- Practical experiments involving a robot foot equipped with these soft pads are presented, showcasing their capacity to enhance walking efficiency across diverse terrains. In this research, we introduce the soft pad foot designs for robots in both large and small scale, specifically engineered to enhance walking efficiency on wet surfaces.
- We conduct practical experiments involving a hexapod robot equipped with these adaptive soft pads, thereby highlighting their substantial contribution to enhancing walking efficiency.

In conclusion, this research has explored the aspects of soft contact locomotion, wet adhesion, and capillary forces, revealing novel possibilities. These possibilities may be used in practical applications to improve the stability and adaptability of robotic systems in different environments. This work represents the collaboration of biological inspiration with technological applications, providing solutions for solving recent problems.

# 3 Bioinspired robotic foot facilitating wet adhesion

## 3.1 ANALYTICAL MODEL

### 3.1.1 Morphology computation model

The conceptual mechanics of morphology changeable soft pad , along with a prototype foot equipped with soft pads (illustrated in Fig. 1), represents a important aspect of this study. These soft pads, integrated into the sole of the foot, possess an adaptability feature that enhances walking performance on wet surfaces. This adaptability is achieved through the controlled application of compressed air, causing a transformation in the morphology of the soft pads. In this section, we delve into the theoretical underlying of this transformative process, explaining the fundamental principles of interaction of these soft pads with a wet floor.

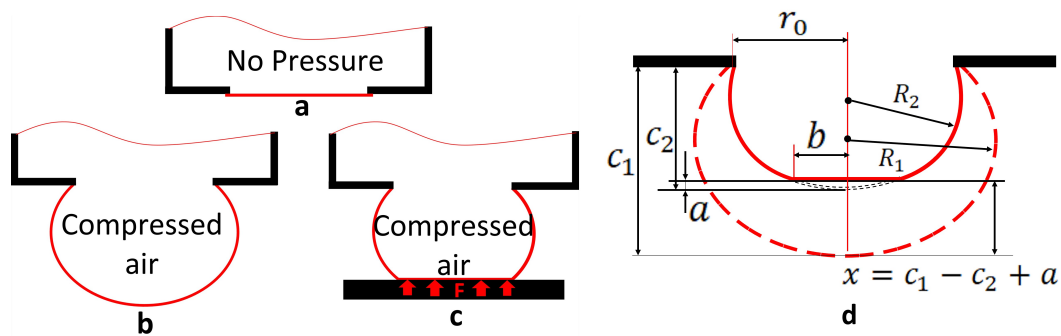


FIGURE 6: Soft Pad Configurations: (a) Depressurized (flat circular soft pad). (b) Pressurized (dome-shaped soft pad) without ground contact. (c) Pressurized with ground contact during walking. (d) Geometric characteristics (at constant pressures) of the soft pad with and without contact (represented by dashed lines).

As the robot walks, an inflated soft pad comes into contact with the floor, exerting a contact force represented by  $F$ . To comprehensively understand this interaction, we first discuss an analytical model that delves into the relationships between the morphology of the soft pad and the values of  $F$  and air pressure, denoted as  $p$ . The various states of a soft pad are illustrated in Fig. 6(a-c): in its initial state, where no pressure is applied, it remains a flat circular sheet; upon inflation by air pressure, it transforms into a spherical dome. Next, when this dome pad makes contact with a floor, the contact force acting on the pad causes the pad's condition to shift from a state of high potential equilibrium (characterized by a spherical shape with a resultant volume  $V_1$ ) to a lower potential state. In this lower potential state, the pad assumes the form of a thin elastic sheet, as depicted in Fig. 6(d). Examining the energy equation during this process, the work of the pressing force on the foot ( $W_F$ ) will be equal to the total work of various force components arising throughout the process, including: the work to push a portion of the air mass out of the dome ( $W_p$ ), the work of the elastic sheet's tension force ( $W_{Ten}$ ), and the work of the dry adhesive force ( $W_{ad}$ ).

$$W_F = W_p + W_{Ten} + W_{ad}. \quad (3.1)$$

The work  $W_p$  is equal to the difference of potential energy stored in the compressed air ( $\Delta U_p$ ), which can be estimated using the following expression:

$$W_p = \Delta U_p = pV_1 - pV_2. \quad (3.2)$$

Based on the geometric properties displayed in Fig. 6(d), we can calculate the volumes at the two states of the dome as follows:

$$V_1 = \frac{\pi}{6}c_1(3r_0^2 + c_1^2), \quad (3.3)$$

$$V_2 = \frac{\pi}{6}c_2(3r_0^2 + c_2^2) - \frac{\pi}{6}a(3b^2 + a^2). \quad (3.4)$$

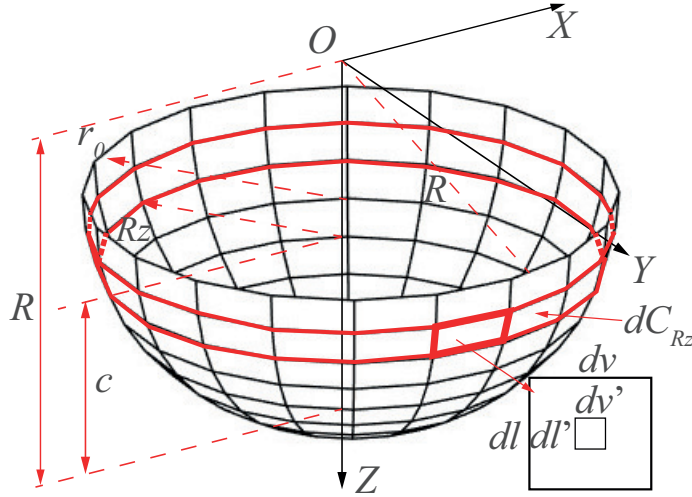


FIGURE 7: The spherical surface differential explanation for tension energy: Tension energy is determined by integrating the differentials of spherical segments along the z-axis.

Thus,  $\Delta U_p$  can be estimated as :

$$\Delta U_p = pV_1 - p\frac{\pi}{6}c_2(3r_0^2 + c_2^2) + p\frac{\pi}{6}a(3b^2 + a^2). \quad (3.5)$$

Examining the work of tension force which is equal to the difference in elastic tension energy  $W_{Ten} = U_{te} - U_{te_0}$ , where  $U_{te_0}$  is the tension energy of dome without pressing force. So, at the energy balancing state, we have  $U_{te_0} = pV_1$ .

Next, we examine the tension energy  $U_{te}$  at the spherical dome surface as the potential strain energy of an elastic sheet under constraint. The classic model presented by [52] for representing the inflation of an elastic balloon doesn't directly apply to the specific portion of the pad, i.e., the spherical dome shape, given the related constraints. In this context, we introduce a new definition of tension energy as the elastic energy stored within the thin sheet when stretched in all directions (refer to Fig. 7).

Let's consider an differential area  $dv' dl'$  on the sheet's surface located at a height of  $(R - c)$  along the Z-axis within the coordinate system  $O - XYZ$ . This area falls within the region highlighted in red, having a radius of  $R_z$ . We can assume that under low air pressure, this area undergoes stretching to become  $dv dl$  at the same height (with the value of  $R_z$  remaining constant). Consequently, the work required



for this stretching is confined to the  $XY$ -axes, as indicated below:

$$dU_{te} = dW_x + dW_y = \frac{1}{2}Tdu_xdu_y + \frac{1}{2}Tdu_ydu_x, \quad (3.6)$$

where  $u_x, u_y$  is the displacement of a differential element of the sheet following  $x$ -axis,  $y$ -axis. Here,  $T$  represents the elastic tension in the thin sheet. Assuming uniform deformation of the thin sheet at all points and in all directions, the elongation along the  $XY$ -axes can be estimated as follows:

$$du_x = du_y, \quad (3.7)$$

$$d(l - l') = d(v - v'), \quad (3.8)$$

$$dl = dv. \quad (3.9)$$

Taking into account the deformation of the sphere, we divide the sphere into segments denoted as  $dC_{R_z}$ . Consequently, the tension potential integrates the work required for the deformation of each soft pad segment along the  $Z$ -axis:

$$dU_{te} = dW_x + dW_y = \frac{1}{2}Tdu_xdu_y + \frac{1}{2}Tdu_ydu_x, \quad (3.10)$$

$$\text{Because } du_x = du_y = d(l - l_0) = d(v - v_0) = dl = dv, \quad (3.11)$$

$$\text{So } dU_{te} = Tdl dv, \quad (3.12)$$

$$\text{then } dW_{r_z} = \int_{dC_{R_z}} dU_{te} = TdC_{R_z}, \quad (3.13)$$

Where:

- $U_{te}$  is the tension energy.
- $T$  is the elastic tension of the thin sheet.
- $dv$  represents the differential of area.
- $dl$  is the differential of length.
- $R_z$  signifies the radius of the red-colored band, which remains constant.

- $R$  denotes the original radius of the sphere.
- $c$  stands for the thickness of the thin sheet.

This approach allows us to quantify the tension energy for this specific constraint-driven deformation of the soft pad segment along the Z-axis. By integrating the work associated with the deformation of the soft pad segment along the z-axis, we can estimate the tension potential as follows:

$$U_{te} = \int_S dW_{r_z} = \int_S 2\pi R_z T dl. \quad (3.14)$$

Subsequently, the differential variable  $dl$  is expressed as a function of the differential variables  $dx$  and  $dz$ :

$$dl = \sqrt{dx^2 + dz^2}, \quad x = \sqrt{R^2 - z^2}, \quad (3.15)$$

$$dx = \frac{-z}{\sqrt{R^2 - z^2}} dz. \quad (3.16)$$

So, the differential variable  $dl$  is summarized as below:

$$dl = \sqrt{\frac{z^2}{R^2 - z^2} dz^2 + dz^2}, \quad (3.17)$$

$$= \frac{R}{\sqrt{R^2 - z^2}} dz. \quad (3.18)$$

The radius of the round segment of the sphere following the z-axis is represented as a function of the spherical radius and the z-coordinate.

$$\text{And } R_z = \sqrt{(R^2 - z^2)}. \quad (3.19)$$

Insert Eq. 3.18, 3.19 into Eq. 3.14, we have:

$$U_{te} = \int_{R-c}^R 2\pi \sqrt{(R^2 - z^2)} T \frac{R}{\sqrt{R^2 - z^2}} dz, \quad (3.20)$$

$$= \int_{R-c}^R 2\pi TR dz, \quad (3.21)$$

$$= 2\pi TRz \Big|_{R-c}^R, \quad (3.22)$$

$$= 2\pi TRc. \quad (3.23)$$

Because  $2Rc = r_0^2 + c^2$ , the tension potential is summarized as below:

$$U_{te} = \pi T(r_0^2 + c^2). \quad (3.24)$$

We consider the tension  $T$  when the soft pad inflates:

$$dl = du + dl', \text{ and } dv = du + dv'. \quad (3.25)$$

The elastic tension that is considered for each element of differential of sphere area:

$$T = k \frac{du}{dl'} = k \frac{du}{dv'}, \quad (3.26)$$

$$= k \frac{dl - dl'}{dl_0} = k \frac{dv - dv'}{dv'}, \quad (3.27)$$

$$= k \left( \frac{dl}{dl'} - 1 \right) = k \left( \frac{dv}{dv'} - 1 \right), \quad (3.28)$$

$$\text{So } \frac{T}{k} + 1 = \frac{dl}{dl'} = \frac{dv}{dv'}. \quad (3.29)$$

Then, we have:

$$T = k \left( \frac{dl}{dl'} - 1 \right), \quad (3.30)$$

$$= k \left( \frac{dv}{dv'} - 1 \right). \quad (3.31)$$

$$\text{So } \left( \frac{T}{k} + 1 \right)^2 = \frac{dl dv}{dl' dv'} = \frac{dS}{dS'}. \quad (3.32)$$

$$\text{Then, } T = k \frac{\sqrt{S} - \sqrt{S'}}{\sqrt{S'}}. \quad (3.33)$$

In step 1 when the spherical pad is inflated by inner pressure without any pressing force, We have:

$$S = \pi (r_0^2 + c_1^2), S_0 = \pi r_0^2, \quad (3.34)$$

$$\text{So } T = k \frac{\sqrt{r_0^2 + c_1^2} - r_0}{r_0}. \quad (3.35)$$

$$(3.36)$$

Insert into Eq. 3.24:

$$U_{te} = \pi k \frac{\sqrt{r_0^2 + c_1^2} - r_0}{r_0} (r_0^2 + c_1^2). \quad (3.37)$$

In step 2 when the spherical pad is inflated by inner pressure with a pressing force, We have:

$$S = \pi (r_0^2 + c_2^2 - a^2), S_0 = \pi r_0^2, \quad (3.38)$$

$$\text{So } T = k \frac{\sqrt{r_0^2 + c_2^2 - a^2} - r_0}{r_0}. \quad (3.39)$$

This result leads to the potential energy for state 1 of a spherical soft pad as below:

$$U_{te} = \pi k \frac{\sqrt{r_0^2 + c_1^2} - r_0}{r_0} (r_0^2 + c_1^2). \quad (3.40)$$

Besides, the potential energy for state 2 of the spherical soft pad is built based on geometrical parameters in this case:

$$U_{te} = \pi k \frac{\sqrt{r_0^2 + c_2^2 - a^2} - r_0}{r_0} (r_0^2 + c_2^2 - a^2). \quad (3.41)$$

So the work of tension force is estimated as below:

$$W_{Ten} = \Delta U_{te} = \pi k \frac{\sqrt{r_0^2 + c_2^2 - a^2} - r_0}{r_0} (r_0^2 + c_2^2 - a^2) - pV_1. \quad (3.42)$$

The work of adhesive force is defined:

$$W_{ad} = \gamma_{12}\pi b^2. \quad (3.43)$$

Insert Eq. 3.5, 3.41, 3.43 into Eq. 3.1, we have:

$$\begin{aligned} W_F &= \int F dz \\ &= -p \frac{\pi}{6} c_2 (3r_0^2 + c_2^2) + p \frac{\pi}{6} a (3b^2 + a^2) + \pi k \frac{(r_0^2 + c_2^2 - a^2)^{\frac{3}{2}}}{r_0} \\ &\quad - \pi k (r_0^2 + c_2^2 - a^2) + \gamma_{12}\pi b^2. \end{aligned}$$

Equilibrium state will obtain when:

$$\frac{dW_F}{db} = 0, \quad (3.44)$$

$$\text{so: } \frac{dW_F}{db} = \frac{dW_F}{db} + \frac{dW_F}{dz} \frac{dz}{db} = 0, \quad (3.45)$$

with  $z$  is a function over  $c_2$  and  $a$ :  $z = c_1 - c_2 + a$ .

The pressing force is the derivation of total energy over a variant of displacement following the  $z$ -axis.

$$\frac{dW_F}{dz} = F, \quad (3.46)$$

$$\frac{dz}{db} = \frac{d(c_1 - c_2 + a)}{db} = \frac{da}{db}. \quad (3.47)$$

Due to the geometrical constraint, the penetration depth  $a$  can be expressed as follows:

$$a = R_2 - \sqrt{R_2^2 - b^2}. \quad (3.48)$$

The result of derivation leads to the equation as below:

$$\pi \left( pR_2 - p\sqrt{R_2^2 - b^2} + 2\gamma_{12} \right) \sqrt{R_2^2 - b^2} - F = 0. \quad (3.49)$$

Because  $a \ll R_2, b \ll R_2$ , we have  $\sqrt{R_2^2 - b^2} \approx R_2$ , so:

$$p\pi \left( R_2 - \sqrt{R_2^2 - b^2} \right) \sqrt{R_2^2 - b^2} + 2\gamma_{12}\pi \sqrt{R_2^2 - b^2} - F = 0, \quad (3.50)$$

$$p\pi R_2^2 - p\pi R_2^2 + p\pi b^2 + 2\gamma_{12}\pi R_2 - F = 0, \quad (3.51)$$

$$\text{and: } p\pi b^2 + 2\gamma_{12}\pi R_2 - F = 0. \quad (3.52)$$

Finally, the radius of contact area can be expressed as follows:

$$b = \sqrt{\frac{F - 2\gamma_{12}\pi \left( \frac{r_0^2 + c_2^2}{2c_2} \right)}{p\pi}}. \quad (3.53)$$

We consider the force that presses into the surface at the equilibrium of state 2.

$$F = \frac{dW_F}{dz} \quad (3.54)$$

$$= \frac{dW_F}{da} \frac{da}{dz} + \frac{dW_F}{dc_2} \frac{dc_2}{dz} + \frac{dW_F}{db} \frac{db}{dz}. \quad (3.55)$$

As below, we have:

$$z = c_1 - c_2 + a, \frac{dz}{db} = 0, \quad (3.56)$$

$$F = \frac{dW_F}{da} - \frac{dW_F}{dc_2}, \quad (3.57)$$

By the condition of Eq. 3.44 and Eq. 3.48:

$$F = \frac{p\pi}{2} \left( b^2 + a^2 + r_0^2 + c_2^2 \right) - \frac{3k\pi}{r_0} (c_2 + a) \sqrt{r_0^2 + c_2^2 - a^2} + 2k\pi (a + c_2). \quad (3.58)$$

Here, we found a homogeneous constrain as follows:

$$\begin{cases} (R_2 - c_2)^2 + r_0^2 = R_2^2 \\ \rightarrow R_2 = \frac{r_0^2 + c_2^2}{2c_2}, \\ (R_2 - a)^2 + b^2 = R_2^2 \\ \rightarrow R_2 = \frac{a^2 + b^2}{2a}. \end{cases}$$

The homogeneous constrain is rewritten as below:

$$\frac{r_0^2 + c_2^2}{2c_2} = \frac{a^2 + b^2}{2a}. \quad (3.59)$$

When  $F = 0 \rightarrow a = 0, b = 0$ , Eq. 3.58 and Eq. 3.59 become:

$$F = \frac{p\pi}{2} (r_0^2 + c^2) - \frac{3k\pi}{r_0} (c + a) \sqrt{r_0^2 + c^2} + 2k\pi (a + c), \quad (3.60)$$

$$\frac{r_0^2 + c^2}{2c} = \frac{a^2 + b^2}{2a}. \quad (3.61)$$

The root of the system of equations Eq. 3.60-3.61 is the geometrical parameter  $c_1$  of step 1. Then we have:

$$R_1 = \frac{r_0^2 + c_1^2}{2c_1}. \quad (3.62)$$

$$(3.63)$$

The root of the system of equations Eq. 3.53-3.59 is the geometrical parameter of step 2 that includes  $c_2, a, b$ , and the geometrical constraint is assumed as below:

$$R_2 = \frac{r_0^2 + c_2^2}{2c_2}. \quad (3.64)$$

The roots of the system of the equation are solved by the numerical method *vpasolve* of MATLAB.

### 3.1.2 Contact model with liquid film

In the previous section, we computed the specifications of a soft pad operating in its spherical dome states, which changed by the contact force  $F$  and the inner pressure  $p$ . In this context, we make the assumption that the dome initially makes contact with the surface through a surrounding liquid film, as depicted in Fig. 8. Liquid molecules adhere to the surface of the dome pad along the contact line between the dome pad and the surface of environment. Our aim is to formulate a model for the resistant force that arises at the contact interface due to this capillary action. This model serves to illustrate the role of the dome in improving locomotion. We calculate the tangential resistant force as follows:

$$F_{re} = F_{fr} + F_{ad} + F_{cap}, \quad (3.65)$$

where:

$$F_{fr} = \mu N, \quad (3.66)$$

$$F_{ad} = \tau A. \quad (3.67)$$

Let's examine the contribution of capillary action to the overall tangential resistant force. The different pressure between inside and outside of the liquid generates

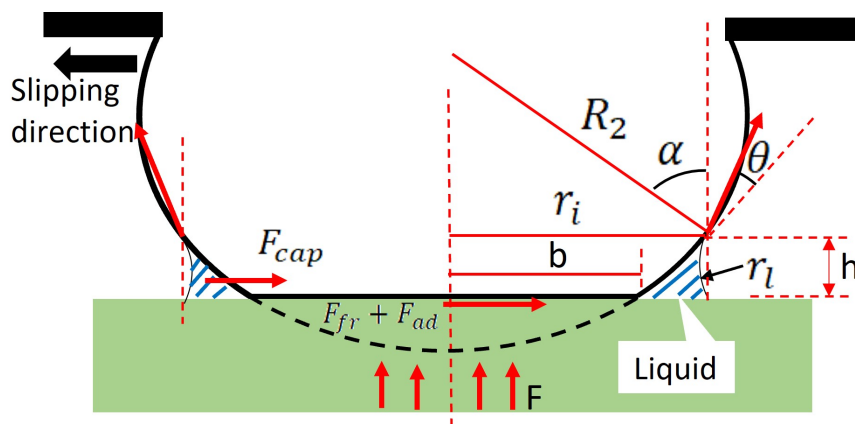


FIGURE 8: Capillary action occurs upon contact with the wet floor, induced by a liquid layer surrounding the soft pad with a height of  $h$ . In this situation, the pad exhibits a tendency to slip to the left.



resistance when the spherical pad attempts to move, which is referred to as the tangential capillary force. Consequently, the tangential capillary force can be calculated as follows:

$$F_{cap} = \int_S \Delta p_l dS \cos \phi, \quad (3.68)$$

$$= \Delta p_l h 2r_i. \quad (3.69)$$

Where  $\gamma_l$  is the surface tension of liquid, the different pressure between inside and outside liquid is estimated as:

$$\Delta p_l = \gamma_l \left( -\frac{1}{r_l} - \frac{1}{r_i} \right), \quad (3.70)$$

$$\text{and } h \approx 2r_l. \quad (3.71)$$

So, the different pressure between inside and outside liquid is rewritten as:

$$\Delta p_l = -\gamma_l \left( \frac{2}{h} + \frac{1}{r_i} \right), \quad (3.72)$$

$$F_{cap} = -2h\gamma_l \left( \frac{2}{h} + \frac{1}{r_i} \right) r_i. \quad (3.73)$$

Finally, the capillary force is summarized as:

$$F_{cap} = -2\gamma_l (2r_i + h). \quad (3.74)$$

The phenomenon of liquid rising along a solid surface due to wet adhesion is a fascinating interplay of intermolecular forces and gravity. This capillary rise, as it is known, occurs when a liquid is in contact with a solid substrate. At this interface, the liquid molecules experience adhesive forces that attract them to the solid. This adhesive force is often due to the surface tension of the liquid  $\gamma_l$ , which causes it to spread across the surface.

As the liquid molecules are attracted to the solid surface, they start climbing upwards. The height to which the liquid can climb is determined by the balance

between this adhesive force and the gravitational force acting on the liquid. When these forces are in equilibrium, the liquid ceases to rise further, and a stable meniscus or curved shape of the liquid is formed.

The shape of the meniscus is governed by the contact angle, which is the angle between the tangent to the liquid surface at the solid-liquid interface and the solid surface. A small contact angle corresponds to a high degree of wetting and results in a concave meniscus, while a large contact angle leads to a convex meniscus.

Applying Newton's laws to the system of force for wet adhesion and the weight of amount of wetted liquid, we obtain:

$$P_l = \sum F_{sl} \sin(\theta + \alpha), \quad (3.75)$$

$$\rho g V_l = 2\pi \gamma_s r_i \sin(\theta + \alpha). \quad (3.76)$$

In Fig. 8, the radius of the round boundary of the wetted area is determined as:

$$r_i = b + h \cot \alpha. \quad (3.77)$$

So, the Eq. 3.76 is rewritten as:

$$\begin{aligned} \rho g V_l &= 2\pi (b + h \cot \alpha) \gamma_s \sin(\theta + \alpha), \\ \text{so, } h\rho g \left[ \pi (b + h \cot \alpha)^2 - \frac{\pi}{3} \left( (b + h \cot \alpha)^2 + b^2 + (b + h \cot \alpha) b \right) \right] \\ &= 2\pi (b + h \cot \alpha) \gamma_s \sin(\theta + \alpha), \\ \text{then, } \frac{h\rho g}{3} \left[ 2(b + h \cot \alpha) - \frac{b}{(b + h \cot \alpha)} b - b \right] &= 2\gamma_s \sin(\theta + \alpha). \end{aligned}$$

Then, the related equation is rewritten as:

$$\frac{h\rho g}{3} \left[ b + 2h \cot \alpha - \frac{b}{(b + h \cot \alpha)} b \right] = 2\gamma_s \sin(\theta + \alpha). \quad (3.78)$$

$$\text{with } \frac{b}{(b + h \cot \alpha)} \approx 1. \quad (3.79)$$

Finally, the height of wetted liquid on the spherical pad is summarized as:

$$h = \sqrt{\frac{3\gamma_s \sin(\theta + \alpha)}{\rho g \cot \alpha}}. \quad (3.80)$$

Additionally, the contact angle is expressed through the surface tension of the liquid and solid as follows:

$$\cos \theta = \left( 2\sqrt{\frac{\gamma_s}{\gamma_l}} - 1 \right). \quad (3.81)$$

Insert these values into Eq. 3.68, resulting in the simplified estimation of  $F_{cap}$  as follows:

$$F_{cap} = -2\gamma_l \left[ 2b + (2 \cot \alpha + 1) \sqrt{\frac{3\gamma_s \sin(\theta + \alpha)}{\rho g \cot \alpha}} \right]. \quad (3.82)$$

As a result, we developed a model to elucidate the alteration in spherical pad morphology induced by air pressure. Subsequently, we demonstrated how this change provides an advantage in enhancing tangential force through computational analysis. The analytical model in this chapter is simulated by the Matlab code that attached in Appendix 7.2.1 and 7.2.2 (Chapter 7: Appendix).

### 3.1.3 Optimal function for design parameters

Building on the analytical model from the previous section, which formulated the geometrical shape of the dome and the wet-adhesive force, this section introduces an optimization function. This function helps us choose the optimal parameters for a foot equipped with dome pads. This purpose revolves around the initial radius, which we call  $r_0$ . It's not just an arbitrary number; it has a particular mission. We've set  $r_0$  with the aim of maximizing the number of contact pairs between the soft sphere pads and the ground surface. This strategy increases the area of contact and also makes the capillary phenomenon more effective.

In terms of optimizing the dome size on the foot, we start by assuming that the foot's area is constant, and it depends on the robot's size. We also suppose that the

maximum radius  $R$  of the dome, starting from the initial radius  $r_0$  of a thin sheet, should be about 1.5 times  $r_0$ .

This calculation gives us the surface area of the dome, which is represented by  $S_{dome}$ . Now,  $S_{dome}$  can be computed using this formula:

$$S_{dome} = 2\pi R \left( R + \sqrt{R^2 - r_0^2} \right) = \frac{3(3 + \sqrt{5})}{2} \pi r_0^2 = 7.8\pi r_0^2.$$

It's roughly 7.8 times the initial area, which means it elongates by around 180%.

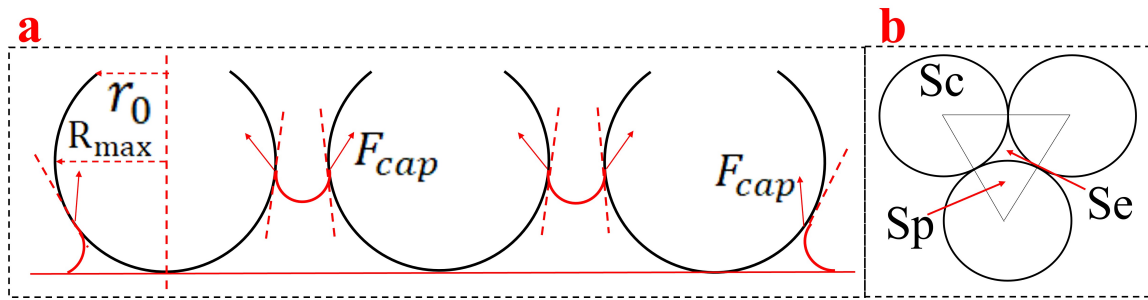


FIGURE 9: Optimization solution for design. (a) phenomenon of rising wet liquid. (b) the arrange of inflated dome in the foot and the area caculation.

This is significantly less than the 845% elongation threshold we observed with silicon Ecoflex 00-20. The number of domes on the foot, indicated as  $n$ , approximates the area  $S_e$ . Additionally,  $S_{tri}$  stands for the area of the triangle formed by three centers, which you can see in Fig. 9. This aspect is crucial to our design and functionality considerations.

As such, we calculate  $S_{area}$  as follows:

$$R = 1.5r_0, \quad (3.83)$$

$$S_{area} = n(S_c + S_e) = n(S_c + S_{tri} - 3S_p), \quad (3.84)$$

$$= n \left( \pi R^2 + 2R^2 \cos \frac{\pi}{3} - \frac{\pi R^2}{2} \right), \quad (3.85)$$

$$= \frac{9n}{4} \left( \pi r_0^2 + 2r_0^2 \cos \frac{\pi}{3} - \frac{\pi r_0^2}{2} \right). \quad (3.86)$$

The number of pads in a constant area is expressed as a function of the inertial radius:

$$n = \frac{S_{area}}{\left(\frac{\pi}{3} + \sqrt{3}\right) r_0^2}. \quad (3.87)$$

In this optimal calculation, we focus on the relationship between the initial radius  $r_0$  and various critical performance metrics, such as the robot's leg's maximum pressing force and the tangential capillary force. Referring to Eq. 3.60, the pressing force is determined as follows:

$$F = \frac{p\pi}{2} (r_0^2 + c^2) - \frac{3k\pi}{r_0} (c + a) \sqrt{r_0^2 + c^2} + 2k\pi (a + c),$$

$$c = R + \sqrt{R^2 - r_0^2} = \frac{\sqrt{5} + 3}{2} r_0.$$

In the case of an inflated dome with a sphere radius of  $1.5r_0$ , the inner pressure is calculated as:

$$F = 0, a = 0, \quad (3.88)$$

$$P = \frac{4.3K}{r_0}. \quad (3.89)$$

When the pressing force reaches its limit, the dome is re-pressed to the state of an approximately flat radius  $r_0$ , and the total pressing force on the foot is computed as:

$$F_{tot} = nS_{sh}P, \quad (3.90)$$

$$= \frac{S_{area}}{\left(\frac{\pi}{3} + \sqrt{3}\right) r_0^2} \pi r_0^2 \frac{4.3K}{r_0}, \quad (3.91)$$

$$= \frac{4.3\pi K S_{area}}{\left(\frac{\pi}{3} + \sqrt{3}\right) r_0}. \quad (3.92)$$

The calculated value of  $F_{tot}$ , derived from the equation presented above, is influenced by the radius  $r_0$ . A smaller  $r_0$  leads to a higher constraint on the pressing

force. Consequently, we have chosen  $r_0 = 0.5\text{mm}$  as it represents the smallest feasible size within our manufacturing capabilities, thereby optimizing the constraint on the pressing force.

According to the force balancing equation, the total capillary force is calculated as below:

$$\sum F_{cap} = P_{li}, \quad (3.93)$$

$$\text{so: } n\gamma \cos\theta S_d = D_l g (V_0 - nV_{sph}), \quad (3.94)$$

$$\text{then: } n\gamma \cos\theta 2\pi a = D_l g \left( S_{bou} h - \frac{n\pi h (3a^2 + h^2)}{6} \right). \quad (3.95)$$

So, the related equation is summarized as below:

$$\frac{2\gamma \cos\theta}{D_l g} a = \frac{\left(\frac{\pi}{3} + \sqrt{3}\right) S_{bou} r_0^2 h}{S_{area} \pi} - \frac{(3a^2 + h^2)}{6}. \quad (3.96)$$

Using the geometrical constraint of the dome parameters:

$$(R - h)^2 + a^2 = R^2, \quad (3.97)$$

$$\text{so: } a^2 = (2R - h) h, \quad (3.98)$$

$$= (3r_0 - h) h, \quad (3.99)$$

$$\text{then: } a = \sqrt{(3r_0 - h) h}. \quad (3.100)$$

The relation between the rising liquid height  $h$  and  $r_0$  is:

$$\frac{2\gamma \cos\theta}{D_l g} \sqrt{(3r_0 - h) h} = \frac{\left(\frac{\pi}{3} + \sqrt{3}\right) r_0^2 h}{\pi} - \frac{(9r_0 h - 2h^2)}{6}. \quad (3.101)$$

In investigating the complex interaction of important factors in our soft pad design, we used the computational tools of MATLAB, particularly the *fimplicit* function. The result of this estimation is shown in Fig. 10.

In our computation, we focus on the influence of several influential parameters including  $\gamma = 0.073\text{ N/m}$  (the surface tension),  $\theta = \pi/3\text{ rad}$  (the contact angle),

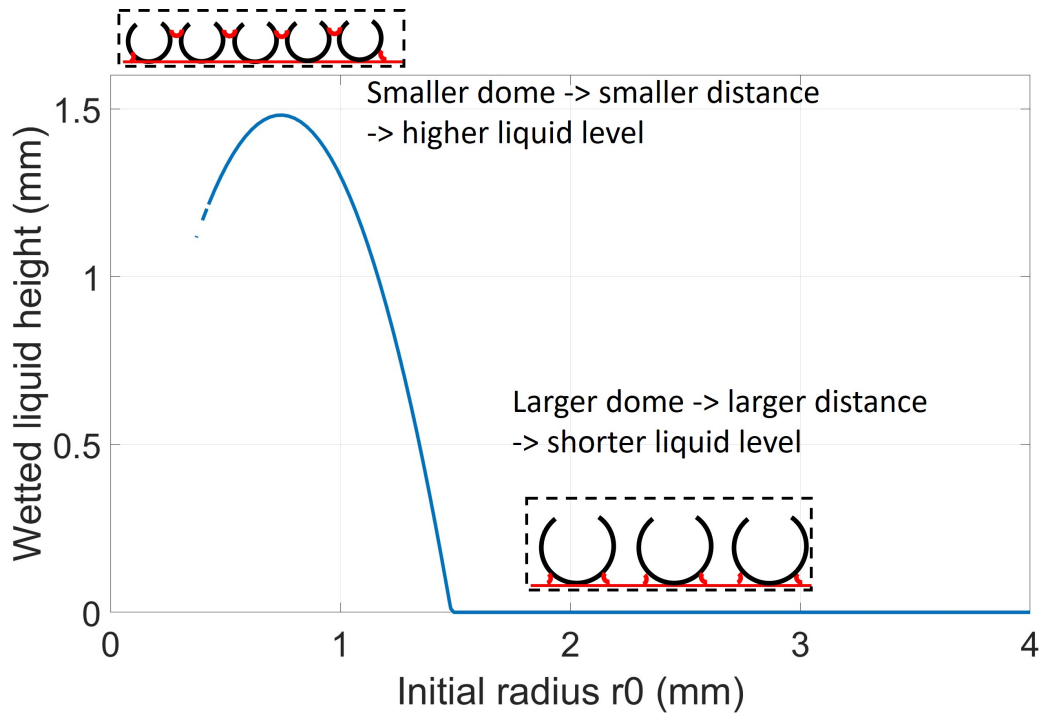


FIGURE 10: The graphical representation illustrates the changes in the liquid's rising height  $h$  versus the initial radius  $r_0$ .

$D_l = 1000 \text{ kg/m}^3$  (the density of liquid), and  $g = 9.81 \text{ N/m}^2$  (the acceleration due to gravity). This calculation helps us see the connection between two important things:  $h$ , the height of the liquid, and  $r_0$ , the initial size of our soft pad. The curve of  $h$  as it moved through changes in  $r_0$  showed a clear picture of the optimal range for this important factor. This result shows that the optimal range is between 0.3 and 0.8. Determining the exact optimal value of  $r_0$  is challenging. However, considering our manufacturing capabilities, the range of  $r_0$  around  $0.5 \text{ mm}$  aligns well with the optimal  $r_0$  range that maximizes the capillary force represented by the liquid height  $h$ .

## 3.2 Experimental

In this section, practical experiments were conducted to investigate calculations and ideas. The concept of the changeable dome pad is illustrated in Fig. 11. This dome pad can change its morphology by adjusting the inner pressure inside.

The soft pad is made of a silicone material called Dragon Skin 10, provided by Smooth-On, Inc., USA. Inside it, there's a rigid, red, 3D-printed structure called the

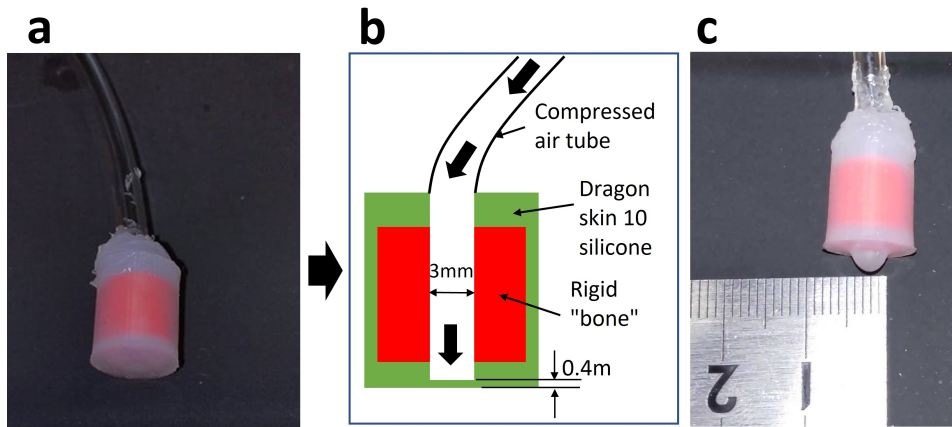


FIGURE 11: Design of the soft pad. (a) Soft pad without air pressure. (b) Illustration of the soft pad design concept. (c) Soft pad under the influence of air pressure.

rigid bone. This part is essential for changing the soft pad's shape.

A small chamber with a 3 mm diameter is designed as a pathway, guiding compressed air into the soft pad's container. By controlling the air, we make the soft pad inflate. Besides, the pad thickness is quite thin with 0.4 mm.

The main goal of choosing  $r_0$  was to optimize the contact area between the soft spherical pads and the ground. This helps increase the friction and adhesion, and it also makes the capillary effect more effective.

### 3.2.1 Inflation and contact-related shape verification

Fig. 12 describes the setup used in our experiments to investigate the analytical model. The experimental system comprises an IMADA force gauge attached to an acrylic plate, which is driven by a motorized linear stage. We also have a soft pad foot that can change its shape by adjusting the inner pressure with a pressure regulator, a pressure sensor to measure the inner pressure, and a 400-CAM058 microscope (SANWA SUPPLY) to measure the dimensions of the dome. In the dome shape experiment without applying pressing force, we adjust the inner pressure at different levels to measure the dome dimensions. Then, we conduct an experiment on the dome shape with pressing force. In this case, the IMADA force gauge is driven to move into the inflated dome. When the acrylic plate attached to the IMADA force gauge presses into the dome, the pressing force is displayed on the IMADA force gauge. Finally, we measure the dome shape parameters using the



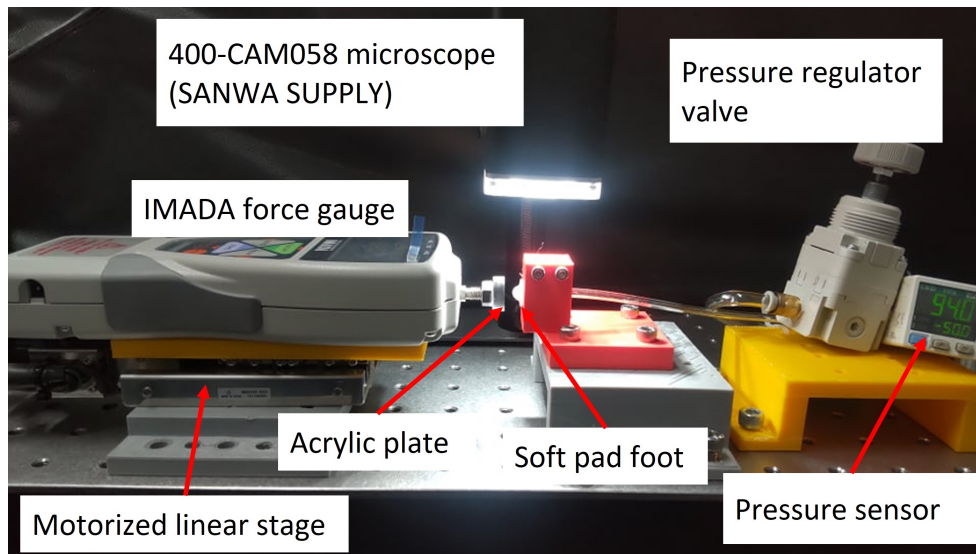


FIGURE 12: Experimental design for examining morphological changes.

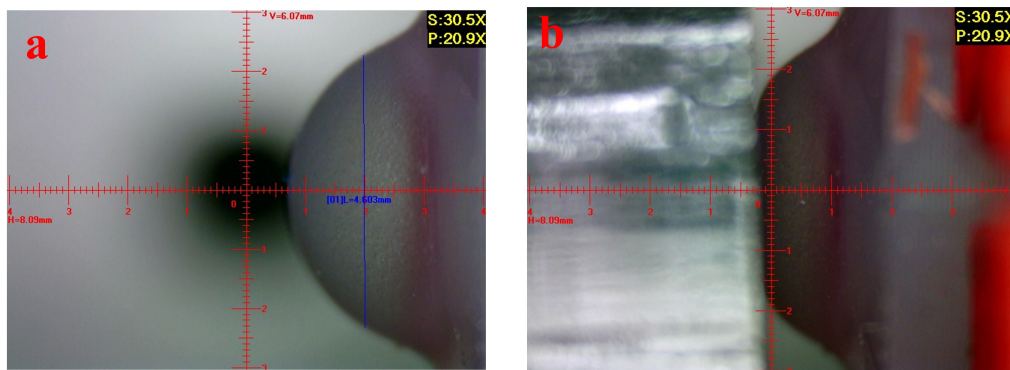


FIGURE 13: Dome morphology dimension processed by 400-CAM058 microscope (SANWA SUPPLY): a- without applying pressing force, b- with applying pressing force.

400-CAM058 microscope (SANWA SUPPLY). Fig. 13 shows the processed image by using 400-CAM058 microscope for dimension measuring in 2 case: with applying pressing force and without applying pressing force. The 400-CAM058 microscope is used with UM12-CAM software for displaying the scaled dome on the software interface.

In the dome shape experiments without applying pressing force, we manipulated the air pressure, setting it to various levels: 55 kPa, 65 kPa, 75 kPa, and 85 kPa. Upon completing these experiments, we plotted the results and compared them with calculated values based on the methodology outlined in the previous section (see Fig. 14, 15). The observed errors typically fell within a range of approximately  $\pm 3\%$ . Remarkably, our analysis indicated that the magnitude of errors exhibited

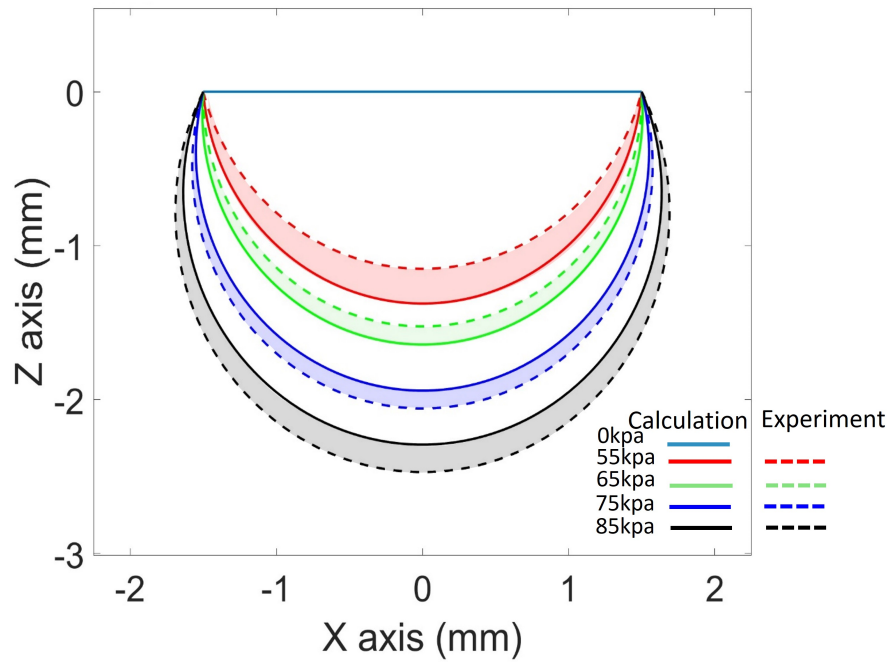


FIGURE 14: Experiment state 1: Effects of different pressures in the soft pad without floor contact were compared using Matlab (Code matlab in Appendix 7.2.1).

a rising trend in tandem with increased air pressure. This correlation could be attributed to changes in the elasticity coefficient  $k$ , which tended to increase as deformation intensified. To assess the pad's elastic properties, we conducted tests using an MX2 Motorized test stand. In practice, it's worth acknowledging that the elasticity coefficient can fluctuate depending on the Young's modulus, particularly in scenarios involving significant deformation. However, in this specific study, we assumed that the deformation of the soft pad dome occurred within the linear region of the Young's modulus, leading to a constant elasticity coefficient.

Transitioning to the experiment of dome shape with applying pressing force, we maintained a constant air pressure of 75 kPa. Then, we considered varying levels of compressive force, setting them at 0.1 N, 0.2 N, and 0.3 N, respectively. In this, we collected parameters including  $b$ ,  $r_0$ , and  $d = (c_2 - a)$ , as illustrated in Fig. 6d. The radius and height of the dome were subsequently calculated using the following

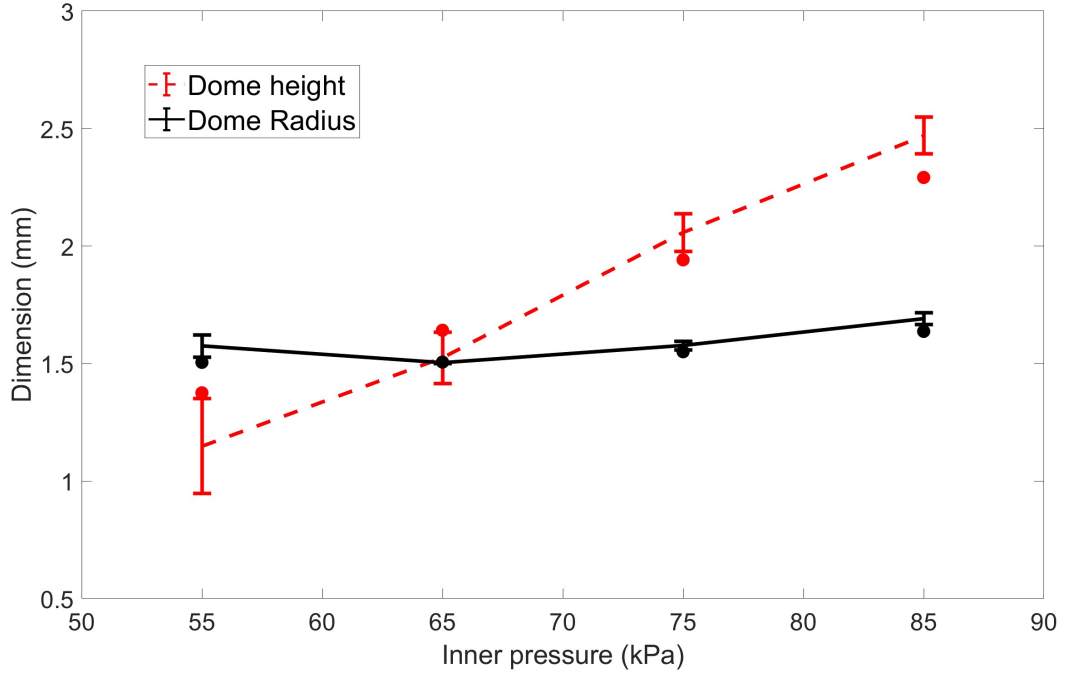


FIGURE 15: Experiment state 1: dimension of dome height and dome radius.

formulate:

$$c_2 = \frac{\sqrt{(r_0^2 - b^2 - d^2)^2 + 4r_0^2d^2} - (r_0^2 - b^2 - d^2)}{2d},$$

$$R_2 = \frac{(r_0^2 + c_2^2)}{2c_2}.$$

Additionally, based on Popov's research (2010) [39], the relative surface energy between the silicone material and acrylic, defined as  $\gamma_{12} = 2\sqrt{\gamma_1\gamma_2}$ , was found to be approximately  $0.006 \text{ J/m}^2$ .

Fig. 16, 17, and 18 present the experimental and calculated results. Fig. 16 compares the dome's geometrical shape under various pressing forces. Fig. 17 and 18 present the dimensions of dome height, radius, adhesive radius, and depth, including error bars.

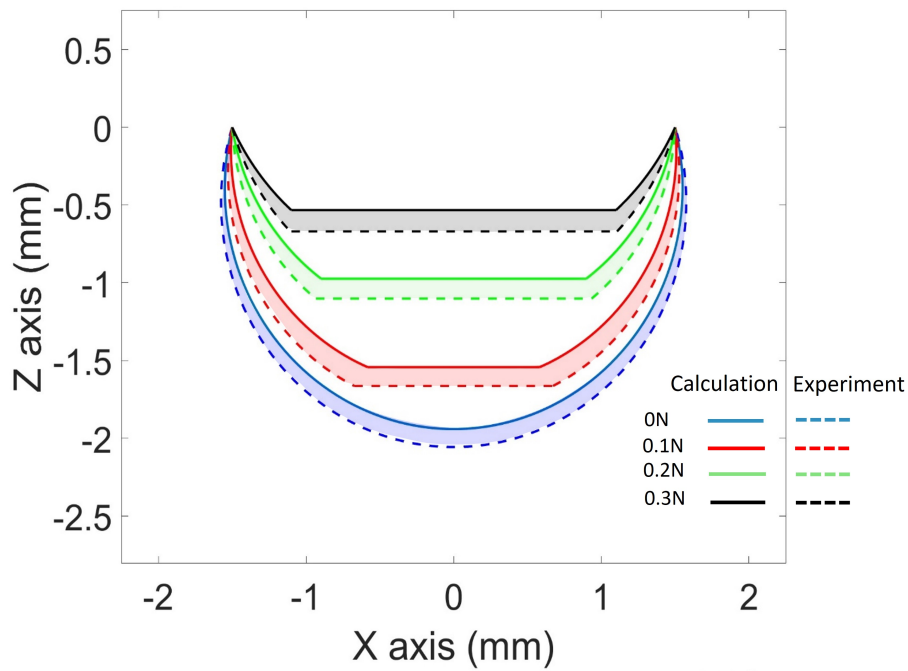


FIGURE 16: Experiment state 2: Response of the soft pad under air pressure of 75 kPa to being pressed at different forces (Code matlab in Appendix 7.2.2).

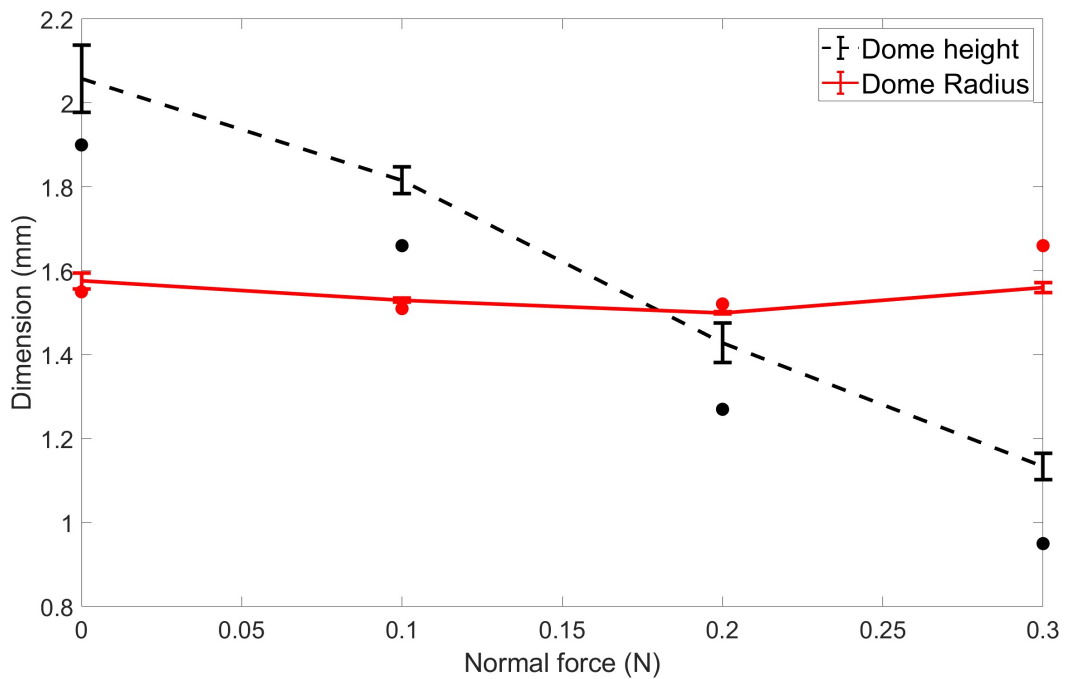


FIGURE 17: Experiment state 2: dimension of dome heigh and dome radius.

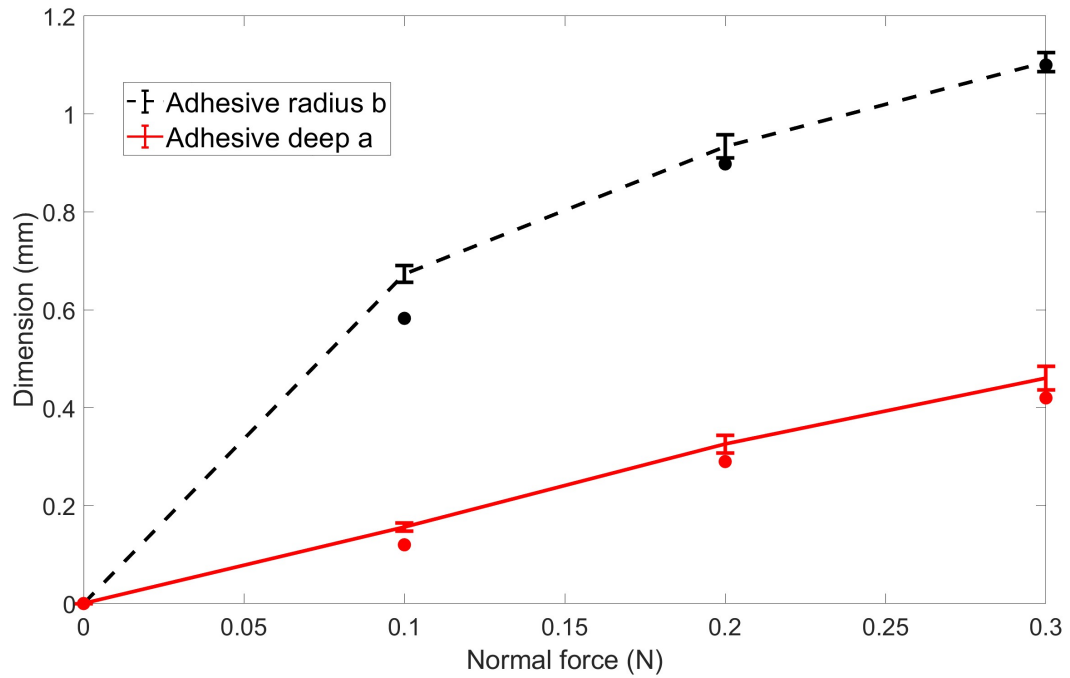


FIGURE 18: Experiment state 2: dimension of adhesive radius and adhesive deep.

### 3.2.2 Tangential force experiment

In this section, we investigate the influence of capillary action on the soft pad dome's resistance to slippage. The experimental setup, illustrated in Fig. 19a, incorporates two motorized linear stages responsible for vertical and horizontal movements. Our experiments encompassed both wet and dry conditions, with the soft

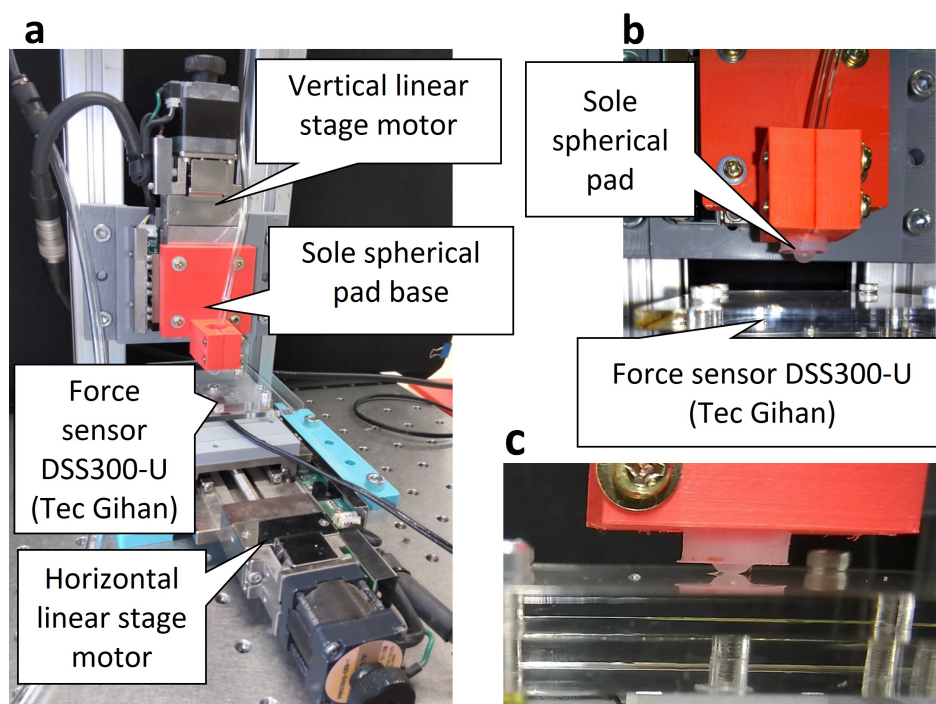


FIGURE 19: Experiment to assess the resistance of the soft pad to tangential forces: (a) Setup of the experiment. (b) Soft pad under air pressure without simulated floor contact, (c) and with simulated wet floor contact.

pad's morphology ranging from flat to domed at 65 kPa, 75 kPa, and 85 kPa, respectively. We calculated the resultant capillary force  $F_{cap}$  as the difference between  $F_{wet}$  and  $F_{dry}$ , the tangential forces measured under wet and dry conditions. In other words,  $F_{cap} = F_{wet} - F_{dry}$ . These tangential force measurements were recorded *prior* to the onset of complete slippage, known as incipient slip (see [53]). Each experimental trial began by pressing the soft pad against a surface, securely affixed to a 3-axis force sensor (DSS300-U, TecGihan, Japan), with varying contact force values. Subsequently, the horizontal linear stage was set in motion, providing tangential

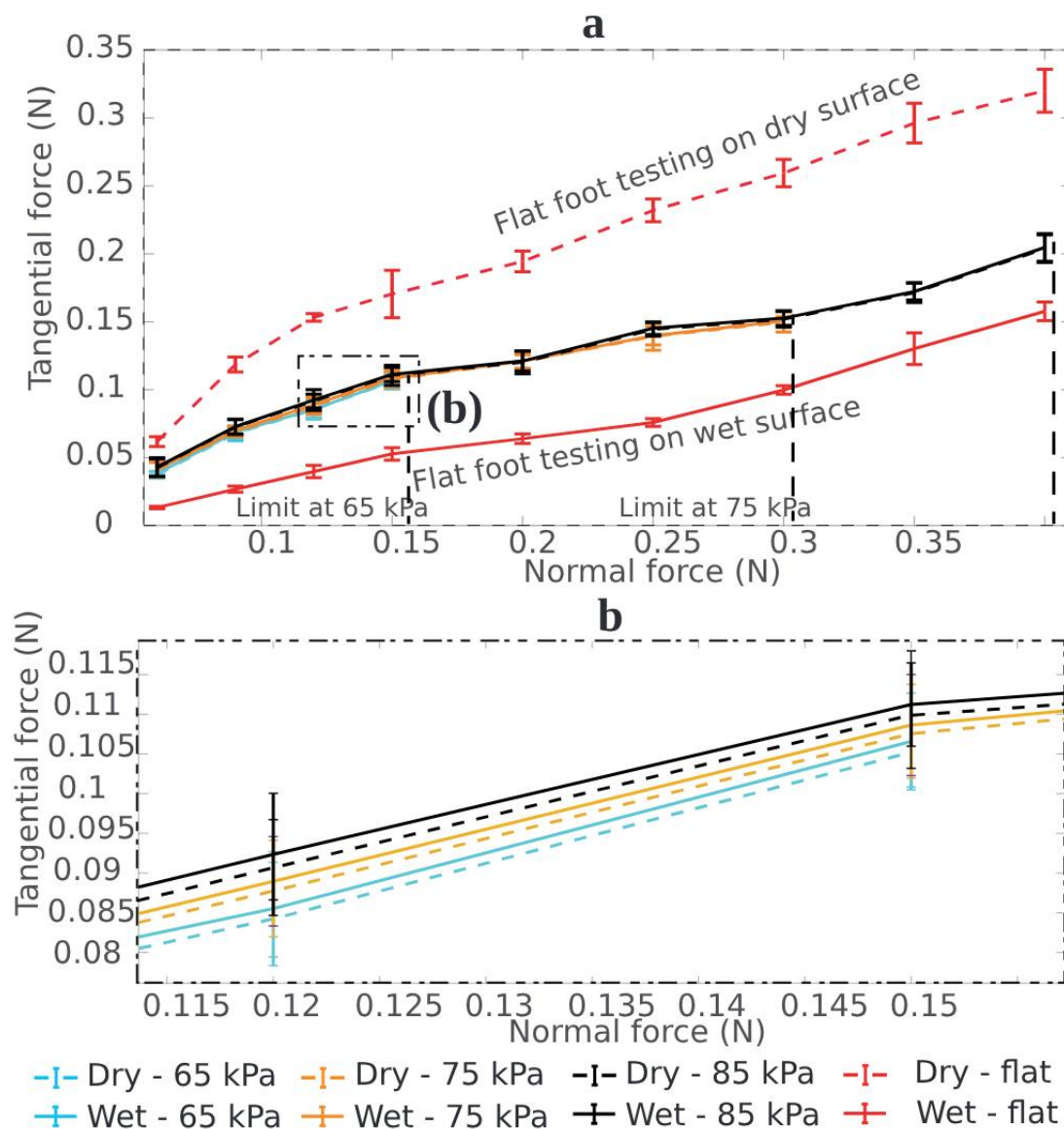


FIGURE 20: (a) Comparison of resulted tangential forces among flat soft pad, and domed pad under pressures of 65 kPa, 75 kPa, and 85 kPa, respectively; on both wet and dry floors. (b) Zoom-in range with comparison of tangential forces under dry (dashed line) and wet (solid line) conditions several air pressure values.



displacement to the soft pad at a low speed of 0.2 mm/s to minimize viscosity effects. The outcomes of these experiments are summarized in Fig. 20.

When considering the dry condition, a flat soft pad (i.e., without the spherical dome induced air pressure) displayed the highest tangential forces across a range of normal forces (up to 0.4 N). However, under wet conditions, the resulting tangential force on the flat-surfaced soft pad decreased significantly. This result emphasizes that a flat soft pad morphology is only suitable for dry environments, as it may experience reduced tangential forces, leading to potential slippage on wet surfaces. In the case of the domed soft pad morphology, we ensured that slippage did not occur by employing a slow pad movement speed of 0.2 mm/s. Additionally, the air

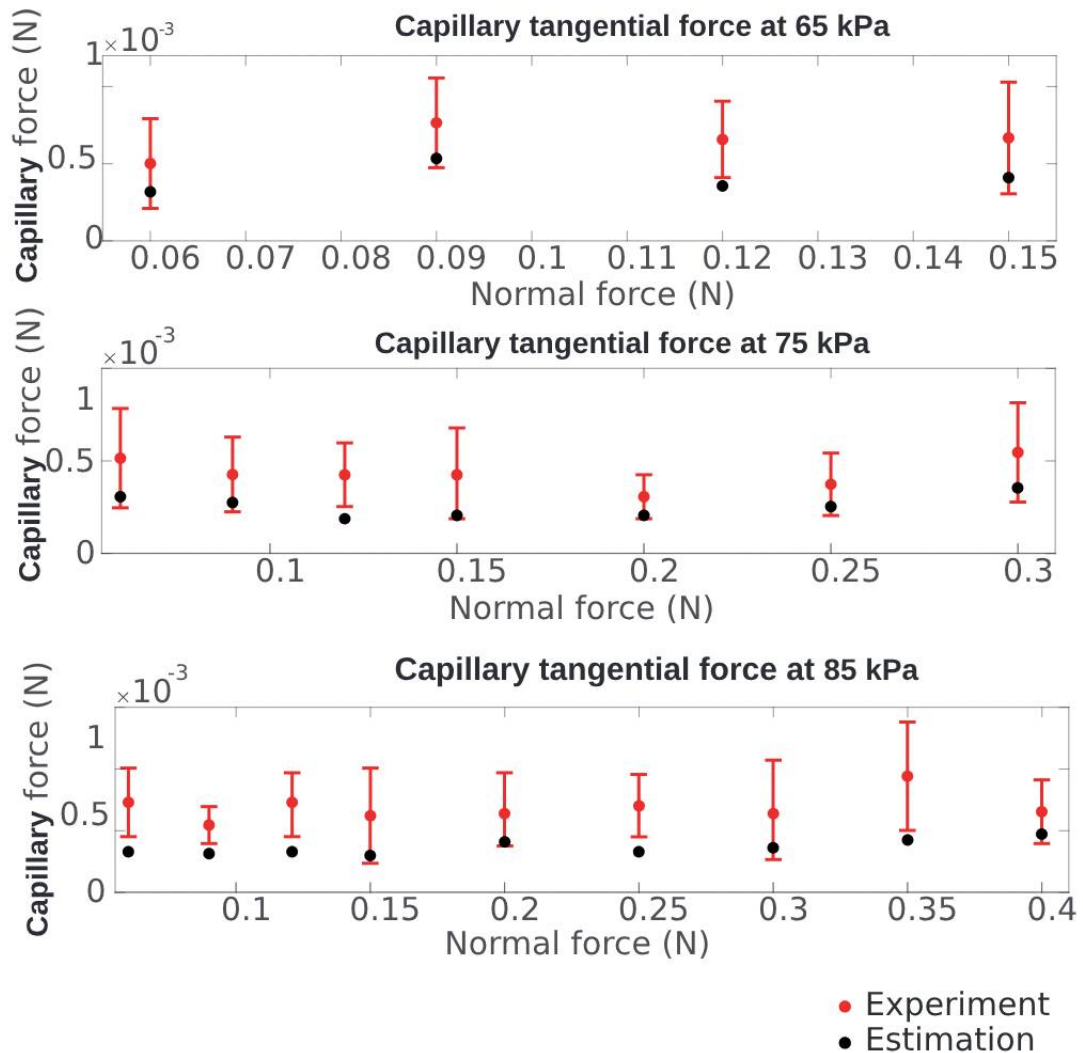


FIGURE 21: Comparison of capillary action in wet condition ( $F_{cap} = F_{wet} - F_{dry}$ ) between experiment (with error bars) and estimation results.

pressure was adjusted to assess the morphological effect. Fig. 20a-b indicate minimal differences in tangential force values between the two conditions: wet (solid lines) and dry (dashed lines). Most notably, the tangential force associated with the domed soft pad surpassed that of the flat pad in wet conditions, indicating superior walking stability with a domed soft pad. Therefore, we conclude that a *flat soft pad is suitable for walking on dry surfaces, and a domed pad is preferable for walking on wet surfaces.*

Concerning the domed soft pad, we assessed the effect of its morphology (determined by inner pressure) on the resulting tangential force. The dome cannot endure high normal force when pressed against the contact surface, as this force could exceed the potential energy stored in the inner pressure. As such, there exists a normal force limit for each morphological state of the dome. According to our measurements, the limits for normal force at 65 kPa, 75 kPa, and 85 kPa are 0.15 N, 0.3 N, and 0.4 N, respectively (as shown on the horizontal axis of Fig. 9a). Our proposed analytical model (refer to Eqs. (17)-(19)) reveals that a lower normal force results in a reduction of the tangential force during the contact phase. Therefore, increasing the air pressure to modify the morphology is essential for raising the normal force limit and, subsequently, enhancing the tangential force. Moreover, substituting the silicone material, such as switching from Dragon Skin 10 (Shore Hardness 10A) to Dragon Skin 20 (Shore Hardness 20A) or Dragon Skin 30 (Shore Hardness 30A), can elevate the normal force limit.

In Fig. 21, we compare the resultant capillary force  $F_{cap}$  of a domed pad in wet conditions across three different air pressure levels (65 kPa, 75 kPa, and 85 kPa) with the estimated values from our analytical model (see Eq. (28)). Despite the complexity introduced by the liquid film at the contact area, leading to errors ranging from 10% to 26%, the experimental results align with the predicted trend.

In this chapter, the design and fabrication process have been explained, and the physical significance will be clarified through the energy equation. The results obtained from calculations and simulations will be validated through experiments. In the next chapter, the mathematical model based on Finite Element method that plays



an important role in this research will be explained.

# 4 The finite element analysis (FEA) for representing wet

## 4.1 The FEA-based solution

In the previous chapter, we presented an analytical model to explain the interplay between solid and liquid in wet adhesion phenomena. Nonetheless, this analytical model has constraints when dealing with specific geometrical shapes and is incapable of addressing issues related to general shapes that are non-integrable. This section introduces a novel Finite Element Method (FEM)-based solution to handle scenarios involving general geometrical shapes. The strategy proposed in this section aims to serve as a comprehensive solution for understanding wet adhesion phenomena in cases of solid objects with arbitrary geometrical shapes.

Several studies have employed the FE method to compute geometric parameters in wet adhesion phenomena, such as [54], [55]. Additionally, researchers have published studies utilizing the FE method to describe capillary phenomena [56]. Furthermore, the authors in research [54] provided estimations for calculating capillary forces in the vertical direction using the FE method. Compared to the mentioned studies, our FE method model in this study contributes the following novelties: firstly, our model considers deformation in soft contact, thus accounting for wet adhesion interaction based on deformed objects; besides, the results we investigate using the FE method in this study is focussed on the tangential effects of wet adhesion force and capillary force, factors used to assess the sliding mechanism in robot locomotion; finally, the FE method model used in our study is applied to calculate in the case of multiple dome pads, which has not been addressed in other studies.

### 4.1.1 The general problem of capillary phenomenon

The conceptual design and mathematical model for the foot with soft pads are presented in Fig. 2. In previous chapter, we proposed a method for modeling the capillary force, which relies on the shape of the dome pad, subject to alterations due to compressed air pressure and applied force. However, this approach has certain limitations; it mainly applies to specific pad geometries that are integrable. When in motion, these pads can undergo deformations as they interact with the environment. Consequently, when we consider the general geometry of the pad, the curved surface of the liquid becomes quite complex, leading to certain unidentified parameters affecting the capillary force.

Furthermore, the influence of the distribution of these dome pads on the capillary force remains unclear, especially in cases where the liquid rises between these pads. In this study, we introduce a novel approach that using the Finite Element (FE) method. This approach is founded on the equilibrium energy equation of the liquid. This approach's advantage is that it allows us to explore wet adhesion and capillary forces, not just at the individual pad level but also within the context of the distributed pattern of pads on the foot. By doing so, we aim to gain a more comprehensive understanding of how these forces operate and interact, enhancing our knowledge of the interplay between the soft pads and the environment. This could be a significant step toward improving the design of these pads and enhancing their performance in practical applications.

### 4.1.2 The FEA-based model for the capillary phenomenon

The phenomenon of capillary rise has attracted the attention of researchers in the history of modern science [57]. The energy balance governing the slow rise of liquid in a capillary tube is composed of three terms: the work done in lifting the liquid ( $W$ ), a term accounting for viscous dissipation ( $K$ ) in the flowing liquid, and a potential energy term ( $-\Delta U$ ) representing the energy stored in the liquid column

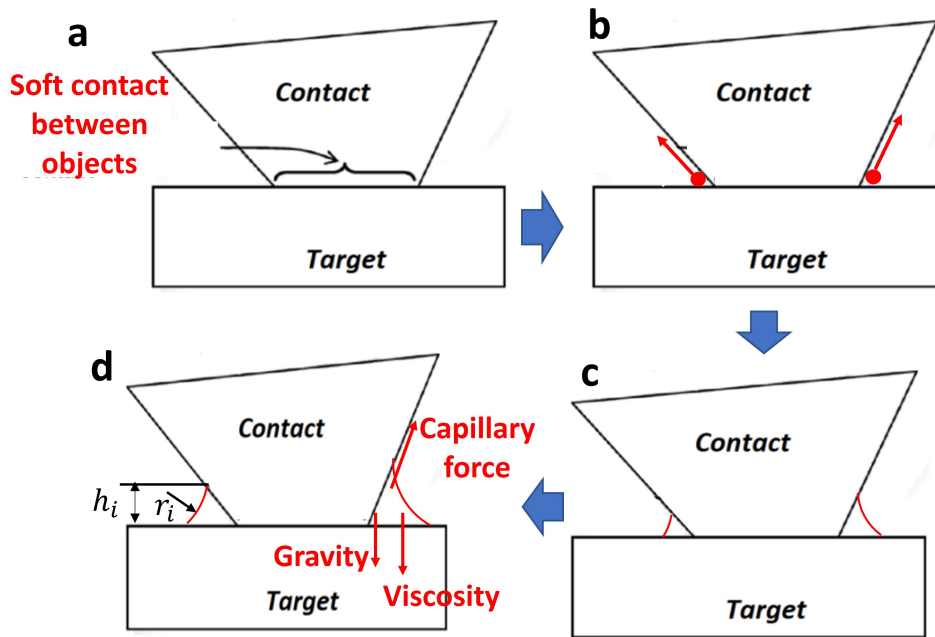


FIGURE 22: Wet process: (a) Soft contact between 2 object. (b) Liquid molecular of wet-adhesion phenomenon in the first time. (c)Wet-adhesion phenomenon in process . (d) Equilibrium state.

[58], [59]:

$$W - K = -\Delta U, \quad (4.1)$$

This dynamic interplay of these components underlies the capillary rise phenomenon, where the balance between lifting the liquid, energy dissipation, and the stored potential energy in the liquid column ultimately determines the height to which the liquid will ascend within a capillary tube. Understanding this balance is crucial in the fields, from microfluidics to materials science, offering insights into the capillary forces that shape the behavior of liquids in confined spaces.

We present Fig. 22, which illustrates the process of liquid rising onto the object from the perspective of energy balance. Fig. 22a illustrates the interaction between the soft object and the surface. Following this interaction, the liquid atoms undergo upliftment, primarily propelled by the action of the wet adhesion force. The work of this force is distributed between two significant factors: the potential energy stored within the liquid and the intermolecular interactions occurring among the liquid

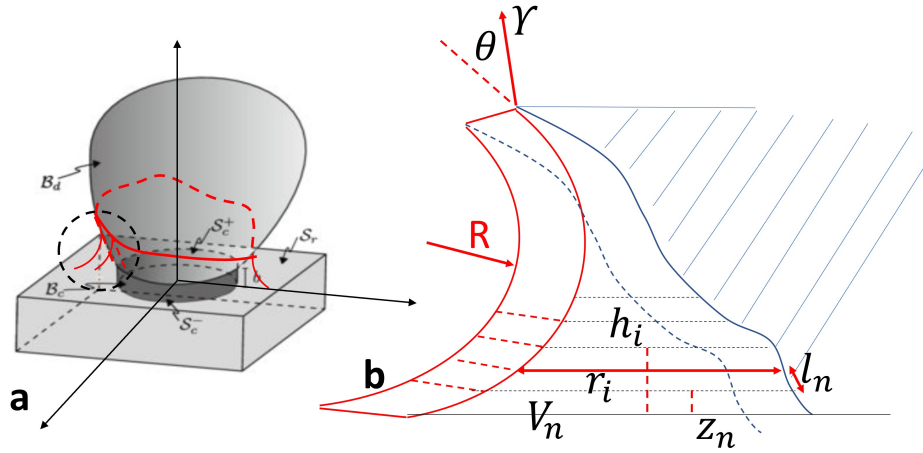


FIGURE 23: (a) Wet adhesion phenomenon in general geometry object. (b) Differentials of liquid following polar coordinates.

atoms, a phenomenon often referred to as viscous dissipation. These fundamental mechanisms are pivotal in comprehending the process of capillary rise and are instrumental in revealing the intricacies of liquid wetting on soft objects. This understanding carries implications in various fields where liquid-surface interactions come into play, from engineering to materials science.

We call the  $W_e$ ,  $K_e$ ,  $U_e$  are the differentiation element following polar coordinates of work of capillary, viscous dissipation, and potential energy, respectively.

$$W = \int_S W_e ds, K = \int_S K_e ds, \Delta U = \int_S U_e ds. \quad (4.2)$$

In this approach, we consider the balance of energy in each element following polar coordinates Fig. 23:

$$W_e - K_e = -\Delta U_e. \quad (4.3)$$

In the role of capillary forces governing the elevation of liquid on a surface, we can delve into the components that construct this phenomenon. Here, the capillary force in each element is denoted as  $f_c$ , while  $dl$  stands for the length of the differential curve. The number of differential layers is represented by  $n$ , and  $l_n$  is the path of the object layer. The crucial parameter of liquid's surface tension energy is called  $\gamma$ . Additionally,  $\phi_1$  characterizes the angle formed between the capillary force and the

curve of the object layer. These variables and their interactions within the context of capillary forces define the dynamics of liquid rise and play a significant role in understanding wetting phenomena on various surfaces. In this context, the equation is formulated as follows:

$$W_e = \int_{L_e} f_c dl \quad (4.4)$$

$$= \sum_{i=0}^n l_n \gamma \cos \phi_1. \quad (4.5)$$

In the case of capillary rise on a wet object, the expression for viscous dissipation can be formulated as follows. Here,  $V_e = V_n(h_i; r_i)$  represents the volume of each liquid layer,  $dp_h$  denotes the hydro-static pressure at each liquid layer,  $\rho$  stands for the liquid's density,  $g$  symbolizes the acceleration due to gravity, and  $z_n$  signifies the height of the liquid layer:

$$K_e = \int V_e dp_h \quad (4.6)$$

$$= \sum_{i=0}^n \rho g z_n V_n(h_i; r_i). \quad (4.7)$$

The change in the gravitational potential energy ( $-\Delta U$ ) can be calculated by integrating the hydro-static force ( $\mathbf{f}_h$ ) as liquid rises from  $z = 0$  to  $z = h$ :

$$\Delta U_e = \int_0^h P_z dz \quad (4.8)$$

$$= \int \rho g V_n(h_i; r_i) dz \quad (4.9)$$

$$= \sum_{i=0}^n \rho g z_n V_n(h_i; r_i). \quad (4.10)$$

Then, the Eq.4.3 become:

$$\sum_{i=0}^n l_n \gamma \cos \theta - \sum_{i=0}^n \rho g z_n V_n(h_i; r_i) - \sum_{i=0}^n l_n \rho g z_n V_n(h_i; r_i) = 0. \quad (4.11)$$

## 4.2 Implementation using SOFA (Simulation Open Framework Architecture) framework

SOFA (Simulation Open Framework Architecture) is a open-source framework designed for the simulation of interactive, real-time physical phenomena. Developed by a community of researchers and engineers, SOFA has become a promising platform for simulating complex, dynamic, and real-world scenarios across various domains, including robotics, biomechanics, medical simulation, and computer graphics. One of SOFA's distinctive features is its adaptability, allowing users to create highly detailed, customized simulations. This flexibility is achieved through a component-based architecture, where each element in the simulation is represented as an individual module. These components can be easily integrated or replaced, enabling researchers and developers to manage simulations to their specific needs. SOFA's open-source encourages collaboration, innovation, and community-driven development. It provides a large library of pre-built components, models, and solvers, reducing development time and enabling users to focus on the core aspects of their simulations. SOFA integrates with other established tools, making it flexible and powerful. This allows users from diverse fields, like biomechanics, robotics, and medical training, to create real-time, interactive simulations. SOFA's powerful framework helps build realistic simulations that run in real-time, pushing the boundaries of virtual reality and computer modeling. Here, the SOFA framework is used to apply the model based on finite element method for capillary simulation.

### 4.2.1 The wet adhesion phenomenon simulation for various shape objects using SOFA

To find the parameters of curved surface of liquid and capillary force, we use an iterative loop, in which the function energy  $Q_e$  is shown as below:

$$Q_{layer} = W_{layer} - K_{layer} + \Delta U_{layer}. \quad (4.12)$$

Base on the equilibrium energy concept in Eq. 4.12, achieving an equilibrium state  $Q_e = 0$ . To proceed, we divide the liquid element into layers, aligning them with the object's mesh. The layer that meets the equilibrium energy condition  $Q_e = 0$  is denoted as the "wet layer." Consequently, layers positioned below the wet layer exhibit a positive energy function ( $Q_e > 0$ ), while those situated above the wet layer manifest a negative energy function ( $Q_e < 0$ ). In our finite element method-based approach, we employ an iterative process to systematically assess each wet layer, commencing from the lowest layer (i.e., the interaction layer between the object and the surface). The iteration concluded once the condition  $Q_e > 0$  is no longer met, determining the appropriate wet layer.

In each iteration cycle, the energy function  $Q_e$  is determined by the parameters of the liquid surface formed during the wetting phenomenon on the object's surface, as illustrated in Fig. 24. Considering a layer assumed to be the rising liquid level, the angle  $\theta$  represents the angle of the surface deformation formed with the vertical axis  $z$ . The  $\phi_1$  angle, obtained from the geometric shape of the pad give us the tangential direction angle of pad surface at differentiation. So, The  $\phi_2$  angle is the angle of the curvature of liquid considered from center. The points  $A_1, A_2, \dots, A_n$  are the respective mesh points on the object's surface.  $C_1, C_2, \dots, C_n$  are the corresponding points belonging to each layer situated on the curved surface of the wetting liquid element in the polar coordinate system of the wetting liquid on the object. Due to the uniformity and symmetry of the liquid molecules, we can construct a circular curve passing through  $C_1, C_2, \dots, C_n$ . The differential angle  $\Delta\phi$  with respect to the center, as viewed from each arc  $C_1C_2, C_2C_3, \dots, C_{n-1}C_n$ , is calculated as  $\Delta\phi = \frac{\phi_2}{\text{amount of layers}}$  (see Fig. 24b). Besides,  $\alpha$  is the angle of considered slice of liquid in polar coordinate. So, in the iteration cycle of considering each slice of liquid, we need to use the  $\alpha_j$  for each cycle.

$$a_i = z_i \tan(\theta - i\Delta\phi), \text{ with } i = 0 : n \quad (4.13)$$



By using the data from the mesh of the object, we determine the vector  $\overrightarrow{A_i A_{i+1}}$  and the angle  $\alpha_j$ . Then, the points of curved surface are determined as below:

$$\overrightarrow{C_i C_{i+1}} = (a_i \cos \alpha_j; a_i \sin \alpha_j; z_i), \tag{4.14}$$

$$C_{i+1} = (x_{c_i} + a_i \cos \alpha_j; y_{c_i} + a_i \sin \alpha_j; z_{c_i}). \tag{4.15}$$

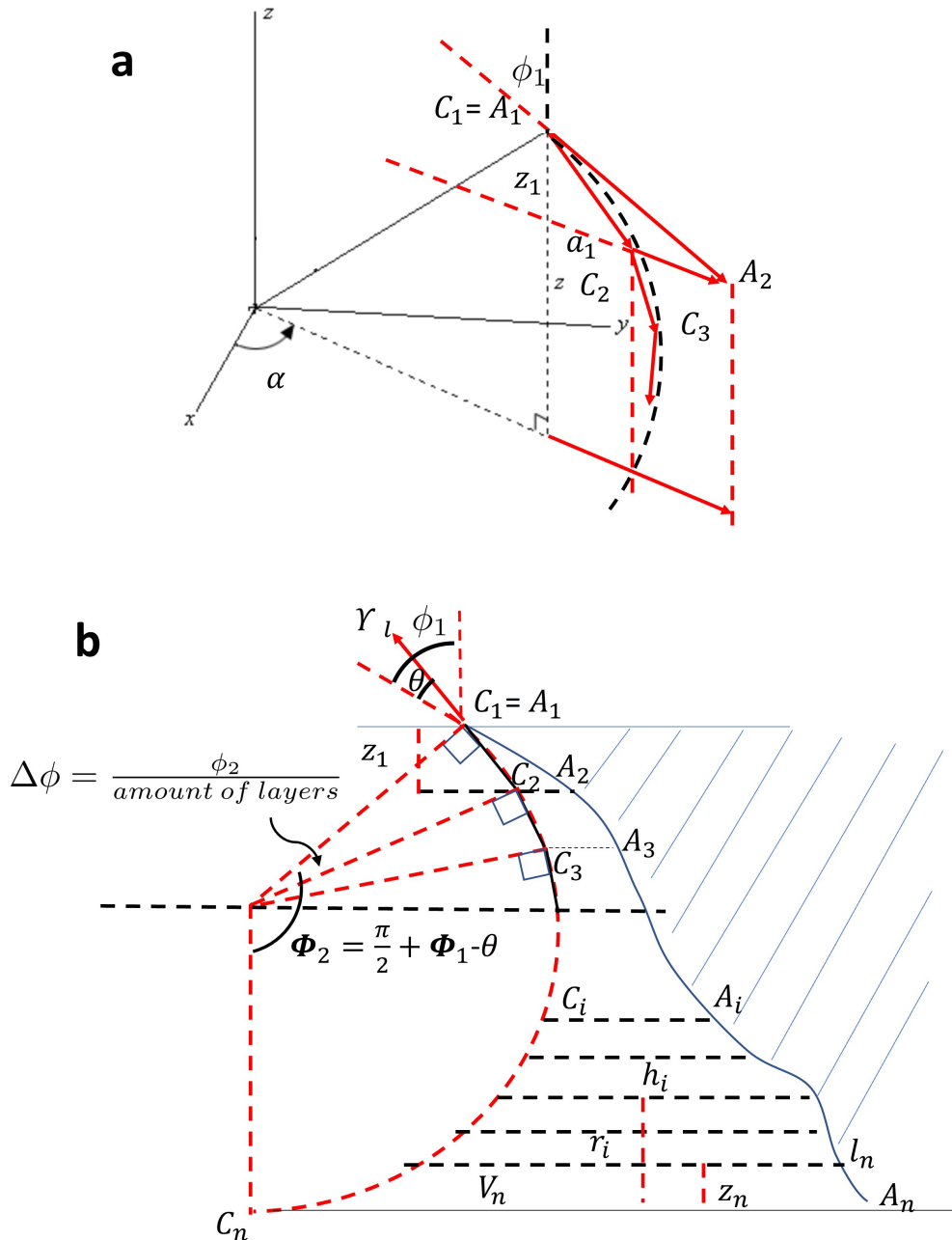


FIGURE 24: (a) The geometric parameters of the differential element of the liquid mass in polar coordinate system. (b) The 2D projection of the differential element of the liquid mass onto its own normal plane.

The radius of curvature is determined through the angle  $\phi_2$  and the length of the curve:

$$\phi_2 R = \sum_{i=0}^n C_i C_{i+1} = C_1 C_2 + C_2 C_3 + C_3 C_4 + \dots + C_{n-1} C_n. \quad (4.16)$$

Then, the pressure difference between the outside and inside of liquid is calculated:

$$\Delta p = \gamma_l \left( \frac{1}{R} + \frac{1}{r} \right). \quad (4.17)$$

The capillary force in this case is calculated as follows: (where  $S_{section}$  is the projected area of the wetting liquid on a plane perpendicular to the direction of motion, see the Fig. 27):

$$F_{cap} = \Delta p S_{section}. \quad (4.18)$$

The algorithm comprises three main stages: Processing index data, considering each slice of the surface, and calculating the wet adhesion, executed in sequence. The processing index data stage begins with the creation of a mesh structure for contact. The user inputs the elements into SOFA and gets parameters for these elements. The contact layer is identified, and the surface is divided into smaller slices, with their indices arranged from low to high. Next, the considering each slice of the surface is processed. A loop runs through each layer from 1 to the maximum layer. Within each layer, coefficients such as  $C_2, C_3, C_4, C_5$  are determined. The algorithm calculates  $Q_e$ , and based on its sign, the process either returns to the first step or proceeds. Once the loop is broken, the wetted layer is determined.

Finally, the calculating the wet adhesion stage is entered. It starts by calculating the wetted liquid area, followed by the computation of  $\Delta p$ , which is important for the subsequent steps. The algorithm then calculates the section of liquid volume in a defined direction and uses this information to calculate the wet adhesion. In this study, there is another crucial step that we have not fully addressed, which is to investigate the influence of the calculated capillary force on the mesh of the object. The

ultimate result to be examined is the equilibrium state of the object's deformation and the updated capillary force based on that deformation. For objects with high stiffness, the capillary force is too small to cause significant deformation. However, a comprehensive model based on the finite element method requires addressing this issue. In this case, a solution has been prepared for future work. We expect to use  $\Delta p$  as a parameter representing the force acting on each element of the mesh object, combined with the normal angle parameter of the element. This information will then be used to calculate the force vector acting on each element. Subsequently, this force parameter will be used to calculate the deformation of the mesh object. We anticipate that this complete algorithm will propose a comprehensive solution in the future.

This algorithm's approach ensures a detailed and accurate analysis of wet adhesion for a given surface and liquid interaction. The algorithm of our finite element method that use to estimate the capillary force is shown as the Fig. 25.

Based on the algorithm explained in this section, we have developed a Python code in SOFA to simulate the curved surface of wet liquid for various geometrical shapes. Fig. 26 displays the results obtained through our novel approach, and these results align well with the observed physical phenomena and related research [60]. Notably, Fig. 26c presents the simulation of wet liquid for a general shape. Utilizing the energy balance equation, we determined the wet layer at each differential element across the entire surface of the object. Subsequently, the geometrical deformation of the wet liquid was illustrated as shown in Fig. 26. Then, Fig. 27 illustrate the method to calculate capillary following the direction of movement. (Eq. 4.18).

Next, we provide results calculated in the SOFA environment using the FE method model. As we know, the geometric parameters of the liquid include two factors: the height of the liquid rising above the solid surface and the radius of the liquid surface. These factors are related to the geometry of the solid, the tension energy of the liquid, and the contact angle of wet adhesion forces which depending on the tension energy of the liquid and solid according to formula  $\cos\theta = 2\sqrt{\frac{\gamma_s}{\gamma_l}} - 1$  [14]. According to the formula, we will see that under wet adhesion conditions, cos theta

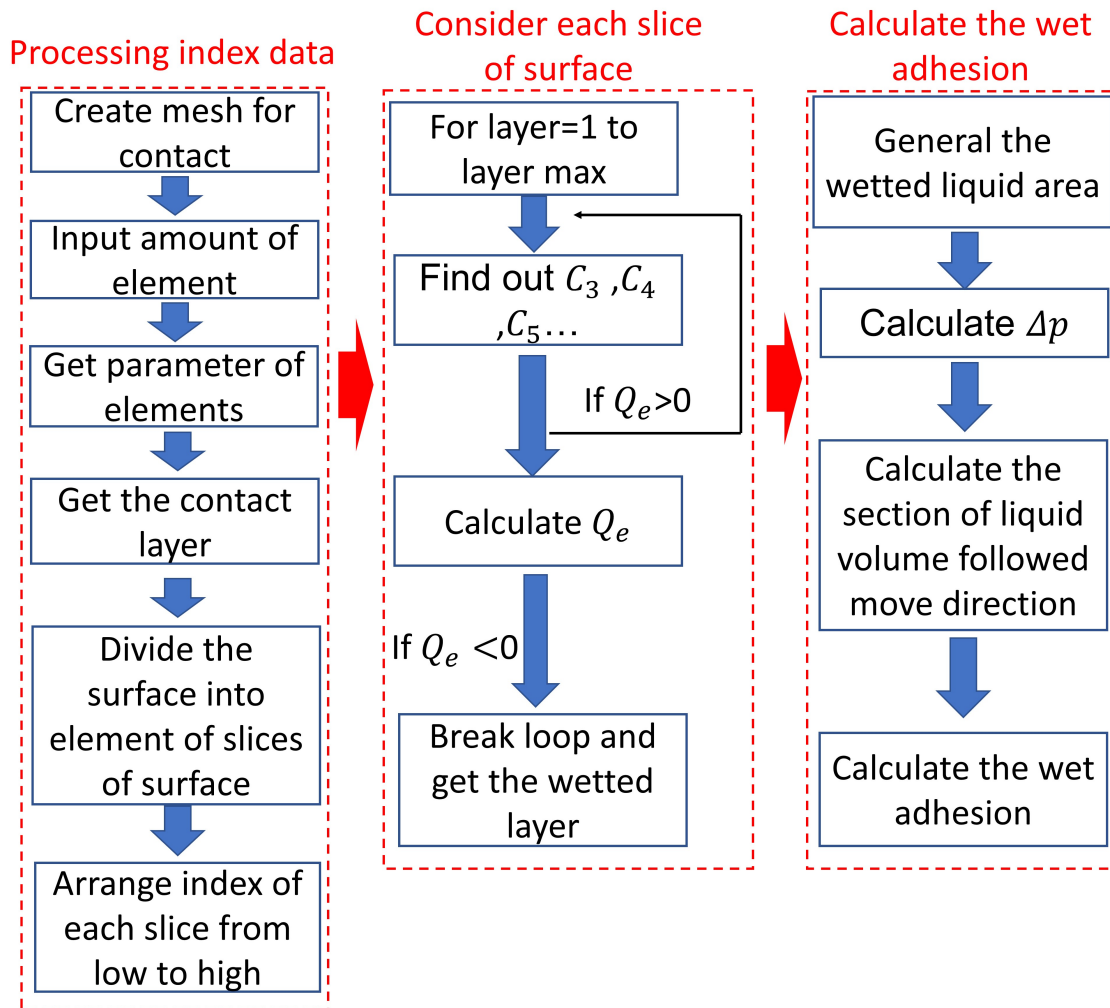


FIGURE 25: The algorithm of finite element method for estimation of capillary force.

is in the range  $[0;1]$ , meaning that the tension is in the range  $[\frac{\gamma_l}{4}; \gamma_l]$ . Below, we run the model to determine the parameters of the height of the liquid rising above the solid surface and the radius of the liquid surface for values of liquid tension energy determined respectively at  $0.0016 \text{ N/m}^2$ ,  $0.002 \text{ N/m}^2$ ,  $0.004 \text{ N/m}^2$ . The size of the dome pad in the simulation is illustrated in Fig.28. It also shows the trend of the liquid rising on the solid surface in the context of increasing tension energy of the solid. It is evident that within the range  $[\frac{\gamma_l}{4}; \gamma_l]$ , the level of the wet-adhered liquid on the solid surface gradually increases. Fig.29 compares, at increasing levels of liquid tension energy, the convergence rate to the maximum height of the liquid rising on the solid surface, which increases with the same considered contact angle. Finally, Fig.30 shows that the radius of the surface of the wet-adhered liquid block will be proportional to the height of the rising liquid.

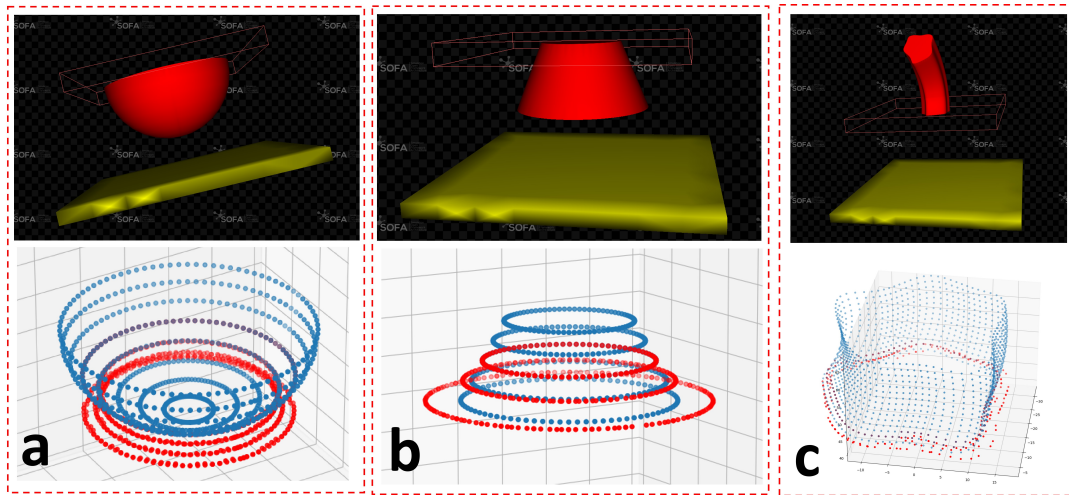


FIGURE 26: SOFA simulation for capillary phenomenon. Note that red dotted boundaries show the uplifted water layer due to adhesion. (a) Dome shape object. (b) Truncated cone shape object. (c) General geometry object

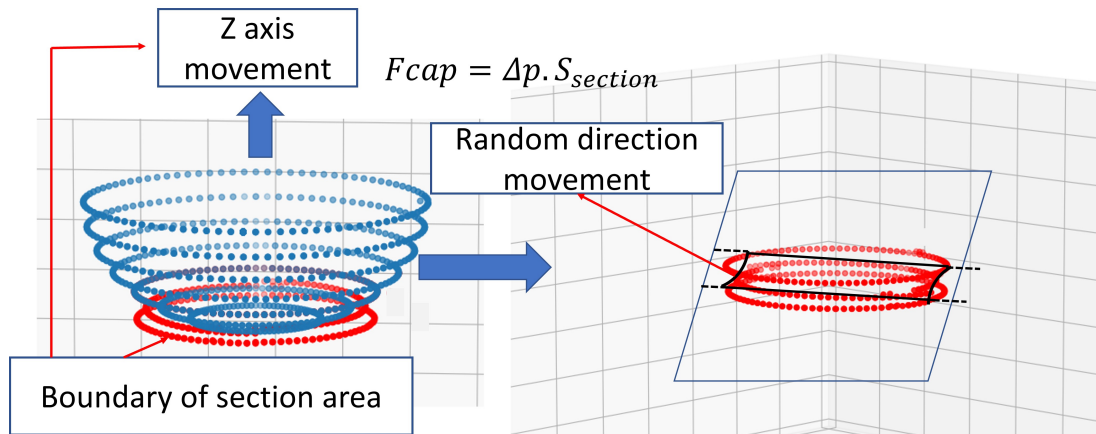


FIGURE 27: Tangential capillary force estimation following the wetted liquid and movement direction, where  $S_{section}$  is the projected area of the wetting liquid on a plane perpendicular to the direction of motion.

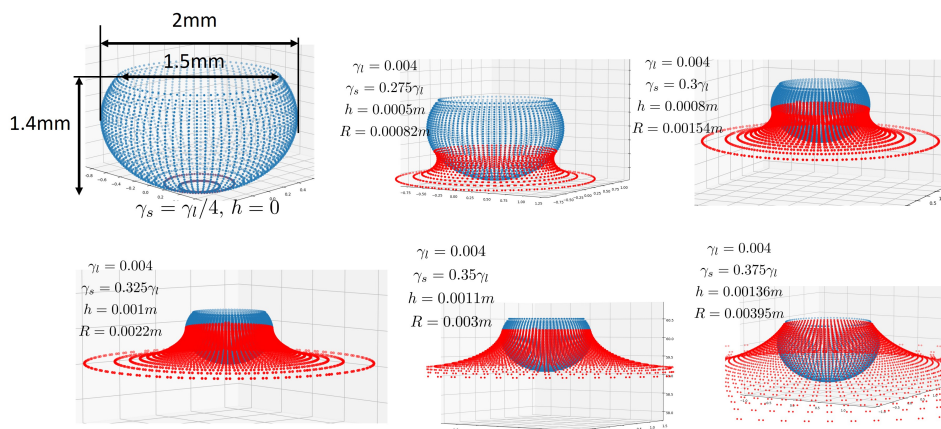


FIGURE 28: Wet adhesion parameters simulating in case of  $\gamma_l = 0.004 \text{ N/m}^2$  with the rising of  $\gamma_s$  (simulation using SOFA.)

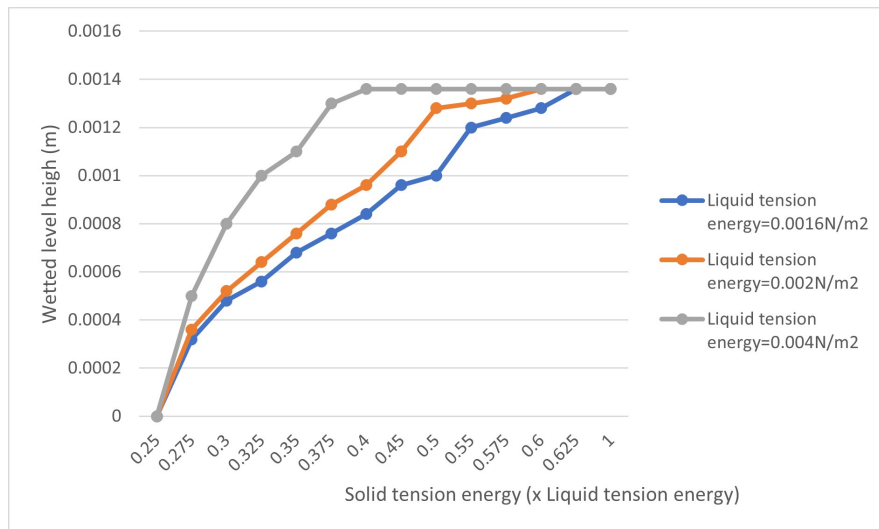


FIGURE 29: The relationship between surface tension energies and wetted height.

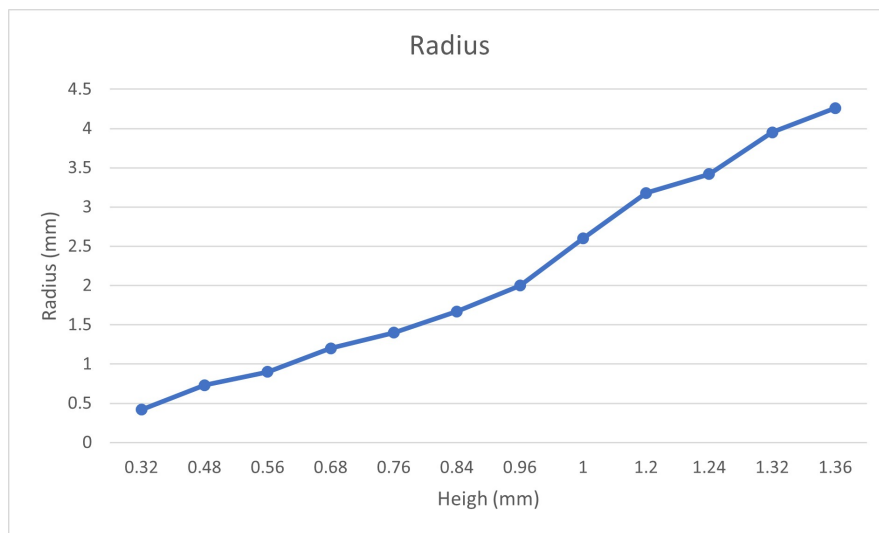


FIGURE 30: The relationship between wetted heigh and radius of wetted liquid curvature.

This investigation is more convincing if this estimation would be accompanied by validating experiments. However, evaluating the experimental accuracy of these surface parameters in wet adhesion phenomena poses a challenge due to equipment and technique demands, including imaging technology and the complexity of tension energy in various liquid and solid types. So we just investigated the trends of those parameters and compared with other studies [39].

## 4.2.2 The FEA-based model for the capillary phenomenon of the patterned pad

In the previous subsection, our approach was employed to simulate wet adhesion, which related to the ability of a liquid to adhere to a solid surface. When a liquid encounters a solid surface, it has the potential to either spread out and form a thin film or cluster together into droplets. Conversely, capillary action is the phenomenon in which a liquid can move against the force of gravity within confined spaces, such as narrow tubes or amidst small particles. This behavior arises due to the combined cohesive forces among liquid molecules and adhesive forces between the liquid and the solid surface. In scenarios with narrower spaces, the liquid is drawn upward to a greater extent through capillary action.

In this subsection, we propose a FE method to estimate capillary forces in the case of multiple pads on our changeable-pad foot. The narrow spaces among the pads, which can be controlled by adjusting the inner pressure, are considered as important factors affecting the capillary force. Fig. 31 illustrates the distribution of soft pads on the foot area. The mesh element parameters are obtained using the tools GMSH and SOFA. In this scenario, the equilibrium energy equations are formulated by considering the relationship between the space occupied by the liquid and the work of capillary force. Let  $n$  represent the total number of domes, and  $W_e$  that explicitly formulated as given in Eq.4.4 denote the work of capillary force that lifts the liquid to its equilibrium height. Subsequently, we use the  $W_e$  formula to calculate the total work of capillary force as follows:

$$W_{tot} = nW_e. \quad (4.19)$$

Considering the influence of both viscous dissipation and potential energy, as elucidated in Equations Eq. 4.6 and Eq. 4.8, we proceed to compute the volume of each liquid layer with the following approach. Within this context,  $d_z$  signifies the height of the layer element,  $S_{bo}$  denotes the boundary area of the dome, and  $V_{sph}$  represents



the volume of each dome submerged beneath the liquid:

$$V_n = dzS_{bo} - nS_{sph(i)}, \quad (4.20)$$

$$K_{tot} = \sum_{i=0}^n \rho g z_n (dzS_{bo} - nV_{sph(i)}), \quad (4.21)$$

$$\Delta U_{tot} = \sum_{i=0}^n \rho g z_n (dzS_{bo} - nV_{sph(i)}). \quad (4.22)$$

The values of  $d_z$ ,  $S_{bo}$ , and  $V_{sph}$  are obtained from the mesh data of GMSH and SOFA. Gmsh is a powerful open-source finite element mesh generator used for 3D object discretization. With Gmsh, complex 3D geometries can be divided into smaller elements, simplifying the numerical analysis of various physical processes, including

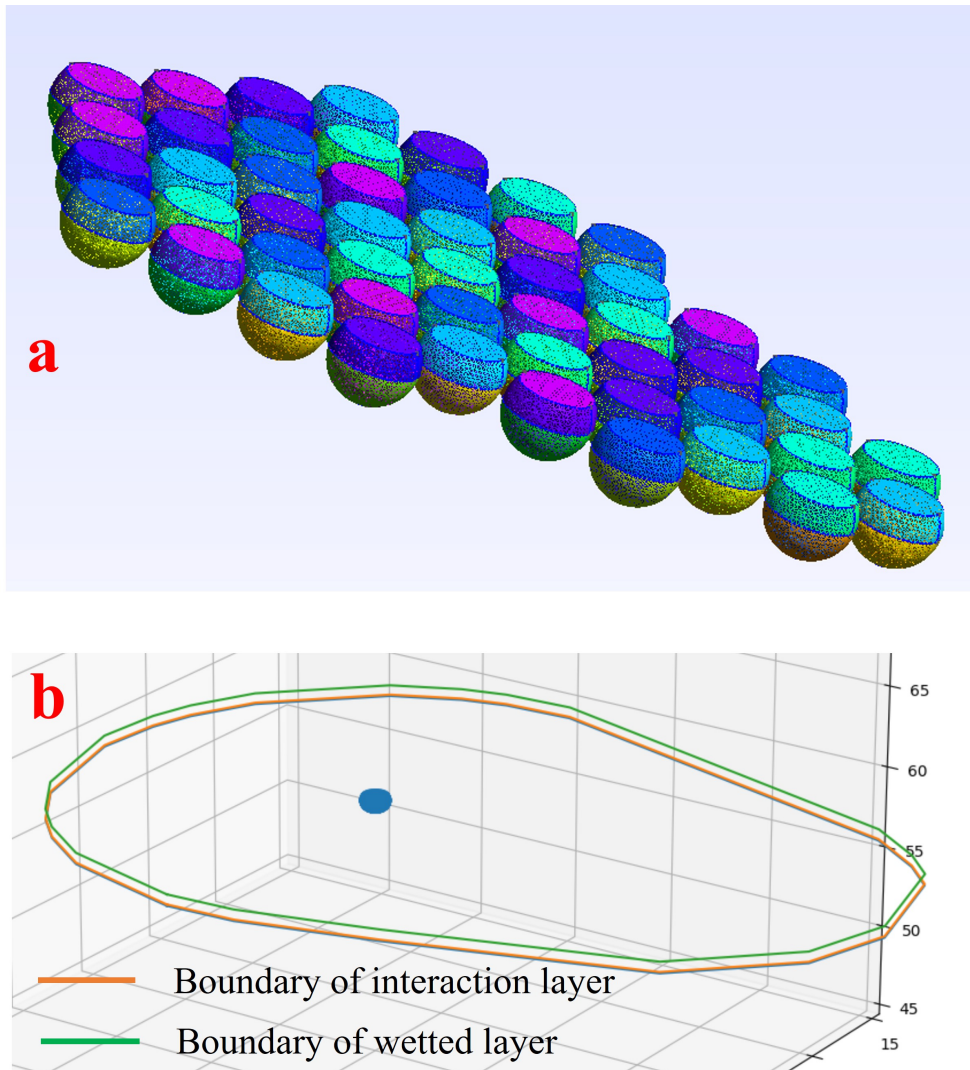


FIGURE 31: SOFA simulation of wet liquid for soft pads foot. (a) Changeable soft pads foot meshing in SOFA. (b) Height of rising wet liquid.



structural mechanics, fluid dynamics, and more. It offers a user-friendly interface and an useful set of tools for mesh creation, making it an important asset in the field of computational engineering and science. Whether you're simulating the behavior of mechanical components or studying fluid flows within complex structures, Gmsh provides the means to generate high-quality 3D meshes that are used for accurate simulations and in-depth analysis.

Therefore, similar to the previous subsection, a loop is utilized to determine the height of the rising liquid through the energy function  $Q_{tot}$  as follows:

$$Q_{tot} = W_{tot} - K_{tot} + \Delta U_{tot}. \quad (4.23)$$

In Fig. 31, we present an overview of our simulation procedure. We utilize a balance energy function to predict the liquid layer's height. By considering the geometric properties of the liquid's shape, we calculate the tangential capillary force, as detailed in Eq. 4.18. The subsequent section focuses on the thorough evaluation of our methodology's accuracy and reliability, including conducting experiments to validate the computed forces. This experimental assessment is a critical step in verifying the real-world applicability and effectiveness of our simulation.

## 4.3 Experimental validation

### 4.3.1 Tangential force experiment

In this section, we assess the impact of capillary action on the morphologically changeable foot's resistance to slippage. The experimental setup is depicted in Fig. 32, which comprises two motorized linear stages facilitating vertical and horizontal movements. This arrangement involved two key components: a vertical linear stage motor responsible for vertical motion and a horizontal linear stage motor governing forward and backward movements. The soft pad foot was securely attached to the vertical linear stage motor, serving as the focal point of the experiment. In this setup, as the soft pad made contact with the surface, it was subjected to controlled

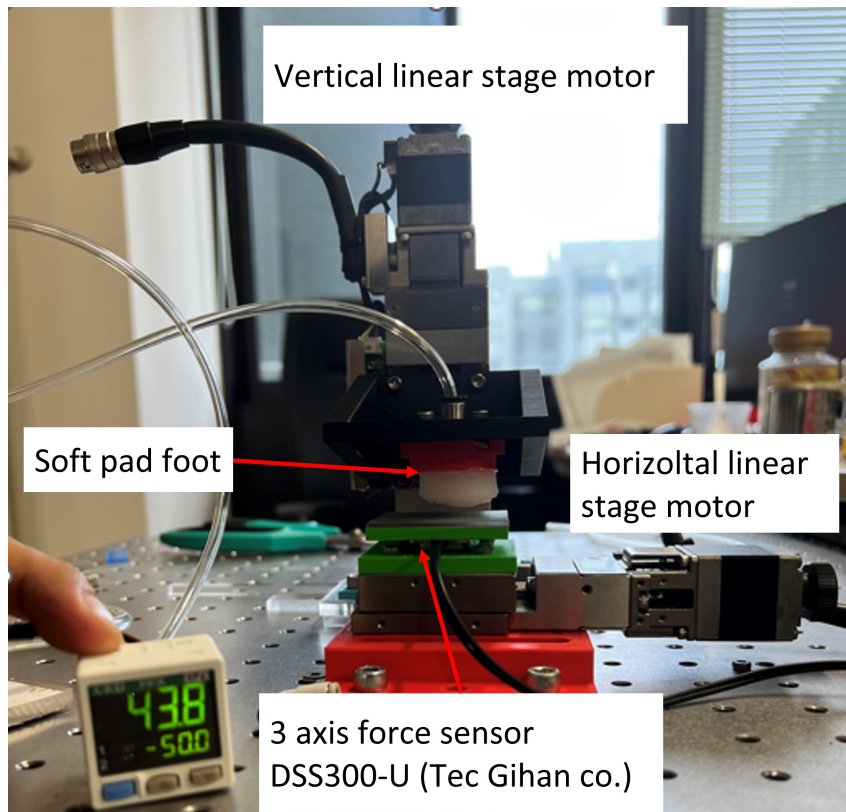


FIGURE 32: Experimental setup of the tangential force.

conditions under both wet and dry circumstances. The horizontal linear stage motor played a pivotal role, creating motion and inducing tangential forces that resisted this motion. The measurement of these tangential resistant forces was a key objective of the experiment. The experimental procedure was as follows: the soft pad foot was gradually pressed onto the surface, with the tests conducted under varying wet and dry conditions. As the soft pad came into contact with the surface, the horizontal linear stage motor initiated its movement, generating a controlled motion. During this motion, the tangential resistant forces were measured. This approach allowed us to gather data regarding the pad's performance and its ability to resist slippage in response to diverse conditions. The results obtained from this experimental setup investigate the interaction between the soft pad and different surfaces, focus on its effectiveness and adaptability.

The experimentation was conducted under both wet and dry conditions, varying the soft pad morphology from flat to domed under an air pressure of 50 kPa. The resultant capillary force  $F_{\text{cap}}$  was derived as the difference between  $F_{\text{wet}}$  and

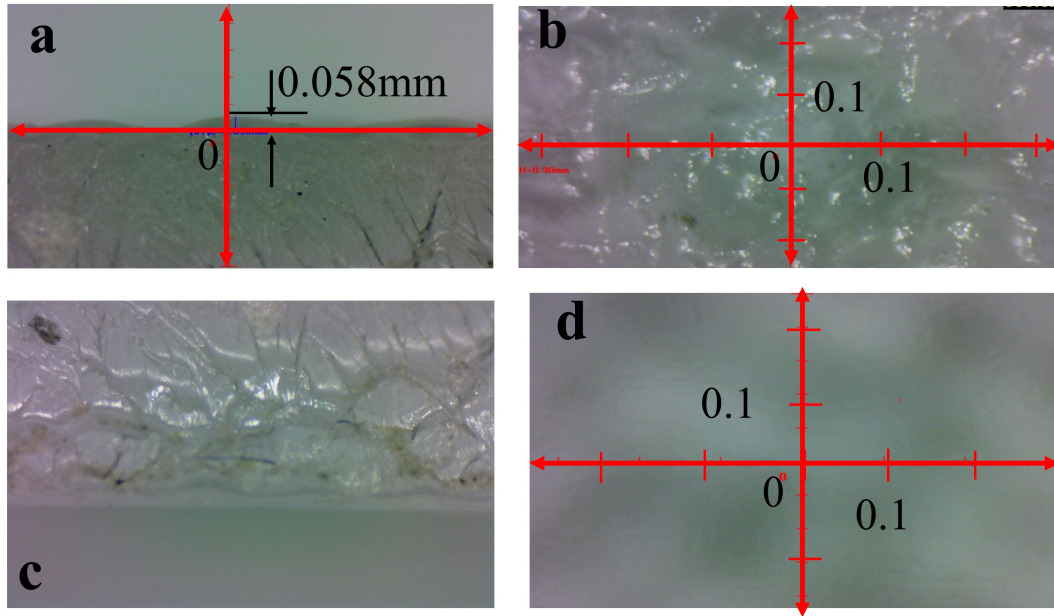


FIGURE 33: Microscopic images of the experimental soft plastic layer surface: (a) presents the projection of the convex elevation on the rough surface, (b) shows the projection of the roughness density on the rough surface, (c) demonstrates the projection of the smooth surface, (d) displays the projection of the roughness density on the smooth surface.

$F_{\text{dry}}$ , corresponding to the tangential forces measured in the respective conditions, specifically  $F_{\text{cap}} = F_{\text{wet}} - F_{\text{dry}}$ . The experimental trial initiated with the soft pad being pressed against a surface affixed to a 3-axis force sensor (DSS300-U, TecGihan, Japan) under varying contact force intensities. Subsequently, the horizontal linear stage was activated to apply tangential displacement to the soft pad at a velocity of 0.2 mm/s, a rate chosen to minimize any influence from viscosity.

The experimental design included two distinct surface conditions: one with a rough texture and the other with a smoother soft plastic surface (as depicted in the photo within Fig. 33, captured using a 400-CAM058 microscope from SANWA SUPPLY, JAPAN). The influence of surface roughness on capillary phenomena is a multifaceted aspect that lies beyond the primary focus of this study. However, to ensure comprehensive experimentation, we conducted force measurements across these varying surface roughness scenarios. The detailed results can be observed in the data presented in Fig. 34.

The outcomes presented in Fig. 34 depict a noticeable trend in capillary forces

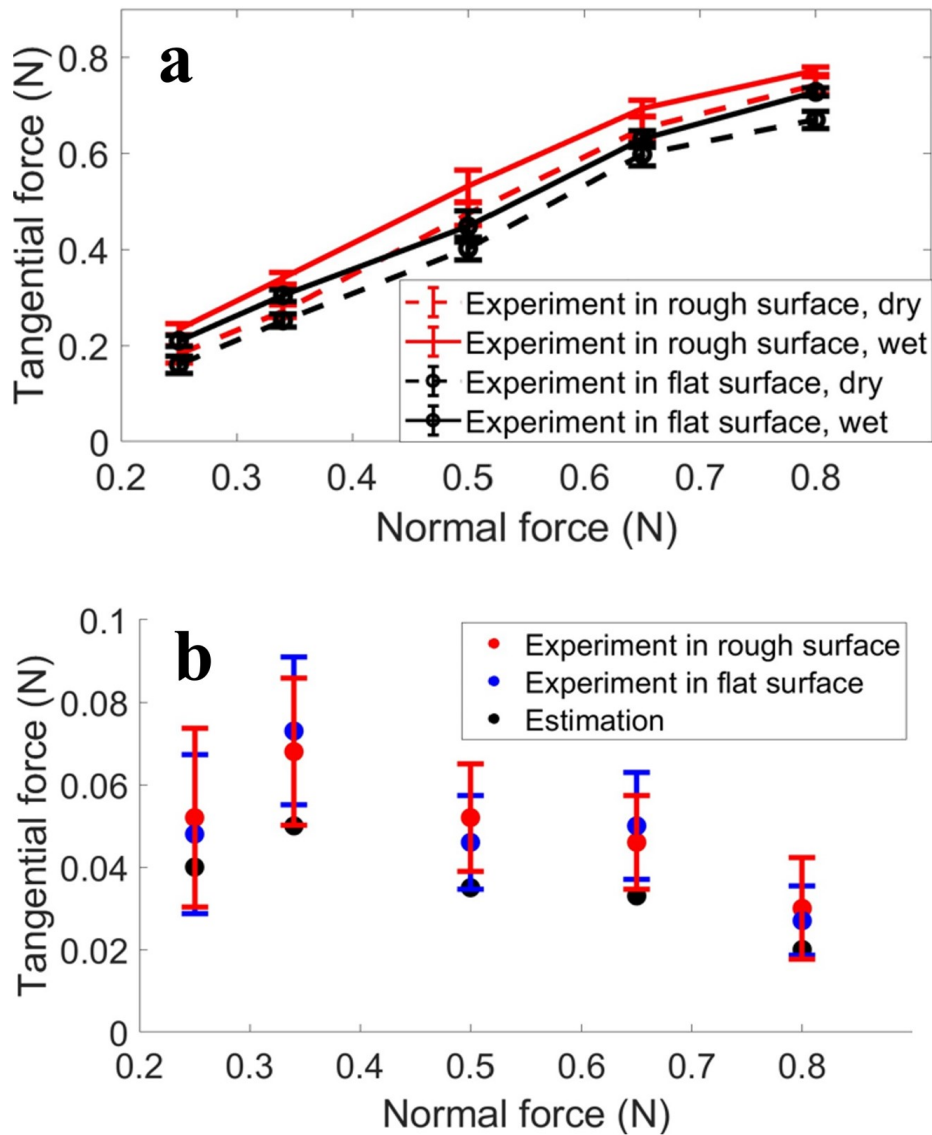


FIGURE 34: (a) Comparison of resulted tangential forces among flat soft pads foot, and domed pads on both wet and dry floors in two different roughness. (b) Comparison of capillary action in wet condition ( $F_{cap} = F_{wet} - F_{dry}$ ) between experiment (with error bars) and estimation results.

across different surfaces. There is an error attributed to the limitations in measurement accuracy. Simultaneously, the friction forces exhibit a linear relationship with the applied contact force on the surface. These results closely correspond with the calculations from the mathematical model detailed in the previous section, with an error of approximately 15% to 25%.

In the Fig. 34.a, the relationship between tangential force and normal force is affected by friction and adhesion. Capillary force, although not proportional to the normal force, doesn't significantly contribute to the observed trend in tangential force as its influence is much smaller. Previous research extensively studied models

where tangential force is proportional to the normal force, as cited in [61], [62], [63], [64]. In our study, we specifically focus on capillary force rather than giving much attention to friction and adhesion.

The wet adhesion and capillary phenomena have been reexamined using the finite element analysis (FEA) approach, contributing to simulation solutions within the SOFA (Simulation Open Framework Architecture) framework. The results obtained from these solutions have been carefully verified through experiments. In the next chapter, showcases integrating morphology-changeable soft pads into a legged robot will be conducted to demonstrate the applicable potential of our design.

# 5 Application to slippage resistance of locomotive robot on wet surface

## 5.1 Design and fabrication

In this chapter, we present the design and fabrication processes for two distinct foot sizes: large-scale and small-scale. Each of these processes has advantages and disadvantages, making them better suited for specific robotic applications.

In the case of the large-scale fabrication process (refer to Fig. 35), the foot benefits from enhanced stability, primarily attributed to the presence of a rigid bone encased within the soft foot structure. However, it's worth noting that the tangential force optimization is not optimal, and we delved into this aspect further in the subsequent Optimization section.

Conversely, in the small-scale fabrication process (as depicted in Fig. 36), we prioritize the optimization of tangential force, significantly improving the foot's ability to avoid slippage. Nevertheless, it's crucial to highlight that under high inner pressure conditions, the set of soft pads experiences deformation, ultimately adopting a dome-like shape.

Below, we provide an explanation of both the design and fabrication processes for these two distinct foot sizes. In particular, the drawing used for fabrication process is present in the Appendix 1: Appendix 1.1: Drawing of mold design for large scale foot, and Appendix 1.2: Drawing of mold design for small scale foot (Chapter 7: Appendix)



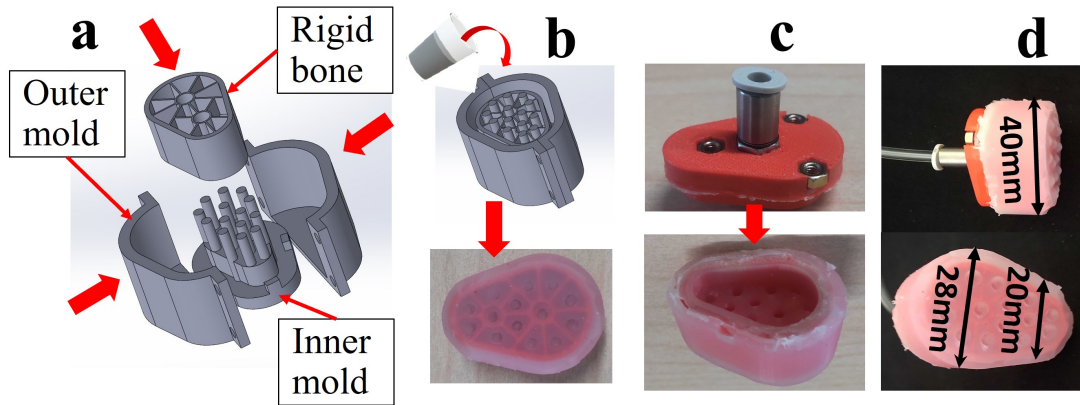


FIGURE 35: Fabrication procedure: (a) Arrangement of the foot mold. (b) Pouring of silicone material. (c) Finalizing the foot structure. (d) Soft pad with applied pressure and dimensions.

### 5.1.1 Large scale design

The design of the foot in the case of large scale is shown in Fig. 35c and 35d, showcasing the inner "bone" structure, which is printed by ZOTRAZ-300 3D printer. This inner structure serves as the rigid core of our design. Wrapping around this core is a membrane of silicone skin, adding a layer of flexibility and tactile sensitivity to the design. The pivotal component, the sole, hosts an array of spherical domes, as illustrated in Fig. 35b.

Initially, in its rest state, the sole of the foot is flat, as exhibited in Fig. 35d. When providing inner pressure, the soft pad domes emerge in response to the increasing air pressure. This transformation is central to the foot's performance, changing its morphology to adapt to various surface conditions.

The mechanics of this design may apply to robot functions. The external air-pressure regulator connects to the rigid bone, and this connection plays a pivotal role in controlling the inflation and deflation of the soft pad domes. When air pressure is applied, these domes engage, adjusting the sole's morphology to facilitate walking on surfaces with different characteristics, particularly those that vary between wet and dry condition by sensing the surface and actively adjusting the inner pressure.

The fabrication process, as illustrated in Fig. 35a-c, is a crucial step in crafting our soft robotic foot. The fabrication process is initiated by filling the outer mold

with silicone material, specifically silicone Ecoflex 00-20 from Smooth-On, Inc., USA. This silicone forms the outer layer, covering the rigid bone, and giving shape to the entire foot structure. This step is instrumental in creating the soft, adaptable surface necessary for our robot to adapt to various terrains. Besides, the inner mold serves the purpose of crafting air hoses. These hoses are important for directing and regulating the flow of air, which is responsible for inflating the thin sheet located within the foot structure. This controlled inflation allows the soft pad to morph and adapt to the ground, enhancing its efficiency and versatility. The 3D-printed cap, produced using a ZORTRAX M300 printer and ABS material, plays an important role in the assembly process.

### 5.1.2 Small scale design

In the particular design, a softer sheet material, Silicone Ecoflex 00-20 (Smooth-On, Inc., USA), was employed. This material helps the foot transform into a spherical dome shape when subjected to controlled air pressure adjustments. It is layered on a firmer substrate, Dragon Skin 30 (Smooth-On, Inc., USA), which provides structural support and stability to the soft pad.

The internal architecture of the foot comprises a network of cylindrical chambers, each with a diameter of 1 mm. These chambers serve a function by acting as

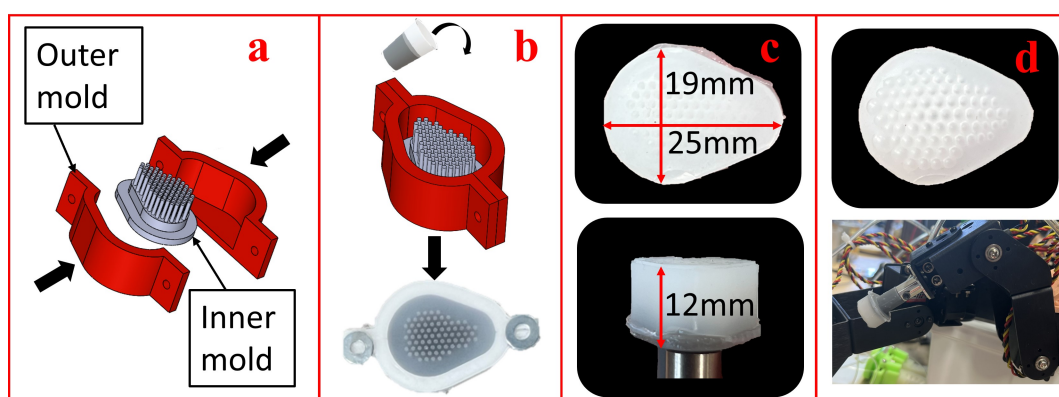


FIGURE 36: Fabrication process: (a) mold set of foot. (b) Pouring silicone include two step: pouring Dragon Skin 30 silicone for the body, then pouring the silicone Ecoflex 00-20 for the thin sheet. (c) Finishing the foot. (d) dome inflation and the robot leg attached the foot.



conduits for the directed flow of compressed air. The air, when appropriately channeled through these chambers, inflates the soft pad. This pad is designed with a thickness of 0.2 mm. An essential design parameter which was considered is the initial radius of these soft pad domes, denoted as  $r_0$ . This value was determined to optimize the tangential force.

The outer molds were fabricated by ZORTRAX M300 printer with ABS material. Besides, the inner mold was printed using a FORMLABS FORM 2 3D printer. The material of choice for this inner mold was grey SLA resin (RS-F2-GPGR-04).

## 5.2 Case of single legged robot with the proposed foot

In this section, we demonstrate the walking efficiency on both wet and dry surfaces using a leg equipped with a foot containing either a flat or a domed soft pad. While our walking system comprises only a single leg for simplicity, the results hold promise in validating the potential applicability of this device in more complex systems in the future.

The walking mechanism consists of a body carrying a stepper motor that drives a one-degree-of-freedom (1-DOF) linkage system, as depicted in Fig. 37a. To assess the effectiveness of preventing foot slippage, we intentionally kept the walking mechanism simple to avoid distraction associated with a more complex system. We utilized a one-leg mechanism moving on four wheels constrained by a rail system, shown in Fig. 37c-d. The basic concept of the linkage mechanism is illustrated in Fig. 37b. The torque  $\tau_1$  generated by the stepper motor produces external forces  $F_1$ ,  $F_2$ ,  $F_3$ ,  $F_4$ . The hinge joint between the foot and the linkage system, supported by two springs, is designed to press the foot to the floor, thus increasing the contact time between the foot and the surface. The external force  $F_4$  causes the foot's backward motion. When the tangential resistance force  $F_{\text{tot}}$  is adequate, slippage between the foot and the surface is prevented, and the foot remains stationary until the reactive forces  $N_1$ ,  $N_2$ ,  $N_3$  push the body forward. The motion of the walking body was tracked using a green marker on the body and three smaller markers attached

to the foot to capture stick/slip motion during walking. A SONY RX10IV(DSC-RX10M4) camera was placed to record marker movement (as shown in Fig. 37c-d). The OpenCV library was used to extract two-dimensional marker movement [65].

By analyzing the contour of the foot based on marker movement, we assessed walking efficiency in five different walking scenarios: 1, On a dry surface (with a flat soft pad); 2, On a wet surface (with a flat soft pad); 3-5, On a wet surface with a domed soft pad pressurized at 40 kPa, 60 kPa, and 75 kPa, respectively. For the first case, the foot posture during walking phases is depicted in Fig. 38a. In this case, the foot makes firm contact with the surface (without slippage), propels the body forward, and then lifts off from the surface in a stable manner.

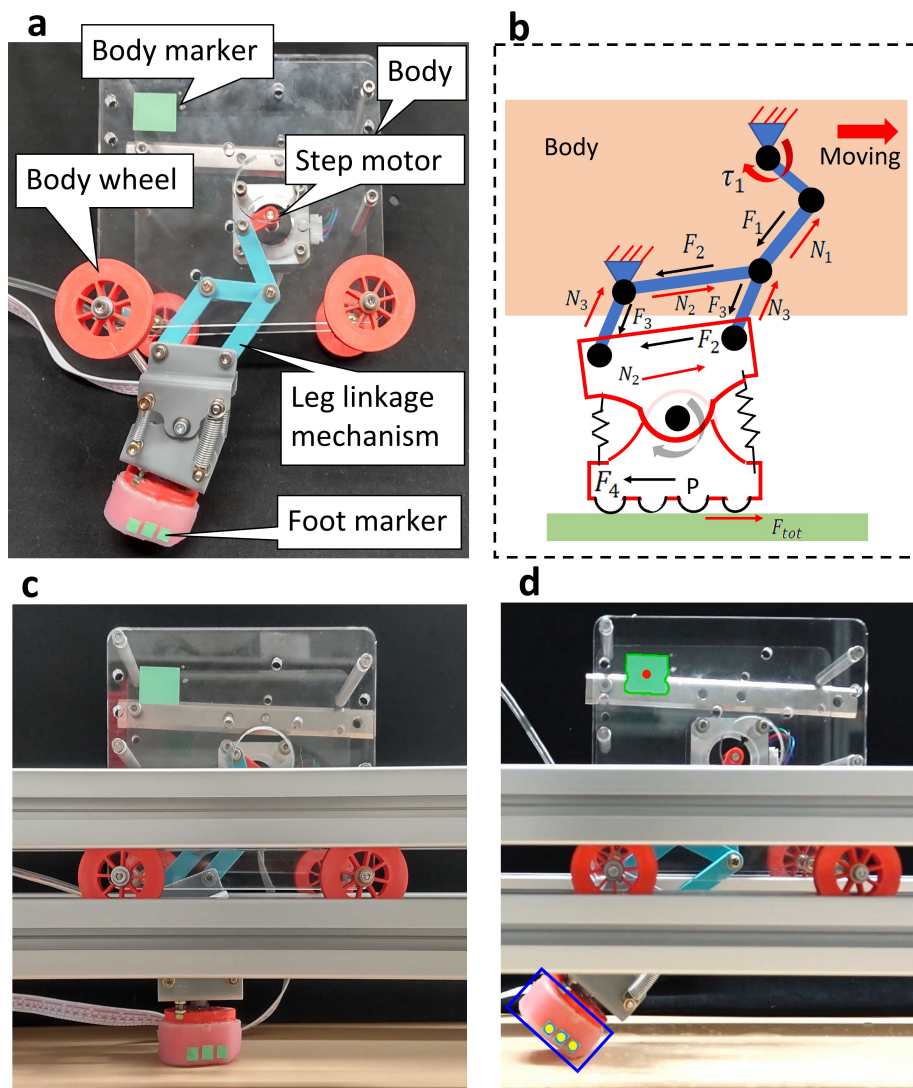


FIGURE 37: Design of the robotic leg. (a) The walking system with its components. (b) Mechanical analysis of the linkage system for walking tests on both (c) dry and (d) wet floors (contour data was tracked to generate the foot paths in Fig. 38).

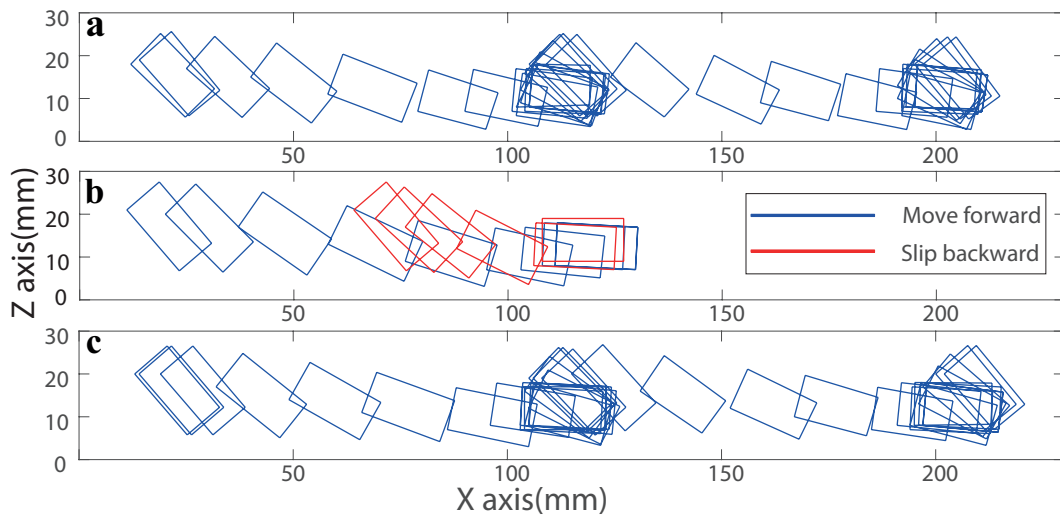


FIGURE 38: Tracked foot's posture (the rectangle in Fig. 37d) during walking action in (a) on a dry floor, (b) on a wet floor with flat foot, and (c) on a wet floor with domed pad (high inner pressure state).

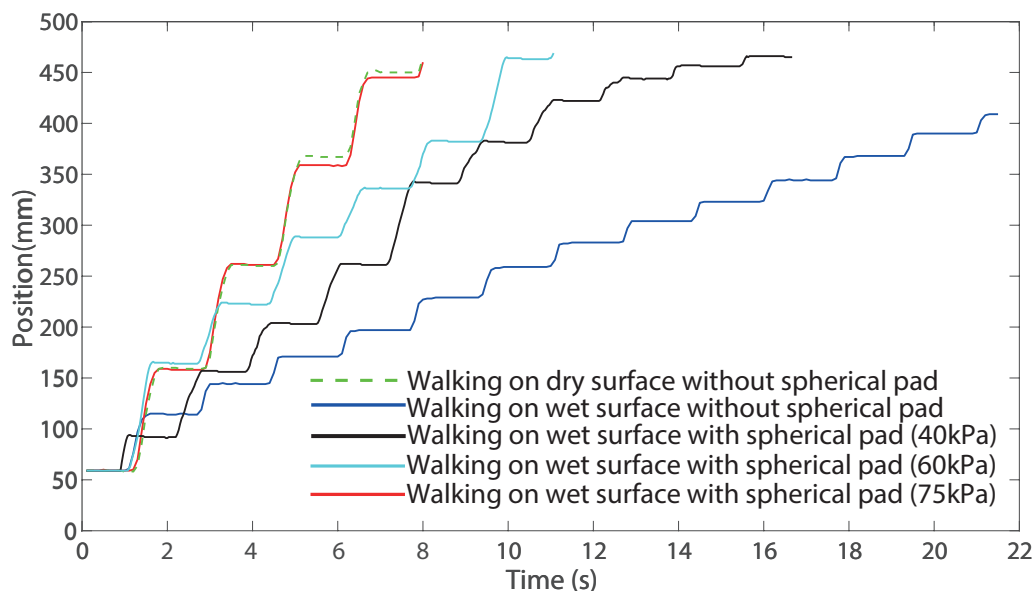


FIGURE 39: Results of the walking robot's body displacement in five experimental conditions (tracked by the marker on the robot body as shown in Fig. 12d).

In the second scenario, the foot's posture is depicted in Fig. 38b. When equipped with a flat soft pad, the foot exhibited poor performance in wet conditions. Upon contact with the wet surface (indicated by blue rectangles), the resultant low tangential force caused the foot to slip backward (indicated by red rectangles) rather than propelling the body forward. This observation aligns with the earlier experimental findings indicating a significant reduction in the tangential force of the flat pad in wet conditions.

In the third case, walking on a wet surface with a domed soft pad showed a locomotion pattern similar to the first case, where a flat soft-padded foot walked on a dry surface. In both cases, there was minimal slippage upon landing of the foot, as demonstrated in the plot in Fig. 38c. This result underscores the potential of the domed soft pad in enhancing walking efficiency in a wet environment.

To summarize the time-series positions of the robot body in all five cases, please refer to Fig. 39. Notably, the movements of the body in case 1 (flat pad, dry surface) and case 5 (domed pad, wet surface, 75 kPa) were quite similar. In both scenarios, the foot executed rapid walking without significant slippage, reaching its destination successfully. However, in case 2 (flat pad, wet surface), reaching the goal took approximately five times longer than in case 5, requiring a much higher number of walking cycles due to slippage.

Varying the morphology of the domed pad with air pressure (at 40 kPa and 60 kPa, respectively) demonstrated that higher pressure notably improved walking performance. In a flat state or a domed state with low air pressure, a layer of liquid became trapped between the foot and the contact surface, changing dry friction-adhesion into lubrication and reducing the tangential resistance force, ultimately leading to slippage. In contrast, with sufficient air pressure, the liquid was expelled from the contact interface to maintain dry friction-adhesion upon contact. Besides, the liquid layer was randomly spread across a large area, making it challenging to ensure uniform distribution around the soft pad's domes. Achieving this specific liquid layer condition was not our objective in this experiment, as securing such conditions in real walking scenarios is difficult. Consequently, the capillary force in the walking leg experiment is smaller than estimated by our analytical model. Nonetheless, the uneven liquid height still generates a capillary force, contributing to tangential capillary effects and aiding the robot in walking on wet surfaces.

### 5.3 Case of hexapod robot with the proposed feet

In this showcase, we show an experiment that use the Hexapod robot developed by Lynxmotion Inc, Canada. Here, our developed soft pads are attached to this robot's feet (see Fig. 40). The robot is a versatile and agile robotic platform characterized by three independent rotational axes of motion. This robotic system mimics the movement of insects with six legs, each of which possesses three degrees of freedom. The three rotational axes typically correspond to the pitch, roll, and yaw orientations, allowing the hexapod to move in a variety of directions and orientations.

In our experimental setup, we employ a straightforward locomotion pattern to guide the robot in a straight path while assessing the performance of its adaptable soft pad foot. The robot's movements are tracked using an optical tracking system (NaturalPoint, Inc. DBA OptiTrack), which collects coordinated data from dedicated markers affixed to each leg (refer to Fig. 40). Additionally, three markers

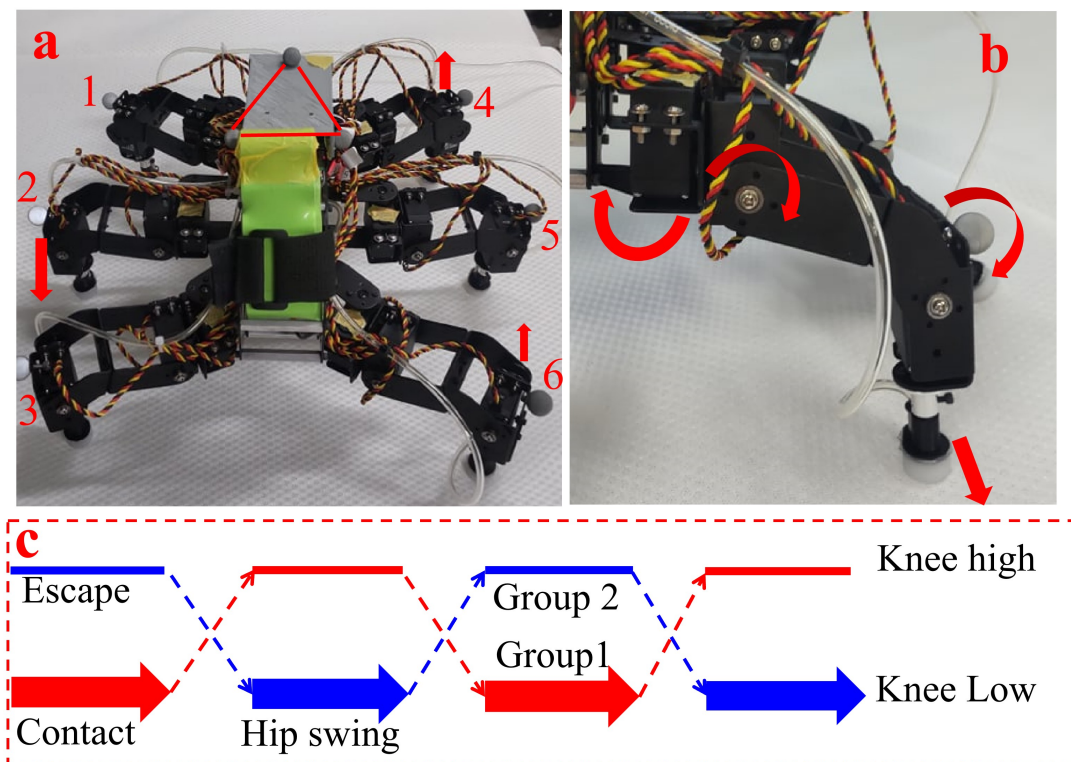


FIGURE 40: 3-Degree-of-Freedom Hexapod robot in the experiment: (a) Hexapod robot with attached markers, (b) leg mechanism illustration. (c) The concept of hexapod locomotion showcased.



placed on the robot's body provide position and orientation information. Typically, a leg mechanism in a 3 DOF hexapod consists of three articulated joints that provide rotational freedom. These joints correspond to the hip, knee, and ankle joints (see Fig. 40b).

The hip joint allows the leg to move forward and backward, as well as to swing laterally to the sides. The knee joint contributes to controlling the leg's height and step length. It decides the time when the foot contact into the floor for moving forward and backward (by swinging the hip joint), or escape from the interaction with the floor. The ankle joint enables the leg to rotate or tilt, allowing the hexapod to adjust its foot orientation to the ground. Ankle joint movement is crucial for maintaining stable contact with the surface. It also aids in adapting the foot's angle for optimal traction during movement.

For this experiment, the robot moves directly forward by activating phase differences between two leg groups: group 1 (legs 1, 3, and 5) and group 2 (legs 2, 4, and 6). Fig. 40c illustrates this locomotion concept. As one group swings its hip joint to move forward, the other group retracts to prepare for its upcoming step. In terms of force analysis, the forces and moments produced by hip swinging are summarized as follows:  $F_{Mov} = F_1 + F_2 + F_3$ ;  $M = F_1l - (F_2 + F_3)l$ , where  $F_1, F_2, F_3$  represent the forces propelling backward leg movement. If the friction force is sufficient, it secures the foot to the floor, and the reaction force  $F_{Mov}$  propels the robot forward. As this movement is linear,  $M = 0$ , yielding  $F_1 = 2F_2 = 2F_3$ . Assessing all leg forces, legs 2 and 5 carry a higher risk of slipping during robot locomotion.

Fig. 41 and Fig. 42 provide a comprehensive overview of the experimental results. On dry surfaces, the robot exhibits robust performance in both smooth and rough terrains, with no signs of slippage. However, when a flat soft pad (no inner pressure) contacts into wet surfaces, issues with backward leg slipping become apparent. Notably, activating the dome pad by increasing the inner pressure significantly mitigates slippage, as observed in Fig. 41 and Fig. 42. These results serve as a valuable assessment of slippage under diverse conditions, with no predefined control rules imposed. Consequently, the robot's trajectory may deviate due to leg

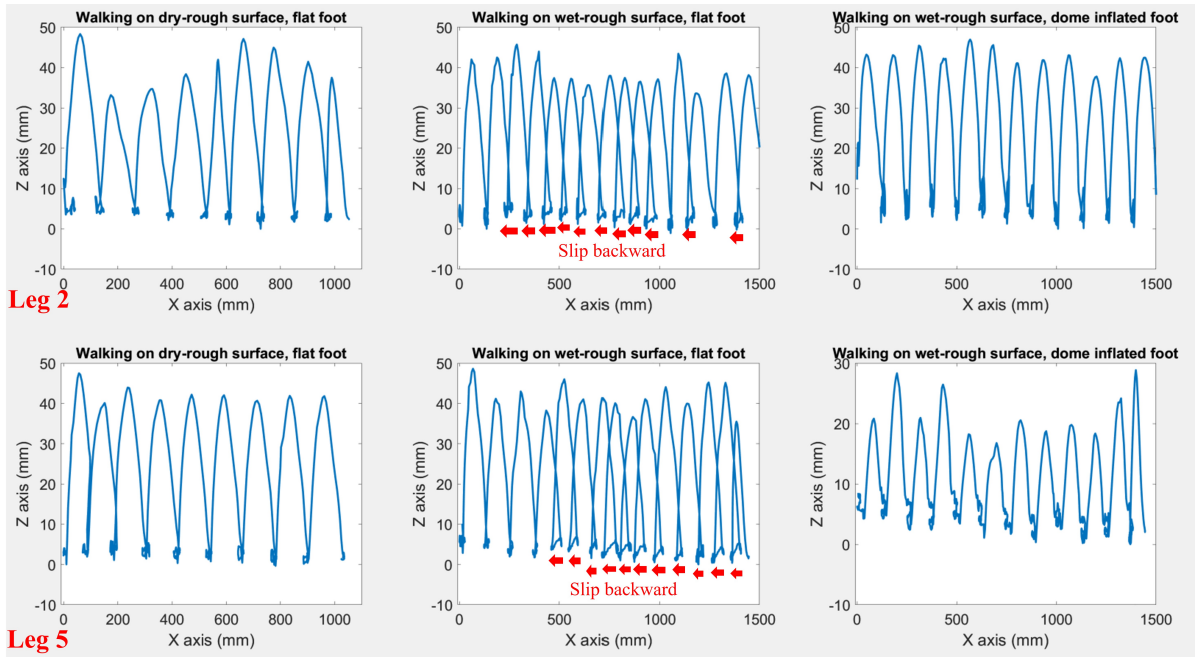


FIGURE 41: The positions of the detected markers on leg 2 and leg 5 of the hexapod while walking on the rough surface, illustrating instances of slippage in different scenarios: walking on dry surface with flat foot, walking on wet surface with flat foot, walking on wet surface with dome pad foot.

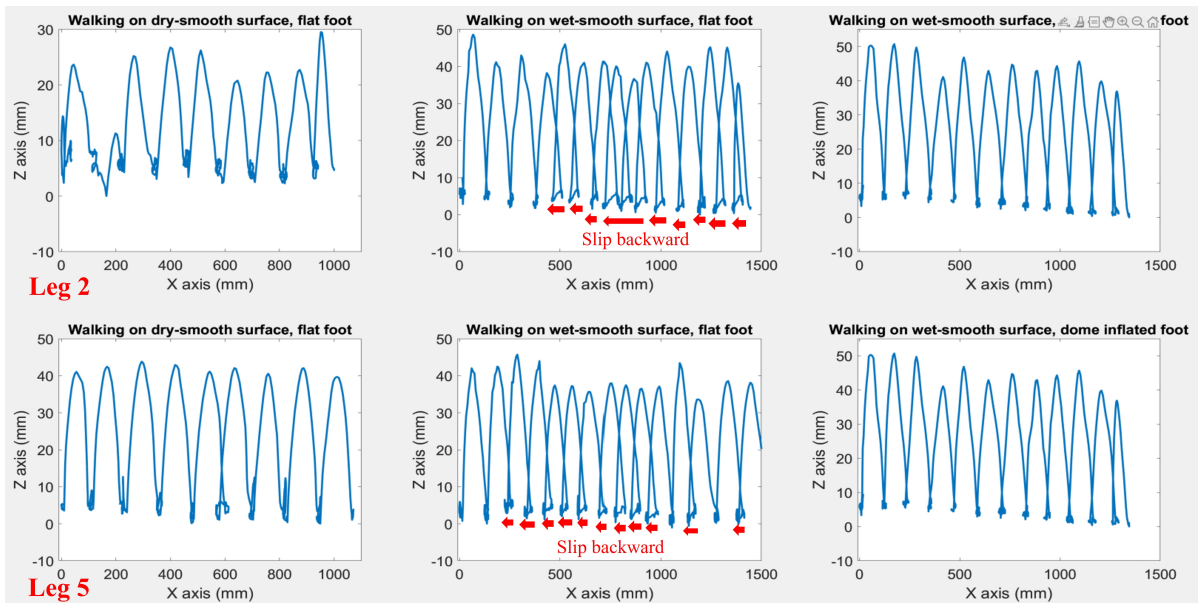


FIGURE 42: The positions of the detected markers on leg 2 and leg 5 of the hexapod while walking on the smooth surface, illustrating instances of slippage in different scenarios: walking on dry surface with flat foot, walking on wet surface with flat foot, walking on wet surface with dome pad foot.

slipping. For a deeper understanding of these outcomes, refer to Fig. 43 and Fig. 44, which depict the paths the robot follows in various experimental scenarios. While navigating wet surfaces with a flat soft pad (absence of inner pressure), the robot

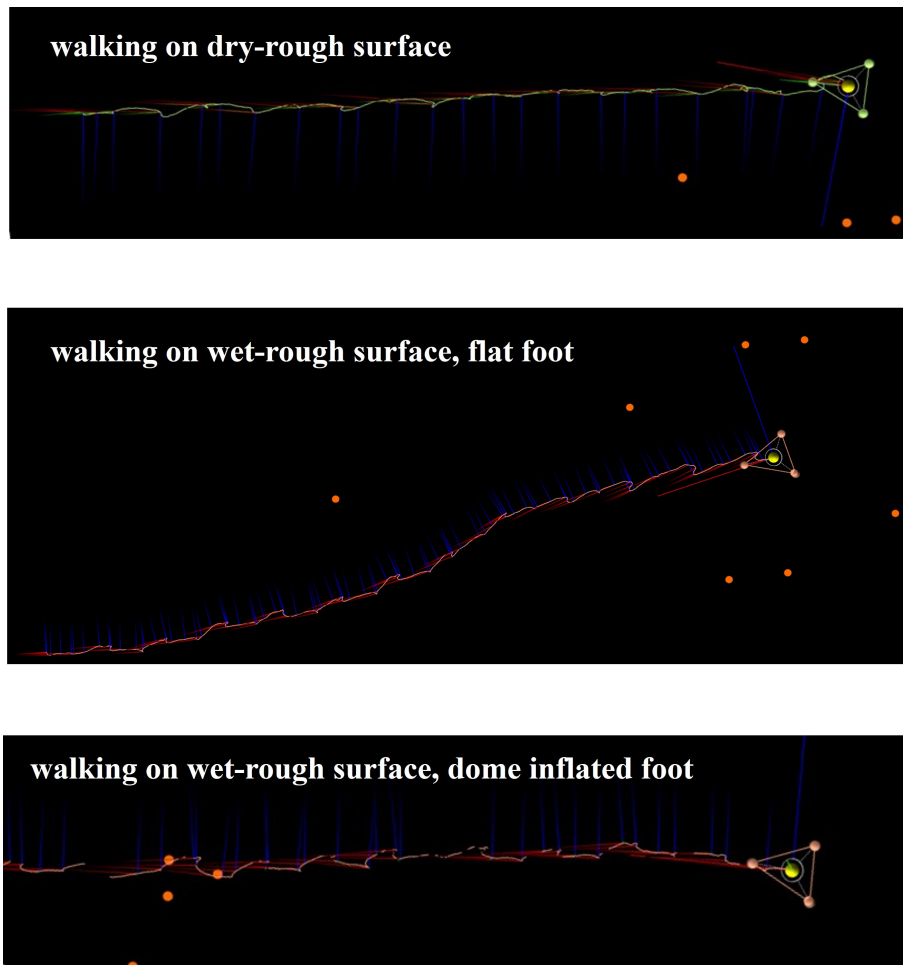


FIGURE 43: The positions of the detected markers on the body of the hexapod while walking on the rough surface in different scenarios: walking on dry surface with flat foot, walking on wet surface with flat foot, walking on wet surface with dome pad foot.

struggles to maintain a straight trajectory, leading to deviations. In contrast, when equipped with the dome pad, slippage is significantly reduced, allowing the robot to uphold a straight course, as evidenced by its trajectory on wet surfaces, which closely resembles its performance on dry terrain.



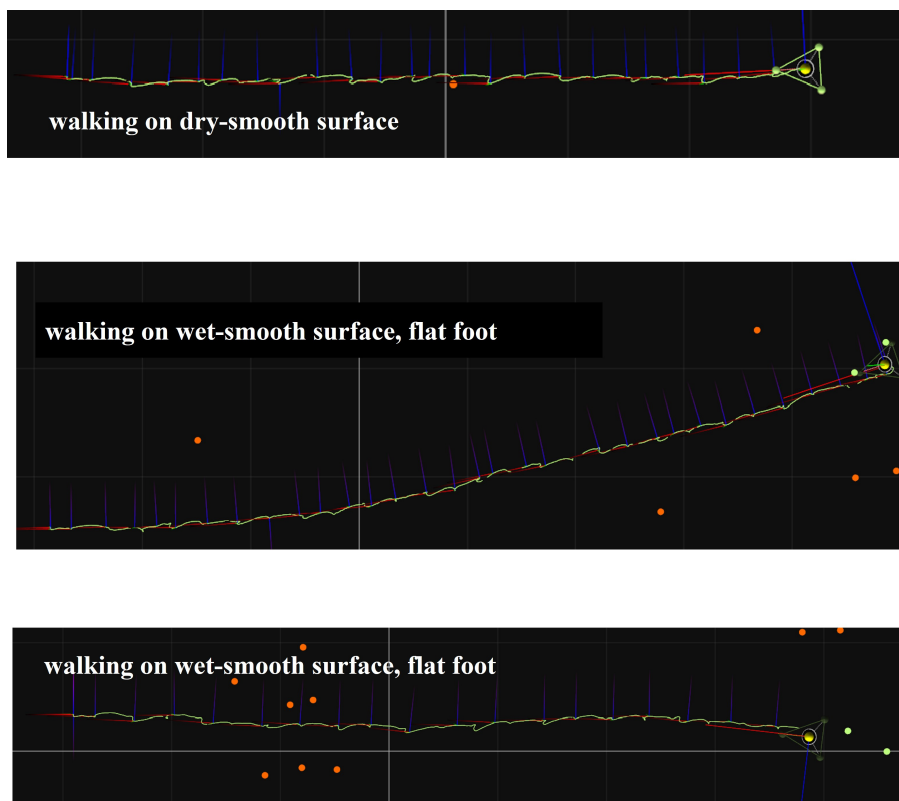


FIGURE 44: The positions of the detected markers on the body of the hexapod while walking on the smooth surface in different scenarios: walking on dry surface with flat foot, walking on wet surface with flat foot, walking on wet surface with dome pad foot.

## 6 Conclusion and Future Works

In the field of soft robotics, our research introduces the mechanics of morphology changeable soft pad that dynamically adjusts the morphology to maximize performance across varying terrains. This novel solution demonstrates the interesting potential of biomimetic engineering, as it draws inspiration from nature's adaptive solutions. Specifically, our novel soft pad design help the robots change their morphology between two primary states: a flat elastic sheet and a protruding spherical dome. The former configuration serves for dry surfaces, offering stability, while the latter enhances efficiency on wet terrains. This feature addresses a crucial challenge in the field of robotics: adaptability to different environments. The contributions of this research may impact the field of robotics through practical applications. Furthermore, our approach introduces a novel solution in wet adhesion and capillary simulation based on the finite element method.

### 6.1 Impact of morphology-changeable soft pads

#### 6.1.1 Design and fabrication

In this study, we have presented a detailed design and fabrication process aimed at realizing a biomimetic approach inspired by the mechanisms found in animal foot pads. The novel concept lies in the development of a morphology-changeable foot pad, carefully designed to optimize friction and adhesion on both dry and wet surfaces. Of significance is the emphasis on exploiting wet adhesion to prevent robot slippage, an aspect that has been relatively understudied until now. The fabrication of the foot pad is conducted through a specially designed mold, ensuring the physical realization aligns with the conceptual framework. To enhance the efficiency

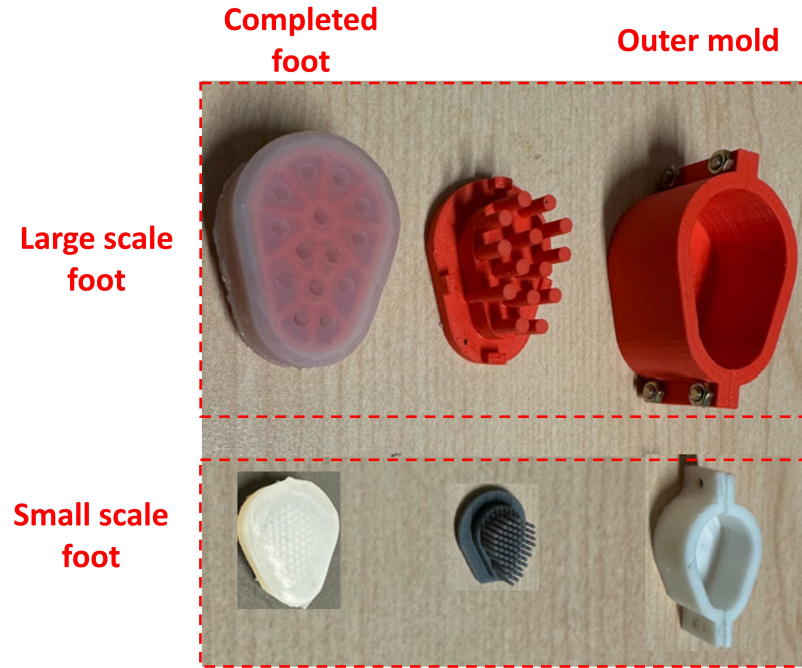


FIGURE 45: Designed mold and completed foot in large and small scale.

of the design and fabrication, we employed optimization algorithms to maximize forces within specific geometrical constraints. Through this work, we expect to contribute to the field of soft robot, providing a robust design and fabrication process applicable in diverse applications. Our optimized approach holds promise for the development of robotics, where the importance of terrain adaptability and wet adhesion has been underscored.

### 6.1.2 Analytical model and finite element method model for Morphology changeable soft dome pad

In conclusion, our research has introduced a novel approach to the design and analysis of morphology-changeable soft pads for robotics applications. The main point of our efforts has been the development of an analytical model based on energy equilibrium equations that examines the morphological properties of the soft pad. This model encompasses the dynamics of tribological aspects, unraveling the interplay of friction, adhesion, and capillary action.

The second analytical model, based on the Finite Element (FE) method, specifically addresses capillary action phenomenon. By adopting this approach, we have

contributed to the understanding of liquid-solid interactions. Moreover, this model serves as a bridge between theoretical concepts and practical applications in robotics. To verify our theoretical model, we conducted force measurement experiments to evaluate the accuracy and reliability of our model. This validation process evaluates our model as a believable approach in the applications of robotics and simulation.

Looking ahead, we expect that our developed model will become an instrumental tool for controlling robots equipped with morphology-changeable soft pads. This tool is expected to provide a reliable means of simulating the complex behavior of liquids in contact with solids, enabling the estimation of wet adhesion forces and capillary forces in real-world scenarios. Our research not only contributes to the theoretical understanding of soft robotics but also proposed a novel tool for advancing the applications of this technology.

### **6.1.3 Application for legged robot walking on different terrain without slippage**

Moreover, our research has developed a novel morphology-changeable soft pad for robot feet, showcasing its exceptional adaptability across diverse terrains. Through experiments, we have successfully demonstrated the transition of a robot equipped with these adaptive soft pads between dry and wet surfaces. The outcomes of our work provide practical validation, suggesting that these soft pads have the potential to enhance the locomotion capabilities of walking robots. Importantly, our findings indicate that the morphology-changeable soft pad foot can offer a useful solution to improve the performance of walking robots when navigating various terrains. This research holds promise for overcoming challenges in complex scenarios where walking robots or humanoid robots need to efficiently complete their tasks. Our research contributes a practical and impactful solution to advance the field of robotics and address real-world challenges associated with adaptability to varied terrains.

## 6.2 Future work

Moving forward, our research lays the groundwork for several future works. First and foremost, there is a need for improving the finite element-based mathematical model algorithm. We expect to incorporate the influence of the calculated capillary force on the mesh of the object, and show the equilibrium state of the object's deformation and the updated capillary force based on that deformation.

Besides, we expect to develop the finite element-based mathematical model algorithm to expand its capabilities to embrace a more comprehensive range of capillary phenomena, ensuring a more accurate representation of the complex interactions between liquids and solids. Delving into the aspects of liquid surface geometry represents a promising direction. An in-depth examination of how liquid shapes interact with different surfaces can deepen our insights, potentially uncovering new information in the behavior of our adaptive soft pads.

Furthermore, the development of adaptive control rules for changing the soft pad's morphology is an important content. This involves control rules that enable the soft pad to dynamically adjust its shape, optimizing the walking robot's performance across diverse terrains. This adaptive capability could prove instrumental in addressing the challenges faced by walking robots operating in real-world, unpredictable surfaces (wet or dry).

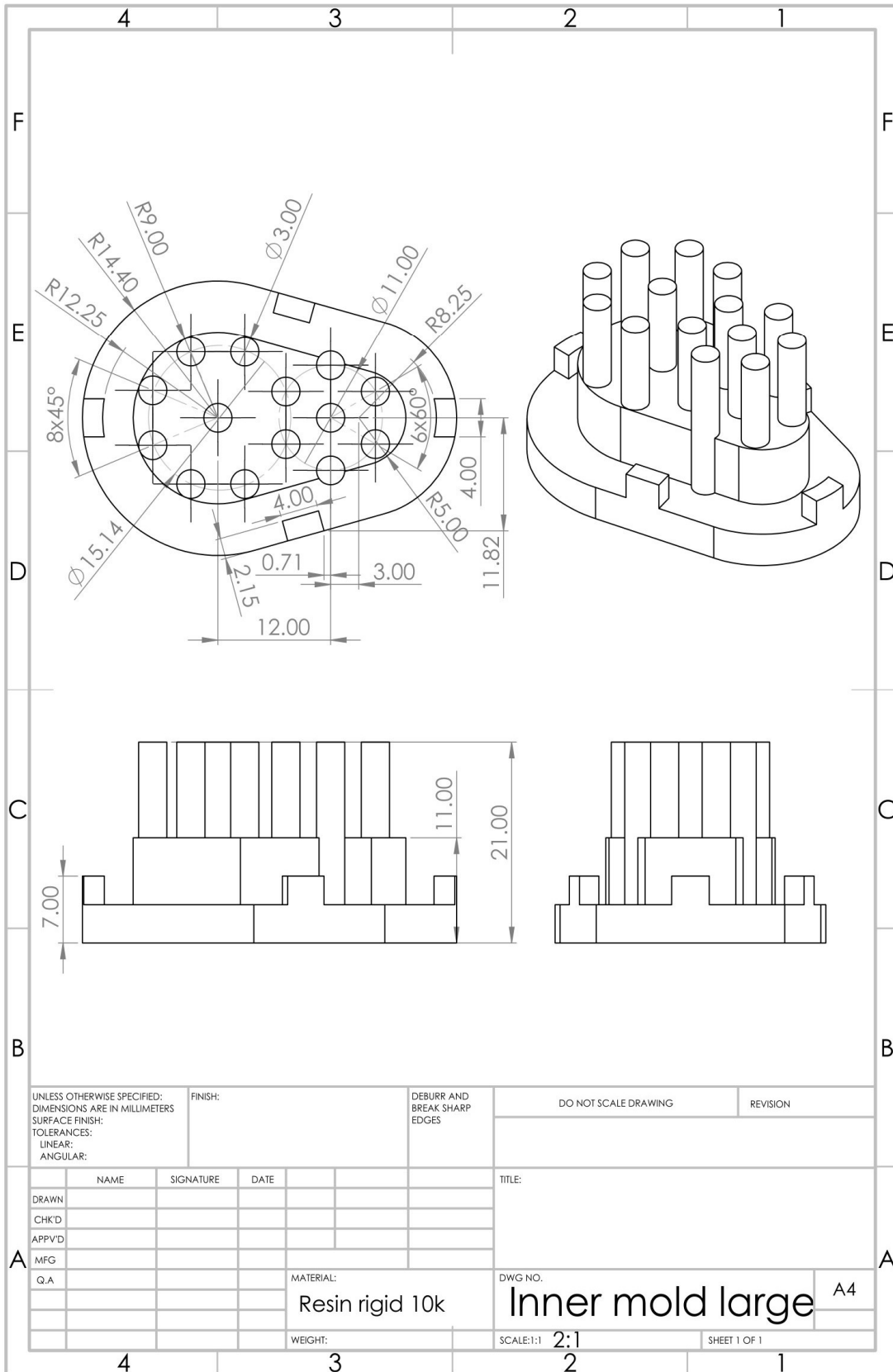
Lastly, a crucial plan for future work involves the development of sensing technology. Specifically, there's a need to create a sensing mechanism capable of detecting tangential resistant forces. This development would draw on our evolving understanding of the interactions that occur in soft contact with the surrounding liquid layer. Implementing such a sensing technology could enhance the robot's ability to respond to its environment, fostering increased adaptability and efficiency in a variety of scenarios. In sum, these future works aim to push the practical applications of our research, contributing to the evolution of soft robotics in real-world scenarios.

# 7 Appendix

## 7.1 Appendix 1: Drawing of mold design

This section shows the drawing of mold design and fabrication discussed in Chapter 3, Section 3.1: Design and fabrication. Specifically, Appendix 1.1 is utilized for the fabrication of the large-scale foot (3.1.1), while Appendix 1.2 is employed for the large-scale foot (3.1.2).

### 7.1.1 Appendix 1.1: Drawing of mold design for large scale foot



UNLESS OTHERWISE SPECIFIED:  
DIMENSIONS ARE IN MILLIMETERS  
SURFACE FINISH:  
TOLERANCES:  
LINEAR:  
ANGULAR:

FINISH:

DEBURR AND  
BREAK SHARP  
EDGES

DO NOT SCALE DRAWING

REVISION

	NAME	SIGNATURE	DATE
DRAWN			
CHK'D			
APP'VD			
MFG			
Q.A			

TITLE:

MATERIAL:

Resin rigid 10k

DWG NO.

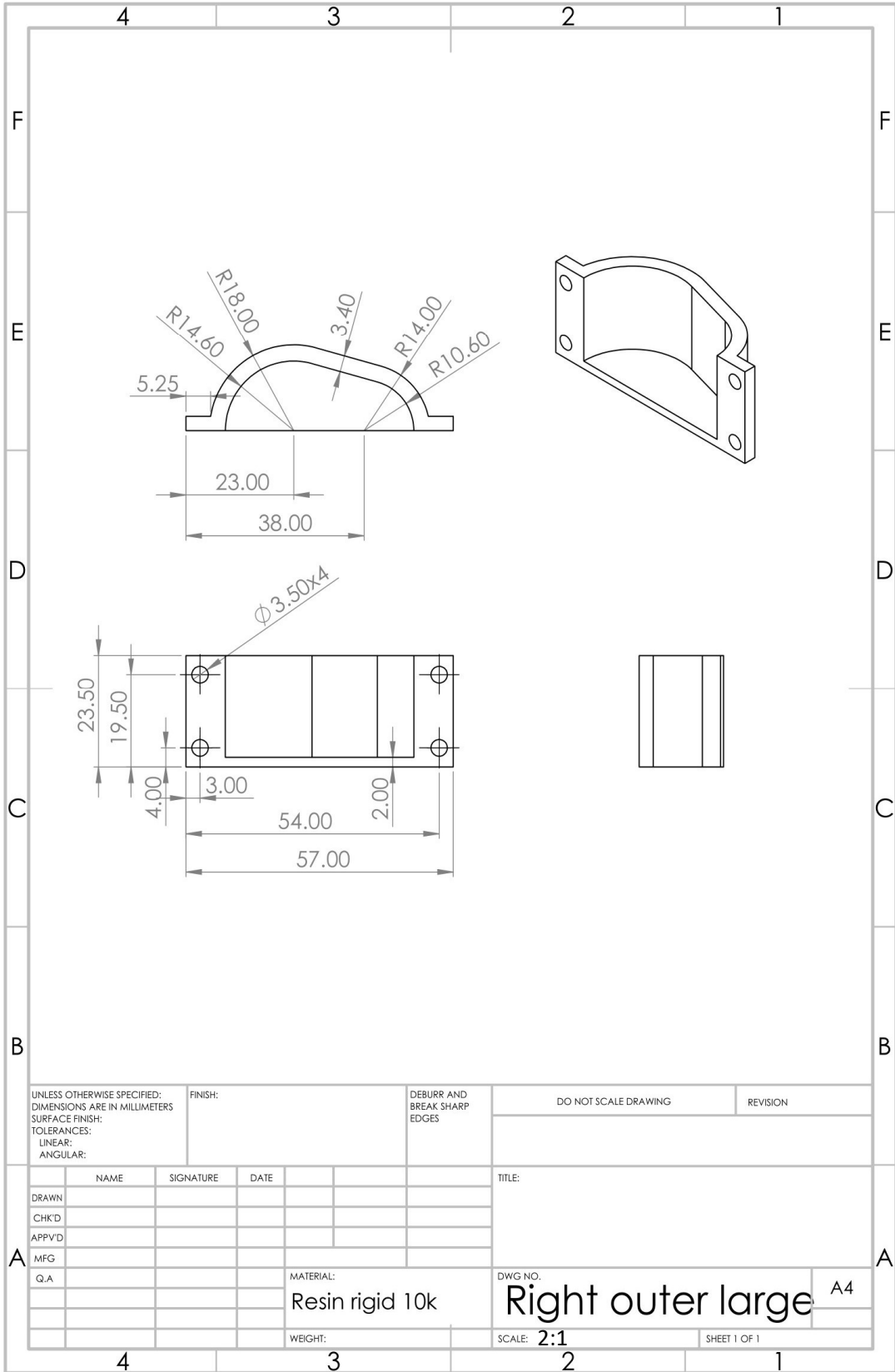
Inner mold large

A4

WEIGHT:

SCALE: 1:1 2:1

SHEET 1 OF 1



UNLESS OTHERWISE SPECIFIED:  
 DIMENSIONS ARE IN MILLIMETERS  
 SURFACE FINISH:  
 TOLERANCES:  
 LINEAR:  
 ANGULAR:

FINISH:

DEBURR AND  
 BREAK SHARP  
 EDGES

DO NOT SCALE DRAWING

REVISION

	NAME	SIGNATURE	DATE
DRAWN			
CHK'D			
APPV'D			
MFG			
Q.A			

TITLE:

MATERIAL:  
 Resin rigid 10k

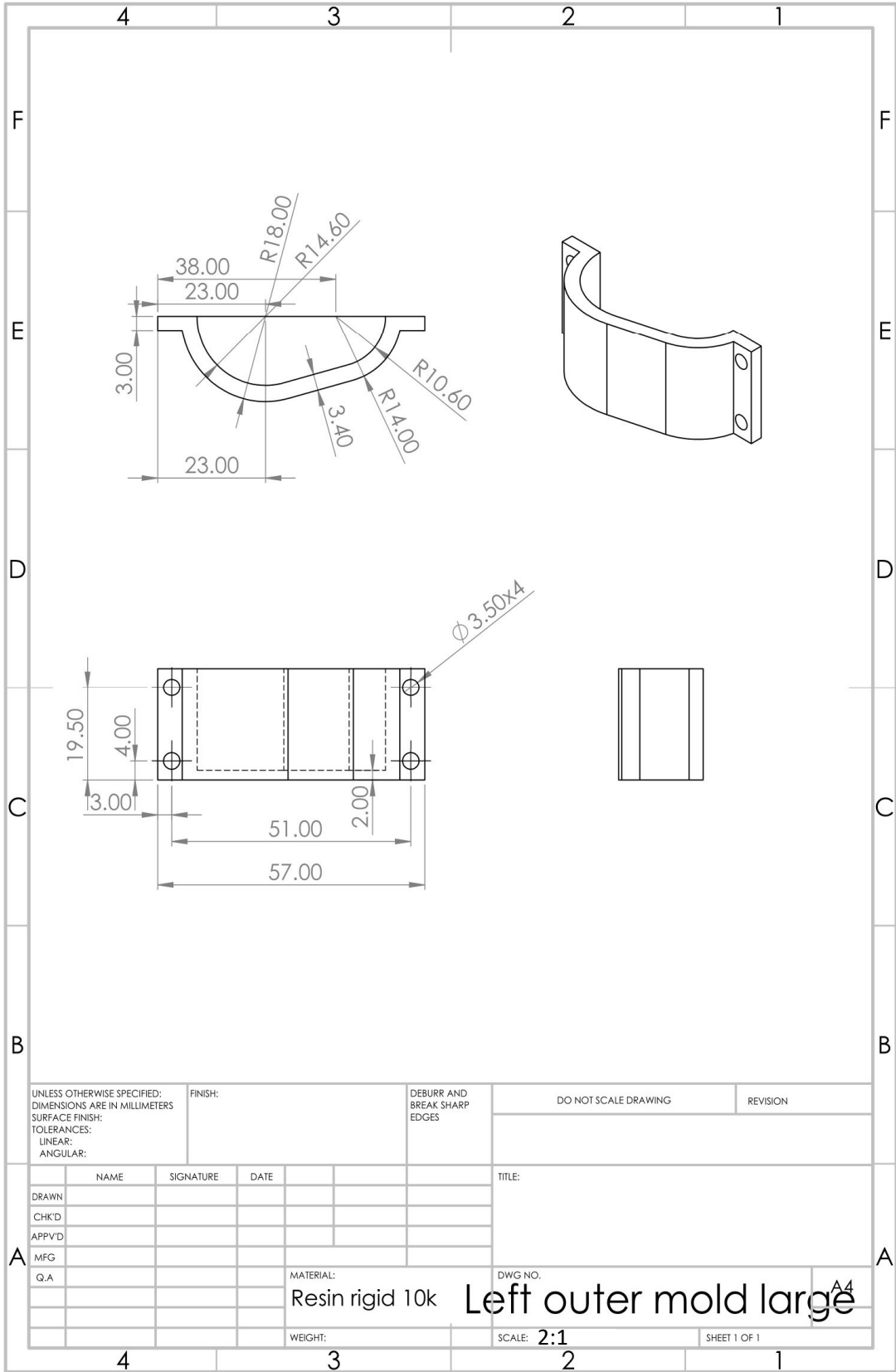
DWG NO.  
**Right outer large** A4

WEIGHT:

SCALE: **2:1**

SHEET 1 OF 1





UNLESS OTHERWISE SPECIFIED:  
 DIMENSIONS ARE IN MILLIMETERS  
 SURFACE FINISH:  
 TOLERANCES:  
 LINEAR:  
 ANGULAR:

FINISH:

DEBURR AND  
 BREAK SHARP  
 EDGES

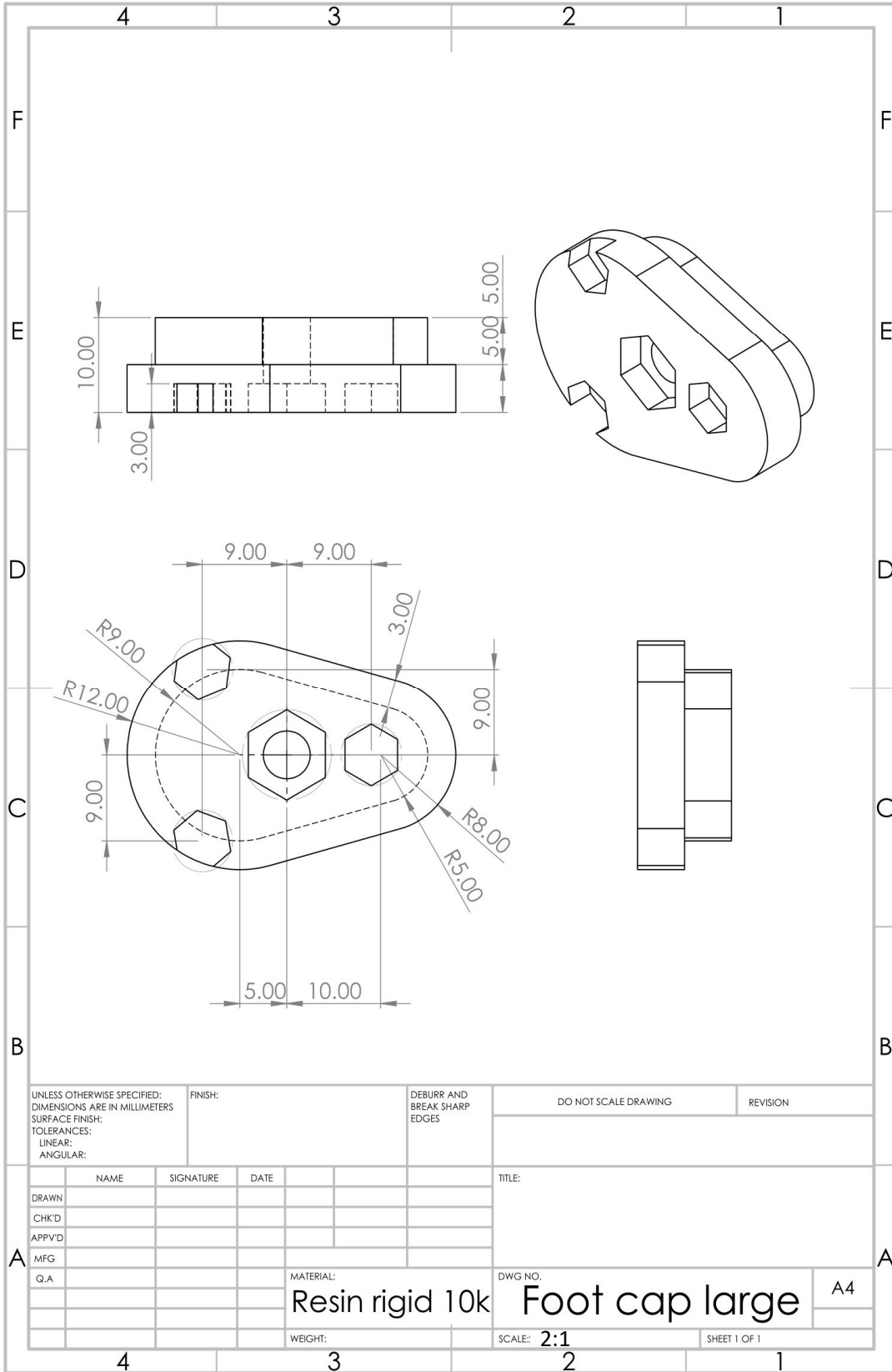
DO NOT SCALE DRAWING

REVISION

	NAME	SIGNATURE	DATE
DRAWN			
CHK'D			
APPV'D			
MFG			
Q.A			

TITLE:	
MATERIAL:	Resin rigid 10k
DWG NO.	Left outer mold large
WEIGHT:	
SCALE:	2:1
SHEET	1 OF 1

A4



UNLESS OTHERWISE SPECIFIED:  
 DIMENSIONS ARE IN MILLIMETERS  
 SURFACE FINISH:  
 TOLERANCES:  
 LINEAR:  
 ANGULAR:

FINISH:

DEBURR AND  
 BREAK SHARP  
 EDGES

DO NOT SCALE DRAWING

REVISION

	NAME	SIGNATURE	DATE
DRAWN			
CHK'D			
APPV'D			
MFG			
Q.A			

TITLE:

MATERIAL:  
**Resin rigid 10k**

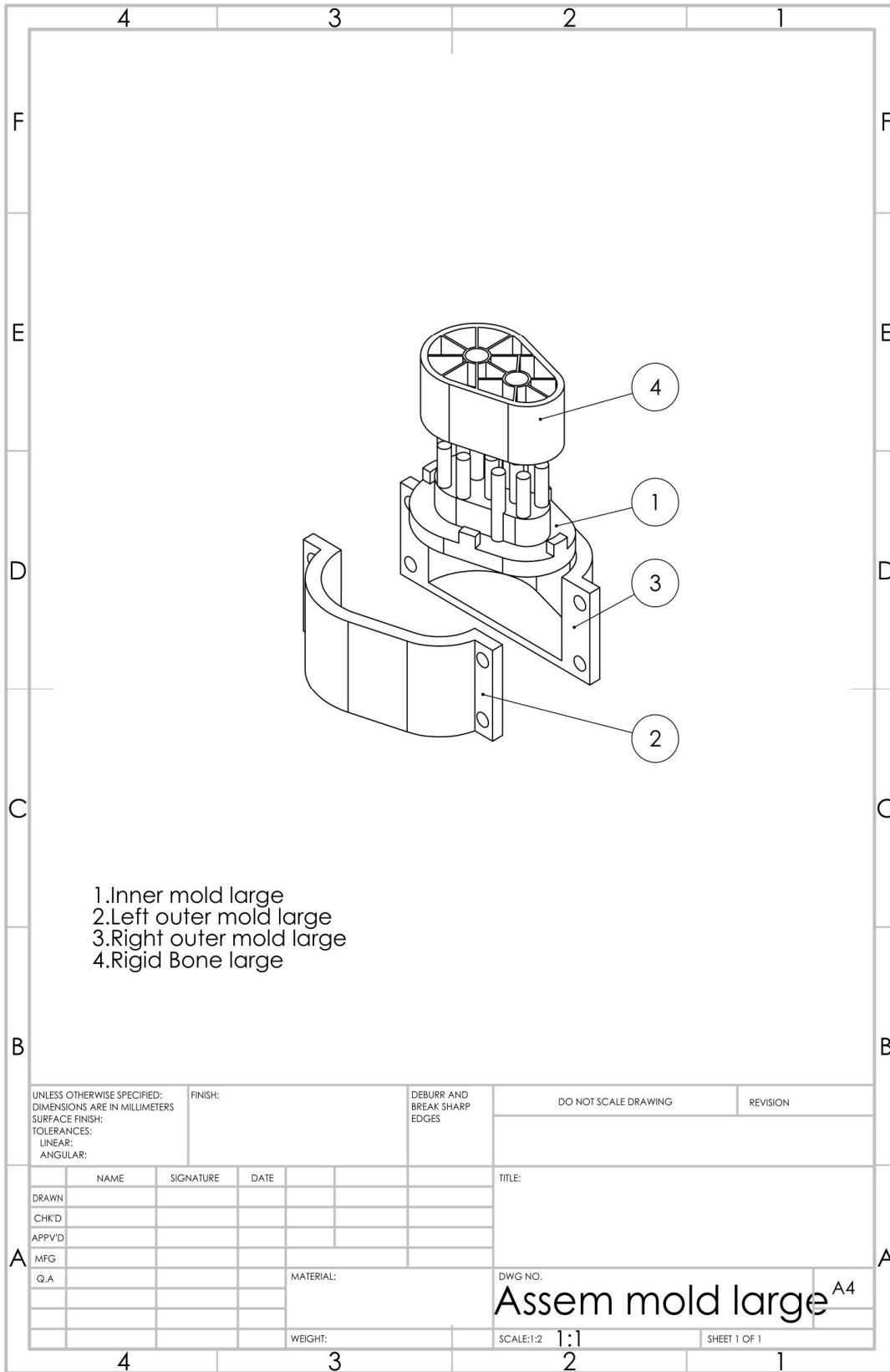
DWG NO.  
**Foot cap large**

A4

WEIGHT:

SCALE: **2:1**

SHEET 1 OF 1



- 1.Inner mold large
- 2.Left outer mold large
- 3.Right outer mold large
- 4.Rigid Bone large

UNLESS OTHERWISE SPECIFIED:  
 DIMENSIONS ARE IN MILLIMETERS  
 SURFACE FINISH:  
 TOLERANCES:  
 LINEAR:  
 ANGULAR:

FINISH:

DEBURR AND  
 BREAK SHARP  
 EDGES

DO NOT SCALE DRAWING

REVISION

	NAME	SIGNATURE	DATE
DRAWN			
CHK'D			
APPV'D			
MFG			
Q.A			

TITLE:

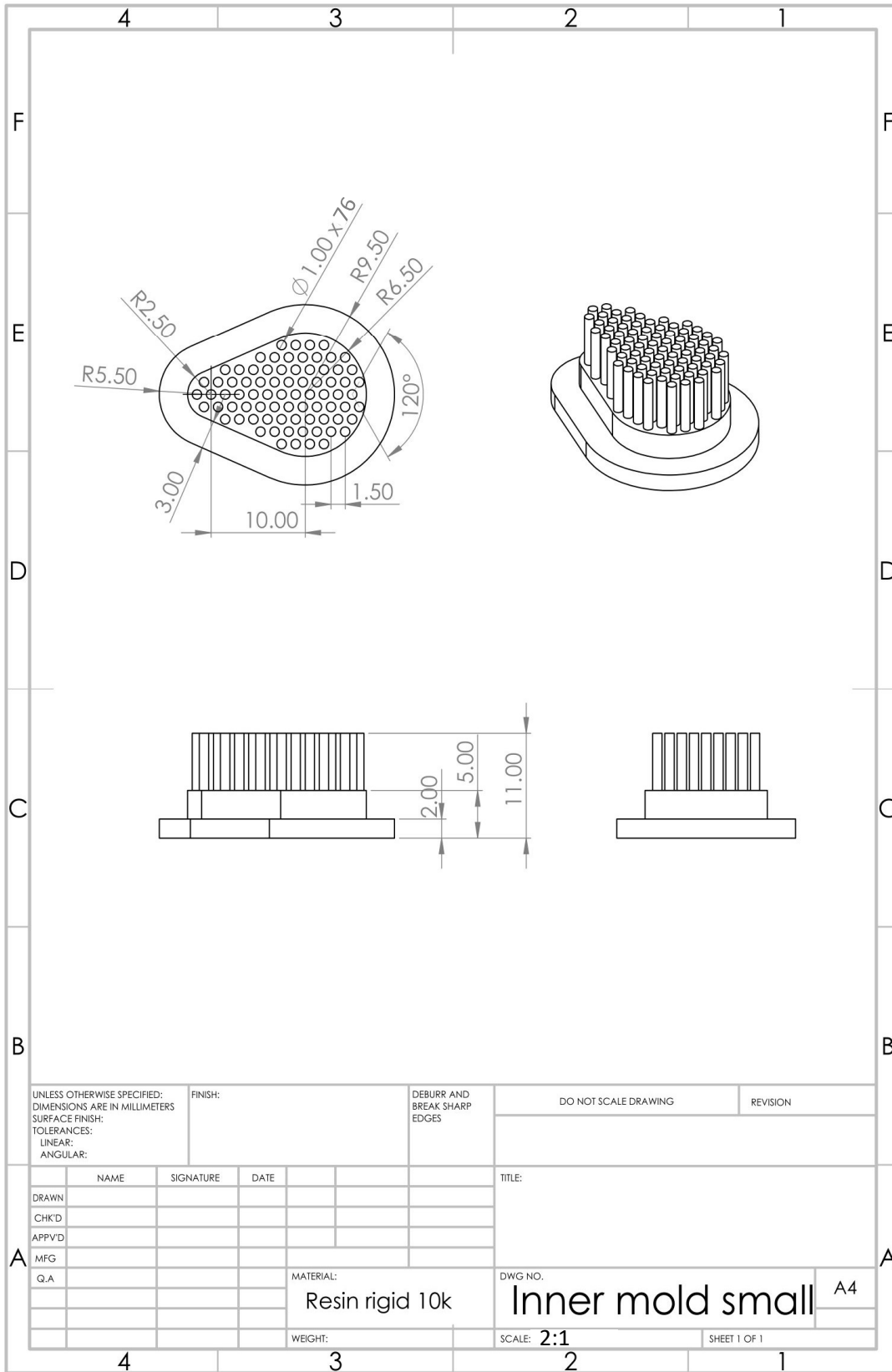
DWG NO. **Assem mold large<sup>A4</sup>**

SCALE: 1:2 | 1:1

WEIGHT:

SHEET 1 OF 1

**7.1.2 Appendix 1.2: Drawing of mold design for small scale foot**



UNLESS OTHERWISE SPECIFIED:  
DIMENSIONS ARE IN MILLIMETERS  
SURFACE FINISH:  
TOLERANCES:  
LINEAR:  
ANGULAR:

FINISH:

DEBURR AND  
BREAK SHARP  
EDGES

DO NOT SCALE DRAWING

REVISION

	NAME	SIGNATURE	DATE		
DRAWN					
CHK'D					
APPV'D					
MFG					
Q.A					

TITLE:

MATERIAL:  
Resin rigid 10k

DWG NO.

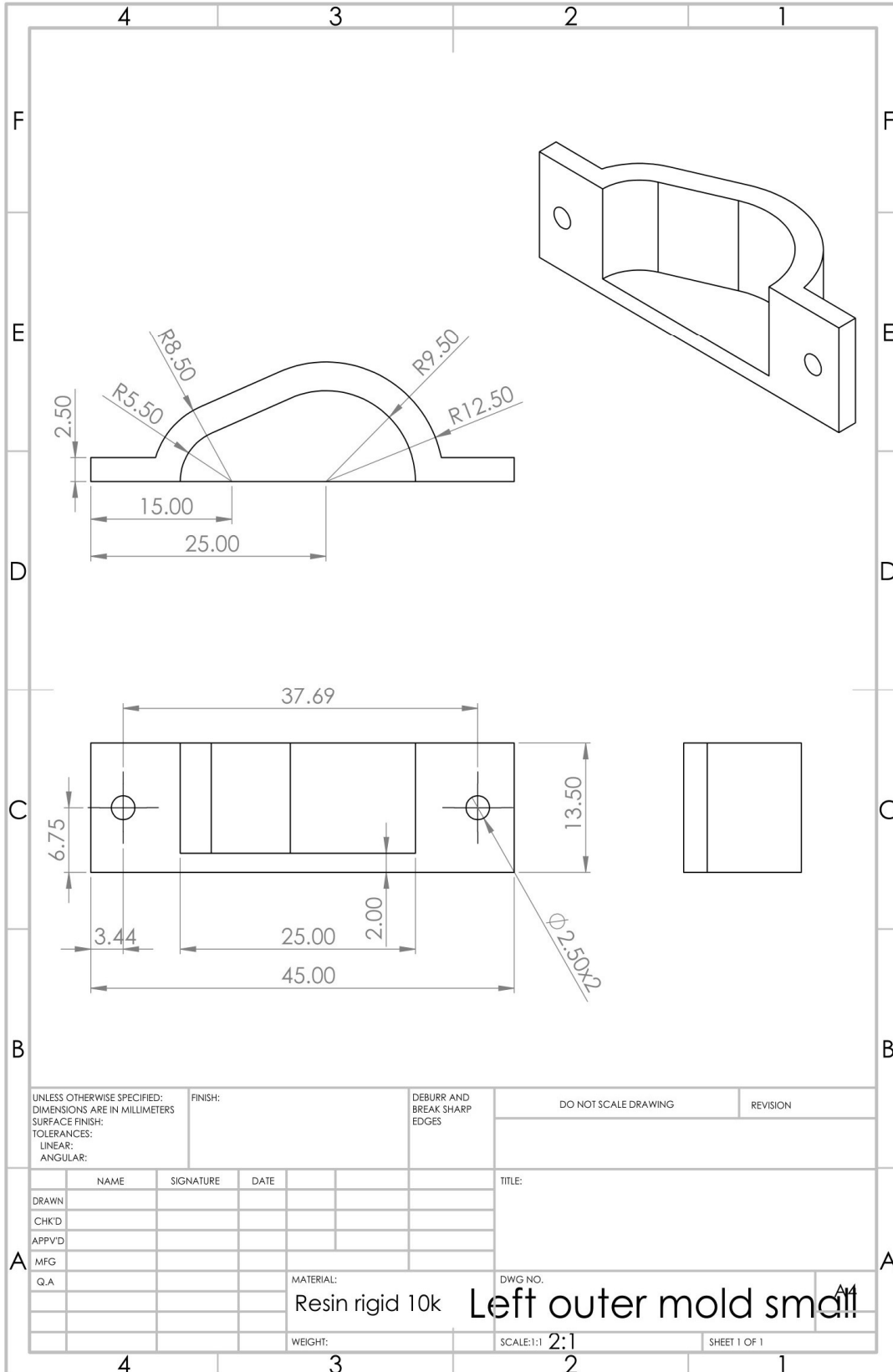
Inner mold small

A4

WEIGHT:

SCALE: 2:1

SHEET 1 OF 1



UNLESS OTHERWISE SPECIFIED:  
 DIMENSIONS ARE IN MILLIMETERS  
 SURFACE FINISH:  
 TOLERANCES:  
 LINEAR:  
 ANGULAR:

FINISH:

DEBURR AND  
 BREAK SHARP  
 EDGES

DO NOT SCALE DRAWING

REVISION

	NAME	SIGNATURE	DATE				
DRAWN							
CHK'D							
APP'VD							
MFG							
Q.A							

TITLE:  
**Left outer mold small**

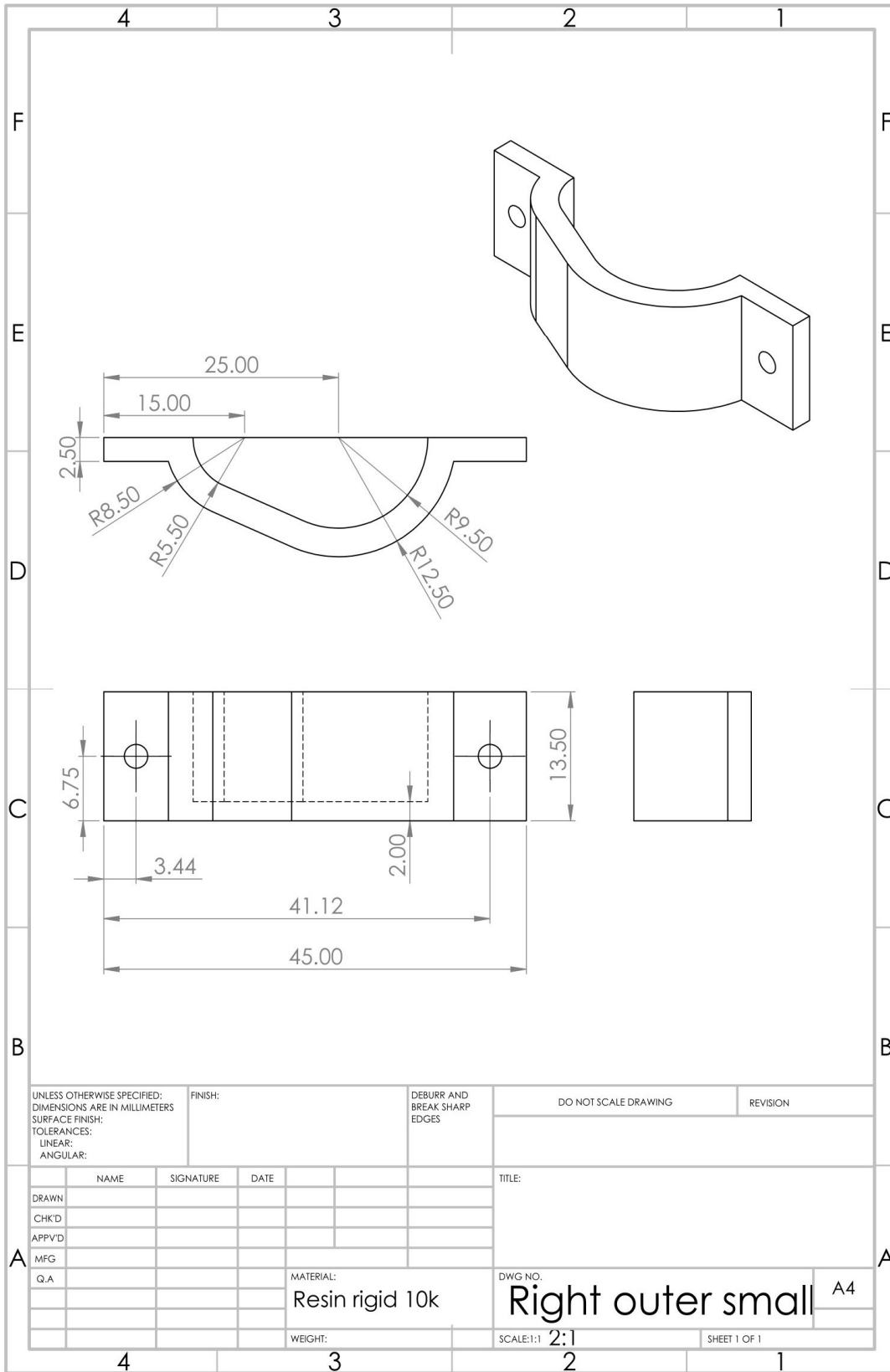
MATERIAL:  
 Resin rigid 10k

DWG NO. **11**

WEIGHT:

SCALE: 1:1 **2:1**

SHEET 1 OF 1



UNLESS OTHERWISE SPECIFIED:  
 DIMENSIONS ARE IN MILLIMETERS  
 SURFACE FINISH:  
 TOLERANCES:  
 LINEAR:  
 ANGULAR:

FINISH:

DEBURR AND  
 BREAK SHARP  
 EDGES

DO NOT SCALE DRAWING

REVISION

	NAME	SIGNATURE	DATE
DRAWN			
CHK'D			
APPV'D			
MFG			
Q.A			

TITLE:

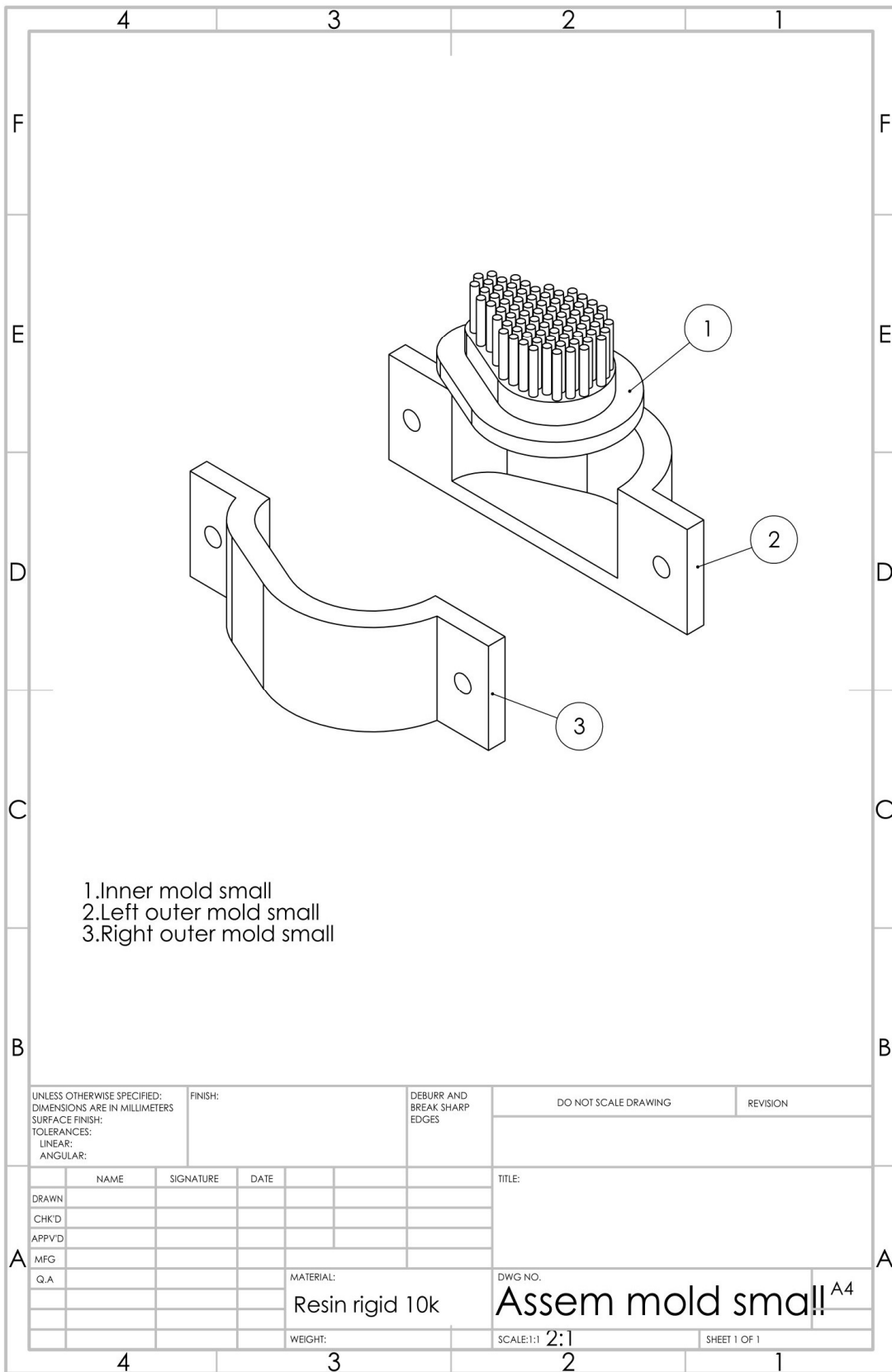
MATERIAL:  
 Resin rigid 10k

DWG NO.  
 Right outer small A4

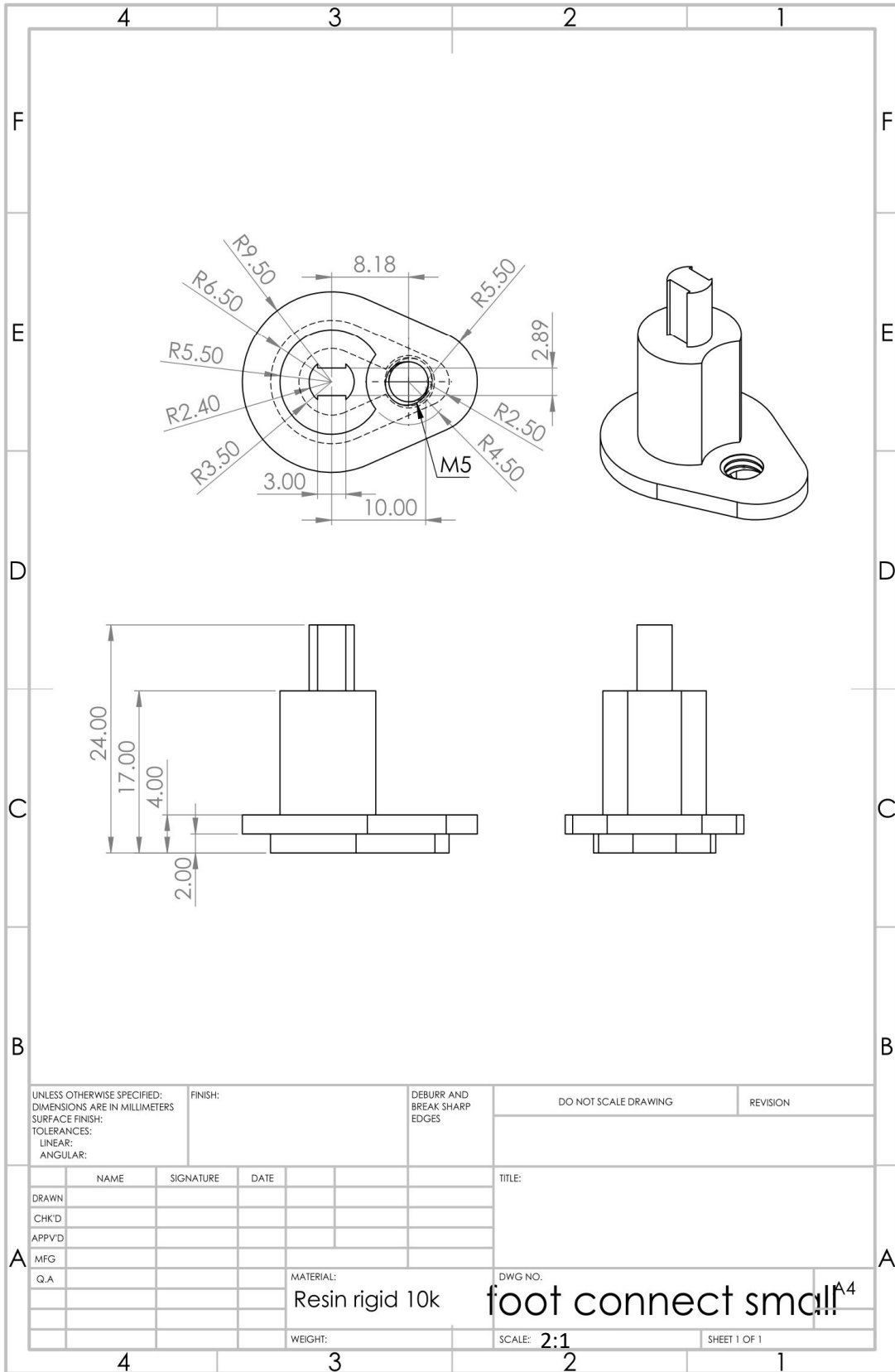
WEIGHT:

SCALE:1:1 2:1

SHEET 1 OF 1







UNLESS OTHERWISE SPECIFIED:  
 DIMENSIONS ARE IN MILLIMETERS  
 SURFACE FINISH:  
 TOLERANCES:  
 LINEAR:  
 ANGULAR:

FINISH:

DEBURR AND  
 BREAK SHARP  
 EDGES

DO NOT SCALE DRAWING

REVISION

	NAME	SIGNATURE	DATE
DRAWN			
CHK'D			
APP'VD			
MFG			
Q.A			

TITLE:	
DWG. NO.	foot connect small <sup>A4</sup>
SCALE:	2:1
SHEET 1 OF 1	

MATERIAL:  
 Resin rigid 10k

WEIGHT:

SCALE: 2:1

SHEET 1 OF 1

## 7.2 Appendix 2: Matlab code for calculation

This section presents the Matlab code used to simulate the analytical model in Chapter 3. Appendix 2.1 is employed for simulating morphology changes without applied pressing force, while Appendix 2.2 simulates morphology changes with applied pressing force. The simulation results are depicted in Fig. 14 and Fig. 16.

### 7.2.1 Morphology changing without pressing force

```
clear all
r0=0.0015;
p=5.5*10^4;
k=40;
syms f(c)
f(c) = (p*(r0^2+c^2)/(2*c))-(2*k*(1.5*sqrt(r0^2+c^2)-r0)/r0);
sol = vpasolve(f)
R=((r0^2+sol^2)/(2*sol))
c=sol;
radius = ((r0^2+c^2)/(2*c));
circr = @(radius,rad_ang) [radius*cos(rad_ang);
    radius*sin(rad_ang)+sqrt(radius^2-r0^2)];
r_angl = linspace(pi/2+acos((c-radius)/radius),
    2*pi+asin((c-radius)/radius));
xy_r = circr(radius,r_angl);
c_ex=0.00125;
radius_ex = (r0^2+c_ex^2)/(2*c_ex)
r_anglex = linspace(pi/2+acos((c_ex-radius_ex)/radius_ex),
    2*pi+asin((c_ex-radius_ex)/radius_ex));
xy_rex = circr(radius_ex,r_anglex);
v = VideoWriter('sphere.avi');
v.FrameRate = 10;
```

```

open(v);
figure(1)
pause(10);
plot([-r0 r0],[0 0], 'LineWidth',2)
axis([-1.5*r0 1.5*r0 0 1.5*r0])
axis equal
xlabel('X axis (mm)')
ylabel('Z axis (mm)')
set(gca, 'FontSize',30)
hold on
pause(3);
frame = getframe(gcf);
writeVideo(v,frame);
figure(1)
plot(xy_r(1,:), xy_r(2,:), 'Color','r', 'LineWidth',2)
plot(xy_rex(1,:), xy_rex(2,:), 'Color','r', 'LineWidth',2, 'LineStyle','--')
axis([-1.5*r0 1.5*r0 0 1.5*r0])
axis equal
xlabel('X axis (mm)')
ylabel('Z axis (mm)')
set(gca, 'FontSize',30)
hold on
pause(3);
frame = getframe(gcf);
    writeVideo(v,frame);
p=6.5*10^4;
syms f(c)
f(c) = (p*(r0^2+c^2)/(2*c))-(2*k*(1.5*sqrt(r0^2+c^2)-r0)/r0);
sol = vpasolve(f)
R=(r0^2+sol^2)/(2*sol)

```

```

c=sol;
radius = (r0^2+c^2)/(2*c);
circr = @(radius,rad_ang) [radius*cos(rad_ang);
    radius*sin(rad_ang)-sqrt(radius^2-r0^2)];
r_angl = linspace(pi/2+acos((c-radius)/radius),
    2*pi+asin((c-radius)/radius));
xy_r = circr(radius,r_angl);
c_ex=0.0016;
radius_ex = (r0^2+c_ex^2)/(2*c_ex);
r_anglex = linspace(pi/2+acos((c_ex-radius_ex)/radius_ex),
    2*pi+asin((c_ex-radius_ex)/radius_ex));
xy_rex = circr(radius_ex,r_anglex);
figure(1)
plot(xy_r(1,:), xy_r(2,:), 'Color','g','LineWidth',2)
plot(xy_rex(1,:),xy_rex(2,:), 'Color','g','LineWidth',2,'LineStyle','--')
axis([-1.5*r0 1.5*r0 0 1.5*r0])
axis equal
xlabel('X axis (mm)')
ylabel('Z axis (mm)')
set(gca,'FontSize',30)
hold on
pause(3);
frame = getframe(gcf);
writeVideo(v,frame);
p=7.5*10^4;
syms f(c)
f(c) = (p*(r0^2+c^2)/(2*c))-(2*k*(1.5*sqrt(r0^2+c^2)-r0)/r0);
sol = vpasolve(f)
R=(r0^2+sol^2)/(2*sol)
c=sol;

```

```

radius = (r0^2+c^2)/(2*c);
circr = @(radius,rad_ang) [radius*cos(rad_ang);
    radius*sin(rad_ang)-sqrt(radius^2-r0^2)];
r_angl = linspace(pi/2+acos((c-radius)/radius),
    2*pi+asin((c-radius)/radius));
xy_r = circr(radius,r_angl);
c_ex=0.002;
radius_ex = (r0^2+c_ex^2)/(2*c_ex);
r_anglex = linspace(pi/2+acos((c_ex-radius_ex)/radius_ex),
    2*pi+asin((c_ex-radius_ex)/radius_ex));
xy_rex = circr(radius_ex,r_anglex);
figure(1)
plot(xy_r(1,:), xy_r(2,:), 'Color', 'b', 'LineWidth', 2)
plot(xy_rex(1,:), xy_rex(2,:), 'Color', 'b', 'LineWidth', 2, 'LineStyle', '--')
axis([-1.5*r0 1.5*r0 0 1.5*r0])
axis equal
xlabel('X axis (mm)')
ylabel('Z axis (mm)')
set(gca, 'FontSize', 30)
hold on
pause(3);
frame = getframe(gcf);
writeVideo(v,frame);
p=8.5*10^4;
syms f(c)
f(c) = (p*(r0^2+c^2)/(2*c))-(2*k*(1.5*sqrt(r0^2+c^2)-r0)/r0);
sol = vpasolve(f)
R=(r0^2+sol^2)/(2*sol)
c=sol;
radius = (r0^2+c^2)/(2*c);

```

```

circr = @(radius,rad_ang) [radius*cos(rad_ang);
    radius*sin(rad_ang)-sqrt(radius^2-r0^2)];
r_angl = linspace(pi/2+acos((c-radius)/radius),
    2*pi+asin((c-radius)/radius));
xy_r = circr(radius,r_angl);
c_ex=0.0024;
radius_ex = (r0^2+c_ex^2)/(2*c_ex);
r_anglex = linspace(pi/2+acos((c_ex-radius_ex)/radius_ex),
    2*pi+asin((c_ex-radius_ex)/radius_ex));
xy_rex = circr(radius_ex,r_anglex);
figure(1)
plot(xy_r(1,:), xy_r(2,:), 'Color','k','LineWidth',2)
plot(xy_rex(1,:), xy_rex(2,:), 'Color','k','LineWidth',2,'LineStyle','--')
axis([-1.5*r0 1.5*r0 0 1.5*r0])
axis equal
legend({'$p=0$', '$p=55kpa$', '$p=65kpa$', '$p=75kpa$', '$p=85kpa$'},
    'Interpreter','latex','FontSize',23)
xlabel('X axis (mm)')
ylabel('Z axis (mm)')
set(gca,'FontSize',30)
hold off
pause(3);
frame = getframe(gcf);
writeVideo(v,frame);
close(v);

```

### 7.2.2 Morphology changing with pressing force

```

syms a c2
fo=0.08;
p=7.5*10^4;

```

```

pi=3.1415;
E=29.5*10^3;
pois=0.5;
E1=E/(1-pois^2);
ga=0.006;
ga_s=0.0027;
ga_l=0.0073;
theta=1.35;
r0=0.0015;
c1=0.0019412681941617884192468215394673;
k=40;
eq1 = (r0^2+c2^2)/(2*c2)-sqrt(((r0^2+c2^2)/(2*c2))^2
    -(fo+2*ga*pi*((r0^2+c2^2)/(2*c2)))/(p*pi))==a;
eq2 = fo==p*(pi/2)*((fo+2*ga*pi*((r0^2+c2^2)/(2*c2)))/(p*pi)+a^2+r0^2+c2^2
    -2*k*pi*(c2+a)*(1.5*sqrt(r0^2+c2^2-a^2)-r0)/r0;
[sol_a, sol_c2]= vpasolve([eq1,eq2], [a c2]);
b=sqrt((fo+2*ga*pi*((r0^2+sol_c2^2)/(2*sol_c2)))/(p*pi))
a_2=sol_a;
c_2=sol_c2;
R1=(r0^2+c1^2)/(2*c1);
R2=(r0^2+c_2^2)/(2*c_2);
phi=asin(b/R2)
cap=2*ga_l*(2*b+(2*cot(phi)+1)*sqrt((3*ga_s*sin(phi+theta))/(9810*cot(phi))))
circr = @(R1,rad_ang) [R1*cos(rad_ang); R1*sin(rad_ang)-sqrt(R1^2-r0^2)];
r_angl = linspace(pi/2+acos((c1-R1)/R1), 2*pi+asin((c1-R1)/R1));
xy_r = circr(R1,r_angl);
if c_2>R2
    circr2 = @(R2,rad_ang) [R2*cos(rad_ang); R2*sin(rad_ang)-sqrt(R2^2-r0^2)];
else
    circr2 = @(R2,rad_ang) [R2*cos(rad_ang); R2*sin(rad_ang)+sqrt(R2^2-r0^2)];

```

```

end

c_ex=0.002;

radius_ex = (r0^2+c_ex^2)/(2*c_ex);

r_anglex = linspace(pi/2+acos((c_ex-radius_ex)/radius_ex),
                    2*pi+asin((c_ex-radius_ex)/radius_ex));

xy_rex = circr(radius_ex,r_anglex);

r_angl2a = linspace(pi/2+acos((c_2-R2)/R2), pi/2+acos((a_2-R2)/R2));
r_angl2b = linspace(2*pi+asin((a_2-R2)/R2), 2*pi+asin((c_2-R2)/R2));

xy_r2a = circr2(R2,r_angl2a);
xy_r2b = circr2(R2,r_angl2b);

c_ex=0.0018;

radius_ex = (r0^2+c_ex^2)/(2*c_ex);

a_ex=0.000084434;

b_ex=0.0005;

r_angl2a_ex = linspace(pi/2+acos((c_ex-radius_ex)/radius_ex),
                      pi/2+acos((a_ex-radius_ex)/radius_ex));
r_angl2b_ex = linspace(2*pi+asin((a_ex-radius_ex)/radius_ex),
                      2*pi+asin((c_ex-radius_ex)/radius_ex));

xy_r2a_ex = circr2(radius_ex,r_angl2a_ex);
xy_r2b_ex = circr2(radius_ex,r_angl2b_ex);

v = VideoWriter('sphere under contact.avi');

v.FrameRate = 10;

open(v);

figure(1)

pause(10);

plot(xy_r(1,:), xy_r(2,:), 'LineWidth',2)

axis([-1.5*r0  1.5*r0    0  1.5*r0])

hold on

plot(xy_rex(1,:), xy_rex(2,:), 'Color', 'b', 'LineWidth',2, 'LineStyle', '--')

axis([-1.5*r0  1.5*r0    0  1.5*r0])

```



```

axis equal
xlabel('X axis (mm)')
ylabel('Z axis (mm)')
set(gca,'FontSize',30)
hold on
pause(3);
frame = getframe(gcf);
writeVideo(v,frame);
figure(1)
plot(xy_r2a(1,:), xy_r2a(2,:), 'Color','r','LineWidth',2)
plot(xy_r2b(1,:), xy_r2b(2,:), 'Color','r','LineWidth',2)
axis([-1.5*r0 1.5*r0 0 1.5*r0])
line([-b b],[a_2-c_2 a_2-c_2], 'Color','r','LineWidth',2)
plot(xy_r2a_ex(1,:), xy_r2a_ex(2,:),
      'Color','r','LineWidth',2,'LineStyle','--')
plot(xy_r2b_ex(1,:), xy_r2b_ex(2,:),
      'Color','r','LineWidth',2,'LineStyle','--')
line([-b_ex b_ex],[a_ex-c_ex a_ex-c_ex],
      'Color','r','LineWidth',2,'LineStyle','--')
axis equal
xlabel('X axis (mm)')
ylabel('Z axis (mm)')
set(gca,'FontSize',30)
hold on
pause(3);
frame = getframe(gcf);
writeVideo(v,frame);
fo=0.19;
eq1 = (r0^2+c2^2)/(2*c2)-sqrt(((r0^2+c2^2)/(2*c2))^2
      -(fo+2*ga*pi*((r0^2+c2^2)/(2*c2)))/(p*pi))==a;

```

```

eq2 = fo==p*(pi/2)*((fo+2*ga*pi*((r0^2+c2^2)/(2*c2)))/(p*pi)+a^2+r0^2+c2^2)
      -2*k*pi*(c2+a)*(1.5*sqrt(r0^2+c2^2-a^2)-r0)/r0;
[sol_a, sol_c2]= vpasolve([eq1,eq2], [a c2]);
b=sqrt((fo+2*ga*pi*((r0^2+sol_c2^2)/(2*sol_c2)))/(p*pi))
a_2=sol_a;
c_2=sol_c2;
R2=(r0^2+c_2^2)/(2*c_2);
phi=asin(b/R2)
cap=2*ga_l*(2*b+(2*cot(phi)+1)*sqrt((3*ga_s*sin(phi+theta))/(9810*cot(phi))))
if c_2>R2
    circr2 = @(R2,rad_ang) [R2*cos(rad_ang); R2*sin(rad_ang)-sqrt(R2^2-r0^2)];
else
    circr2 = @(R2,rad_ang) [R2*cos(rad_ang); R2*sin(rad_ang)+sqrt(R2^2-r0^2)];
end
r_angl2a = linspace(pi/2+acos((c_2-R2)/R2), pi/2+acos((a_2-R2)/R2));
r_angl2b = linspace(2*pi+asin((a_2-R2)/R2), 2*pi+asin((c_2-R2)/R2));
xy_r2a = circr2(R2,r_angl2a);
xy_r2b = circr2(R2,r_angl2b);
c_ex=0.0014;
radius_ex = (r0^2+c_ex^2)/(2*c_ex);
a_ex=0.00036217;
b_ex=0.00098;
r_angl2a_ex = linspace(pi/2+acos((c_ex-radius_ex)/radius_ex),
                        pi/2+acos((a_ex-radius_ex)/radius_ex));
r_angl2b_ex = linspace(2*pi+asin((a_ex-radius_ex)/radius_ex),
                        2*pi+asin((c_ex-radius_ex)/radius_ex));
xy_r2a_ex = circr2(radius_ex,r_angl2a_ex);
xy_r2b_ex = circr2(radius_ex,r_angl2b_ex);
figure(1)
plot(xy_r2a(1,:), xy_r2a(2,:), 'Color', 'g', 'LineWidth', 2)

```

```

plot(xy_r2b(1,:), xy_r2b(2,:), 'Color', 'g', 'LineWidth', 2)
axis([-1.5*r0 1.5*r0 0 1.5*r0])
line([-b b], [(a_2-c_2) (a_2-c_2)], 'Color', 'g', 'LineWidth', 2)
plot(xy_r2a_ex(1,:), xy_r2a_ex(2,:),
      'Color', 'g', 'LineWidth', 2, 'LineStyle', '--')
plot(xy_r2b_ex(1,:), xy_r2b_ex(2,:),
      'Color', 'g', 'LineWidth', 2, 'LineStyle', '--')
line([-b_ex b_ex], [(a_ex-c_ex) (a_ex-c_ex)],
      'Color', 'g', 'LineWidth', 2, 'LineStyle', '--')
axis equal
xlabel('X axis (mm)')
ylabel('Z axis (mm)')
set(gca, 'FontSize', 30)
hold on
pause(3);
frame = getframe(gcf);
writeVideo(v, frame);
fo=0.285;
eq1 = (r0^2+c^2)/(2*c2)-sqrt(((r0^2+c2^2)/(2*c2))^2
      -(fo+2*ga*pi*((r0^2+c2^2)/(2*c2)))/(p*pi))==a;
eq2 = fo==p*(pi/2)*((fo+2*ga*pi*((r0^2+c2^2)/(2*c2)))/(p*pi)+a^2+r0^2+c2^2
      -2*k*pi*(c2+a)*(1.5*sqrt(r0^2+c2^2-a^2)-r0)/r0;
[sol_a, sol_c2]= vpasolve([eq1,eq2], [a c2]);
b=sqrt((fo+2*ga*pi*((r0^2+sol_c2^2)/(2*sol_c2)))/(p*pi))
a_2=sol_a;
c_2=sol_c2;
R2=(r0^2+c_2^2)/(2*c_2);
phi=asin(b/R2)
cap=2*ga_l*(2*b+(2*cot(phi)+1)*sqrt((3*ga_s*sin(phi+theta))/(9810*cot(phi))))
if c_2>R2

```

```

    circr2 = @(R2,rad_ang) [R2*cos(rad_ang); R2*sin(rad_ang)-sqrt(R2^2-r0^2)];
else
    circr2 = @(R2,rad_ang) [R2*cos(rad_ang); R2*sin(rad_ang)+sqrt(R2^2-r0^2)];
end
r_angl2a = linspace(pi/2+acos((c_2-R2)/R2), pi/2+acos((a_2-R2)/R2));
r_angl2b = linspace(2*pi+asin((a_2-R2)/R2), 2*pi+asin((c_2-R2)/R2));
xy_r2a = circr2(R2,r_angl2a);
xy_r2b = circr2(R2,r_angl2b);
c_ex=0.001;
radius_ex = (r0^2+c_ex^2)/(2*c_ex);
a_ex=0.0004368;
b_ex=0.0011;
r_angl2a_ex = linspace(pi/2+acos((c_ex-radius_ex)/radius_ex),
    pi/2+acos((a_ex-radius_ex)/radius_ex));
r_angl2b_ex = linspace(2*pi+asin((a_ex-radius_ex)/radius_ex),
    2*pi+asin((c_ex-radius_ex)/radius_ex));
xy_r2a_ex = circr2(radius_ex,r_angl2a_ex);
xy_r2b_ex = circr2(radius_ex,r_angl2b_ex);
figure(1)
plot(xy_r2a(1,:), xy_r2a(2,:), 'Color','k', 'LineWidth',2)
plot(xy_r2b(1,:), xy_r2b(2,:), 'Color','k', 'LineWidth',2)
axis([-1.5*r0 1.5*r0 0 1.5*r0])
line([-b b],[a_2-c_2 a_2-c_2], 'Color','k', 'LineWidth',2)
plot(xy_r2a_ex(1,:), xy_r2a_ex(2,:),
    'Color','k', 'LineWidth',2, 'LineStyle','--')
plot(xy_r2b_ex(1,:), xy_r2b_ex(2,:),
    'Color','k', 'LineWidth',2, 'LineStyle','--')
line([-b_ex b_ex],[a_ex-c_ex a_ex-c_ex],
    'Color','k', 'LineWidth',2, 'LineStyle','--')
axis equal

```

```
xlabel('X axis (mm)')
ylabel('Z axis (mm)')
set(gca,'FontSize',30)
hold off
pause(3);
frame = getframe(gcf);
writeVideo(v,frame);
close(v);
```

# Bibliography

- [1] Jangsun Hwang, Yoon Jeong, Jeong Min Park, et al. “Biomimetics: forecasting the future of science, engineering, and medicine”. In: *International journal of nanomedicine* 10 (2015), p. 5701.
- [2] Sangbae Kim, Cecilia Laschi, and Barry Trimmer. “Soft robotics: a bioinspired evolution in robotics”. In: *Trends in biotechnology* 31.5 (2013), pp. 287–294.
- [3] Julius E. Bernth, Van Anh Ho, and Hongbin Liu. “Morphological computation in haptic sensation and interaction: from nature to robotics”. In: *Advanced Robotics* 32.7 (2018), pp. 340–362.
- [4] Vincent C Müller and Matej Hoffmann. “What is morphological computation? On how the body contributes to cognition and control”. In: *Artificial life* 23.1 (2017), pp. 1–24.
- [5] Saranshu Singla, Dharamdeep Jain, Chelsea M Zoltowski, et al. “Direct evidence of acid-base interactions in gecko adhesion”. In: *Science Advances* 7.21 (2021), eabd9410.
- [6] Fandong Meng, Quan Liu, Xin Wang, et al. “Tree frog adhesion biomimetics: opportunities for the development of new, smart adhesives that adhere under wet conditions”. In: *Philosophical Transactions of the Royal Society A* 377.2150 (2019), p. 20190131.
- [7] Rolf Pfeifer, Max Lungarella, and Fumiya Iida. “Self-organization, embodiment, and biologically inspired robotics”. In: *science* 318.5853 (2007), pp. 1088–1093.
- [8] Robert D Prusch. “Solute secretion by the tube foot epithelium in the starfish *Asterias forbesi*”. In: *Journal of Experimental Biology* 68.1 (1977), pp. 35–43.

- [9] Morgane Algrain, Elise Hennebert, Philip Bertemes, et al. "In the footsteps of sea stars: deciphering the catalogue of proteins involved in underwater temporary adhesion". In: *Open Biology* 12.8 (2022), p. 220103.
- [10] Bin Han, Haoyuan Yi, Zhenyu Xu, et al. "3D-SLIP model based dynamic stability strategy for legged robots with impact disturbance rejection". In: *Scientific Reports* 12.1 (2022), p. 5892.
- [11] Iain DC Hill, Benzhenq Dong, W Jon P Barnes, et al. "The biomechanics of tree frogs climbing curved surfaces: a gripping problem". In: *Journal of Experimental Biology* 221.5 (2018), jeb168179.
- [12] B Kollbe Ahn. "Perspectives on mussel-inspired wet adhesion". In: *Journal of the American Chemical Society* 139.30 (2017), pp. 10166–10171.
- [13] Minsu Kang, Kahyun Sun, Minho Seong, et al. "Applications of bioinspired reversible dry and wet adhesives: A review". In: *Frontiers in Mechanical Engineering* 7 (2021), p. 668262.
- [14] Ji-Peng Wang, Elena Gallo, Bertrand François, et al. "Capillary force and rupture of funicular liquid bridges between three spherical bodies". In: *Powder Technology* 305 (2017), pp. 89–98.
- [15] Fabio Gabrieli, Pierre Lambert, Simonetta Cola, et al. "Micromechanical modelling of erosion due to evaporation in a partially wet granular slope". In: *International journal for numerical and analytical methods in geomechanics* 36.7 (2012), pp. 918–943.
- [16] Hyeongho Min, Sangyul Baik, Jihyun Lee, et al. "Enhanced biocompatibility and multidirectional wet adhesion of insect-like synergistic wrinkled pillars with microcavities". In: *Chemical Engineering Journal* 429 (2022), p. 132467.
- [17] Gavin Hanna, W Jon, and WP Jon Barnes. "Adhesion and detachment of the toe pads of tree frogs". In: *Journal of Experimental Biology* 155.1 (1991), pp. 103–125.

- [18] Julian KA Langowski, Dimitra Dodou, Marleen Kamperman, et al. "Tree frog attachment: mechanisms, challenges, and perspectives". In: *Frontiers in zoology* 15.1 (2018), pp. 1–21.
- [19] Kellar Autumn. "How gecko toes stick: the powerful fantastic adhesive used by geckos is made of nanoscale hairs that engage tiny forces, inspiring envy among human imitators". In: *American scientist* 94.2 (2006), pp. 124–133.
- [20] Jing Yu, Sathya Chary, Saurabh Das, et al. "Gecko-inspired dry adhesive for robotic applications". In: *Advanced Functional Materials* 21.16 (2011), pp. 3010–3018.
- [21] Gerrit Huber, Hubert Mantz, Ralph Spolenak, et al. "Evidence for capillarity contributions to gecko adhesion from single spatula nanomechanical measurements". In: *Proceedings of the National Academy of Sciences* 102.45 (2005), pp. 16293–16296.
- [22] Romana Santos, Stanislav Gorb, Valérie Jamar, et al. "Adhesion of echinoderm tube feet to rough surfaces". In: *Journal of Experimental Biology* 208.13 (2005), pp. 2555–2567.
- [23] Julian KA Langowski, Dimitra Dodou, Peter van Assenbergh, et al. "Design of tree-frog-inspired adhesives". In: *Integrative and comparative biology* 60.4 (2020), pp. 906–918.
- [24] Michael A Bell, Isabella Pestovski, William Scott, et al. "Echinoderm-inspired tube feet for robust robot locomotion and adhesion". In: *IEEE Robotics and Automation Letters* 3.3 (2018), pp. 2222–2228.
- [25] Aihong Ji, Zhihui Zhao, Poramate Manoonpong, et al. "A bio-inspired climbing robot with flexible pads and claws". In: *Journal of Bionic Engineering* 15.2 (2018), pp. 368–378.
- [26] Yufeng Chen, Neel Doshi, and Robert J Wood. "Inverted and inclined climbing using capillary adhesion in a quadrupedal insect-scale robot". In: *IEEE Robotics and Automation Letters* 5.3 (2020), pp. 4820–4827.



- [27] Kenneth Langstreth Johnson, Kevin Kendall, and aAD Roberts. "Surface energy and the contact of elastic solids". In: *Proceedings of the royal society of London. A. mathematical and physical sciences* 324.1558 (1971), pp. 301–313.
- [28] Boris V Derjaguin, Vladimir M Muller, and Yu P Toporov. "Effect of contact deformations on the adhesion of particles". In: *Journal of Colloid and interface science* 53.2 (1975), pp. 314–326.
- [29] KNG Fuller and David Tabor. "The effect of surface roughness on the adhesion of elastic solids". In: *Proceedings of the Royal Society of London. A. Mathematical and Physical Sciences* 345.1642 (1975), pp. 327–342.
- [30] Daniel Maugis. "Adhesion of spheres: the JKR-DMT transition using a Dugdale model". In: *Journal of colloid and interface science* 150.1 (1992), pp. 243–269.
- [31] Pho Van Nguyen and Van Anh Ho. "Mechanics of wet adhesion in soft interaction with patterned morphology". In: *Bioinspiration & Biomimetics* 14.1 (2018), p. 016005.
- [32] Pho Van Nguyen and Van Anh Ho. "Grasping Interface With Wet Adhesion and Patterned Morphology: Case of Thin Shell". In: *IEEE Robotics and Automation Letters* 4.2 (2019), pp. 792–799. DOI: [10.1109/LRA.2019.2893401](https://doi.org/10.1109/LRA.2019.2893401).
- [33] Pho Van Nguyen and Van Anh Ho. "Wet Adhesion of Soft Curved Interfaces With Micro Pattern". In: *IEEE Robotics and Automation Letters* 6.3 (2021), pp. 4273–4280. DOI: [10.1109/LRA.2021.3067277](https://doi.org/10.1109/LRA.2021.3067277).
- [34] Richard D O'Rorke, Terry WJ Steele, and HK Taylor. "Bioinspired fibrillar adhesives: a review of analytical models and experimental evidence for adhesion enhancement by surface patterns". In: *Journal of Adhesion Science and Technology* 30.4 (2016), pp. 362–391.
- [35] Daisuke Yamada, Takashi Maeno, and Yoji Yamada. "Artificial finger skin having ridges and distributed tactile sensors used for grasp force control". In: *Proceedings 2001 IEEE/RSJ International Conference on Intelligent Robots and Systems. Expanding the Societal Role of Robotics in the the Next Millennium (Cat. No. 01CH37180)*. Vol. 2. IEEE. 2001, pp. 686–691.

- 
- [36] Dirk-Michael Drotlef, Lukas Stepien, Michael Kappl, et al. "Insights into the adhesive mechanisms of tree frogs using artificial mimics". In: *Advanced Functional Materials* 23.9 (2013), pp. 1137–1146.
- [37] Cheng-Hsin Chuang, Yi-Rong Liou, and Chih-Wei Chen. "Detection system of incident slippage and friction coefficient based on a flexible tactile sensor with structural electrodes". In: *Sensors and Actuators A: physical* 188 (2012), pp. 48–55.
- [38] Michael Bloesch, Christian Gehring, Péter Fankhauser, et al. "State estimation for legged robots on unstable and slippery terrain". In: *2013 IEEE/RSJ International Conference on Intelligent Robots and Systems*. IEEE. 2013, pp. 6058–6064.
- [39] Valentin L Popov. *Contact mechanics and friction*. Springer, 2010.
- [40] Ayokunle Olanrewaju, Maiwenn Beaugrand, Mohamed Yafia, et al. "Capillary microfluidics in microchannels: from microfluidic networks to capillary circuits". In: *Lab on a Chip* 18.16 (2018), pp. 2323–2347.
- [41] Ulrich Hornung and Hans D Mittelmann. "A finite element method for capillary surfaces with volume constraints". In: *Journal of computational physics* 87.1 (1990), pp. 126–136.
- [42] Li Luo, Xiao-Ping Wang, and Xiao-Chuan Cai. "An efficient finite element method for simulation of droplet spreading on a topologically rough surface". In: *Journal of Computational Physics* 349 (2017), pp. 233–252.
- [43] SASHIKUMAAR Ganesan and LUTZ Tobiska. "Finite element simulation of a droplet impinging a horizontal surface". In: *Proceedings of ALGORITMY*. Vol. 2005. 2005, pp. 1–11.
- [44] Raffaele Ardito, Alberto Corigliano, and Attilio Frangi. "Multiscale finite-element models for predicting spontaneous adhesion in MEMS". In: *Mechanics & Industry* 11.3-4 (2010), pp. 177–182.

- [45] Hiroyuki Minaki and Shaofan Li. "Multiscale modeling and simulation of dynamic wetting". In: *Computer Methods in Applied Mechanics and Engineering* 273 (2014), pp. 273–302.
- [46] Bjorn Van Belleghem, R Montoya, J Dewanckele, et al. "Capillary water absorption in cracked and uncracked mortar—A comparison between experimental study and finite element analysis". In: *Construction and Building Materials* 110 (2016), pp. 154–162.
- [47] Ju-Nan Kuo and Yi-Kai Lin. "Capillary kinetics of water in hydrophilic microscope coverslip nanochannels". In: *2012 7th IEEE International Conference on Nano/Micro Engineered and Molecular Systems (NEMS)*. IEEE. 2012, pp. 636–639.
- [48] Vincent Richefeu, Moulay Said El Youssoufi, Robert Peyroux, et al. "A model of capillary cohesion for numerical simulations of 3D polydisperse granular media". In: *International Journal for Numerical and Analytical Methods in Geomechanics* 32.11 (2008), pp. 1365–1383.
- [49] Jin Ho Song, Sangyul Baik, Tae-Heon Yang, et al. "Wet soft bio-adhesion of insect-inspired polymeric oil-loadable perforated microcylinders". In: *Chemical Engineering Journal* 423 (2021), p. 130194.
- [50] Liwen Zhang, Yurun Guo, Yan Wang, et al. "Multi-dimensional Self-splitting Behaviors for Improving Wet Attachment on Nonuniform Bioinspired Pillar Surface". In: *Advanced Functional Materials* 32.47 (2022), p. 2205804.
- [51] ZhenDong Dai and Stanislav Gorb. "Contact mechanics of pad of grasshopper (Insecta: ORTHOPTERA) by finite element methods". In: *Chinese Science Bulletin* 54.4 (2009), pp. 549–555.
- [52] William Alexander Osborne and W Sutherland. "The elasticity of rubber balloons and hollow viscera". In: *Proceedings of the Royal Society of London. Series B, Containing Papers of a Biological Character* 81.551 (1909), pp. 485–499.

- [53] Van Anh Ho and Shinichi Hirai. "Understanding Slip Perception of Soft Fingertips by Modeling and Simulating Stick-Slip Phenomenon." In: *Robotics: Science and System VII* (2012), pp. 129–136.
- [54] Raffaele Ardito, Alberto Corigliano, Attilio Frangi, et al. "Advanced models for the calculation of capillary attraction in axisymmetric configurations". In: *European journal of mechanics-a/solids* 47 (2014), pp. 298–308.
- [55] Nicholas J Nigro, Benjamin P Zellmer, Dongkai Shangguan, et al. "A modified finite element method for determining equilibrium capillary surfaces of liquids with specified volumes". In: *International journal for numerical methods in fluids* 33.6 (2000), pp. 833–846.
- [56] Lenar Ishbulatov, Sergey Galyshev, Pavel Solovev, et al. "Simulation of the capillary action via FlowVision software". In: *MATEC Web of Conferences*. Vol. 224. EDP Sciences. 2018, p. 02092.
- [57] James Clerk Maxwell. "Capillary action". In: *Encyclopaedia Britannica* 5 (1876), pp. 256–275.
- [58] CW Extrand. "Forces, pressures and energies associated with liquid rising in nonuniform capillary tubes". In: *Journal of colloid and interface science* 450 (2015), pp. 135–140.
- [59] Julian Szekely, AW Neumann, and YK Chuang. "The rate of capillary penetration and the applicability of the Washburn equation". In: *Journal of Colloid and Interface Science* 35.2 (1971), pp. 273–278.
- [60] Britta Buck, Johannes Lunewski, Yali Tang, et al. "Numerical investigation of collision dynamics of wet particles via force balance". In: *Chemical Engineering Research and Design* 132 (2018), pp. 1143–1159.
- [61] Evangelos Lias, Simon D Connell, Shivaprakash N Ramakrishna, et al. "Probing the frictional properties of soft materials at the nanoscale". In: *Nanoscale* 12.4 (2020), pp. 2292–2308.

- 
- [62] Yifei Mo, Kevin T Turner, and Izabela Szlufarska. "Friction laws at the nanoscale". In: *Nature* 457.7233 (2009), pp. 1116–1119.
- [63] Katerina Busuttil, Mark Geoghegan, Christopher A Hunter, et al. "Contact mechanics of nanometer-scale molecular contacts: correlation between adhesion, friction, and hydrogen bond thermodynamics". In: *Journal of the American Chemical Society* 133.22 (2011), pp. 8625–8632.
- [64] Robert W Carpick and Miquel Salmeron. "Scratching the surface: fundamental investigations of tribology with atomic force microscopy". In: *Chemical reviews* 97.4 (1997), pp. 1163–1194.
- [65] G. Bradski. "The OpenCV Library". In: *Dr. Dobb's Journal of Software Tools* (2000).